INTERNAL REPORT

HIP-2025-03

Gravitational waves from acoustic turbulence in the early universe

Jani Dahl

HELSINKI INSTITUTE OF PHYSICS

P.O.Box 64 • FIN-00014 UNIVERSITY OF HELSINKI • FINLAND

DOCTORAL DISSERTATION

To be presented for public discussion with the permission of the Faculty of Science of the University of Helsinki, in Auditorium E204, Physicum, on the 20th of August, 2025 at 12 o'clock.

Supervisors:
Prof. Kari Rummukainen
University of Helsinki

Prof. Mark Hindmarsh
University of Helsinki
University of Sussex

Prof. David Weir
University of Helsinki

Pre-examiners:
Assoc. Prof. Maarit Korpi-Lagg
Aalto University

Prof. Danièle Steer
Université Paris Cité

Opponent:
Dr. Thomas Konstandin
University of Hamburg

Custos:
Prof. Kari Rummukainen
University of Helsinki

ISSN 1455-0563 (print)
ISSN 2814-9459 (online)
ISBN 978-952-84-0006-6 (print)
ISBN 978-952-84-0007-3 (online)

Unigrafia, PunaMusta Oy
Joensuu 2025

Abstract

Gravitational waves (GWs) are an ideal probe of the early universe. Because of their nearly free propagation through cosmic history, they carry within them unfiltered information on the processes that created them and the conditions that prevailed at the time. Cosmological first-order phase transitions, predicted by many extensions to the Standard Model that aim to provide mechanisms for processes like the baryogenesis, would provide a strong source of GWs in the early universe. For a wide range of scenarios, the generation of GWs from such transitions will be dominated by sound waves that continue to propagate in the fluid long after the transition has completed. In time, these sound waves steepen into shocks, forming acoustic turbulence, that is associated with strong dissipation. The acoustic phase and its decay through acoustic turbulence are important factors in determining the overall intensity of the GW signal, and consequently, its detectability in future GW experiments, like LISA.

In this thesis we have studied acoustic turbulence by numerical simulations in two and three dimensions using the relativistic fluid equations expanded in the limit of non-relativistic bulk velocities with the ultrarelativistic equation of state. We study the shape of individual shocks, the energy spectrum, and the decay of acoustic turbulence, and compare our results against the known properties of classical acoustic turbulence. We confirm the universality of the energy spectrum after shock formation, regardless of initial conditions, and derive a universal shape function for it, associating the discovered small scale behaviour with the dissipation of shocks over time using the shape of individual shock waves. The appearance of an inertial range power law that is close and approaches the k^{-2} KP spectrum of classical acoustic turbulence with increasing Reynolds number is also confirmed. For the decay, we at late times derive analytical results for the time dependence of the kinetic energy and the integral length scale using the universality of the energy spectrum and its stationarity at large length scales.

We have improved on previous literature discussing GW generation from sound waves, namely the Sound Shell Model, by fixing an oversight that masked the true large scale behaviour of the GW power spectrum, and by studying also the expanding universe case. We confirm the model's predicted steep k^9 peak power law by numerical simulations, and find the presence of a sharp peak in the GW spectrum that is unique to the acoustic case. This acoustic peak could be an important characteristic of GWs produced by sound waves and acoustic turbulence. We have applied the shape of the energy spectrum and the properties of the decay from the simulations to estimate the GW power spectrum from decaying acoustic turbulence using the Sound Shell Model velocity field correlations. Numerical integration of the spectrum with parameter values motivated by the simulations results in a shallower peak power law that converges to k^4 in time. The convergence in the spectral amplitude induced by the decay is found to give an effective lifetime that is two times the timescale of the flow when compared to the stationary case, which is recovered in the low mean flow velocity limit. The characteristic acoustic peak is still a feature of the GW spectrum in the decaying case.

Tiivistelmä

Gravitaatioaallot tarjoavat ainutlaatuisen ikkunan varhaiseen maailmankaikkeuteen niiden lähes vuorovaikuttamattoman etenemisen seurauksena. Tänä päivänä havaittavat gravitaatioaallot pitävät sisällään tietoa niistä prosesseista ja olosuhteista, jotka vallitsivat niiden syntyhetkellä. Yksi potenttiaalinen voimakas gravitaatioaaltolähde varhaisessa maailmankaikkeudessa seuraa kosmologisista ensimmäisen kertaluvun faasimuunnoksista, joita ilmenee erilaisissa hiukkasfysiikan standardimallin laajennuksissa mekanismina selittämään ilmiöitä, kuten baryogeneesi. Laajalle kirjolle kyseisiä faasimuunnoksia hallitsevaksi gravitaatioaaltolähteeksi muodostuu muunnoksen synnyttämät ääniaallot, jotka ovat pitkäikäisiä faasimuunnoksen kestoon verrattuna. Nämä ääniaallot jyrkistyvät ajan myötä shokkiaalloiksi, johtaen akustiseksi turbulenssiksi kutsuttuun ilmiöön, joka tuo mukanaan virtauksen voimakkaan vaimenemisen. Tämän akustisen vaiheen ja sen vaimenemisen ymmärtäminen ovat tärkeitä tekijöitä niiden synnyttämän gravitaatioaaltosignaalin kokonaisintensiteetin määrittämisessä, jolla on keskeinen rooli niiden havaittavuuden kannalta, kun kyse on tulevaisuuden gravitaatioaaltoilmaisimista, kuten LISA:sta.

Tässä väitöskirjassa olemme tutkineet akustista turbulenssia numeerisilla simulaatioilla kahdessa ja kolmessa ulottuvuudessa käyttäen suhteellisuusteorian mukaisia virtausyhtälöitä ultrarelativistisella tilanyhtälöllä, jotka on kehitetty sarjaksi epärelativististen kokonaisvirtausten rajalla. Tutkimuksen kohteena ovat olleet erityisesti yksittäisten shokkiaaltojen muoto, fluidin energiaspektri, sekä akustisen turbulenssin vaimeneminen. Näistä saatuja tuloksia on verrattu klassisesta akustisesta turbulenssista tiedettyihin ominaisuuksiin. Tuloksemme vahvistavat energiaspektrin yleispätevän muodon shokkien muodostumisen jälkeen, jolle johdetun funktion käytös pienillä pituusskaaloilla määräytyy shokkiaaltojen loiventumisesta niiden vaimetessa. Simulaatioista ilmenee myös, että energiaspektrin inertia-alueen potenssilaki on lähellä, ja lähenee, klassiselle akustiselle turbulenssille ominaista k^{-2} KP-spektriä Reynoldsin luvun kasvaessa. Virtauksen vaimenemiselle johdamme myöhäisinä aikoina voimassa olevat analyyttiset tulokset kineettisen energian ja fluidin olennaispituusskaalan aikakehitykselle käyttäen energiaspektrin yleispätevyyttä ja sen muuttumattomuutta suurilla pituusskaaloilla.

Olemme parantaneet ääniaalloista syntyneiden gravitaatioaaltojen mallintamista tutkimalla niiden syntyä myös laajenevassa maailmankaikkeudessa, ja korjaamalla erään niin kutsuttuun äänikuorimalliin liittyvän laskennallisen seikan, jonka vaikutus peitti alleen gravitaatioaaltojen tehospektrin todellisen käyttäytymisen suurilla pituusskaaloilla. Vahvistamme myös kyseisen mallin ennustaman gravitaatioaaltotehospektrin huipun tuntumassa olevan jyrkän k^9 potenssilain olemassaolon numeerisilla simulaatioilla, ja näemme spektrissä terävän huipun, joka on läsnä vain akustisessa tapauksessa. Tämä niin kutsuttu akustinen huippu voi olla tärkeä piirre ääniaaltojen ja akustisen turbulenssin synnyttämien gravitaatioaaltojen tunnistamisessa. Olemme hyödyntäneet simulaatioista saatuja ominaisuuksia energiaspektrille ja virtauksen vaimenemiselle arvioidaksemme akustisesta turbulenssista seuraavaa gravitaatioaaltotehospektriä käyttämällä äänikuorimallin korrelaatioita sen nopeuskentälle. Spektrin numeerinen integrointi käyttämällä simulaatioille tyypillisiä lukuarvoja johtaa loivempaan huipun potenssilakiin, joka konvergoituu muotoon k^4 ajassa. Vaimenemisesta johtuva konvergenssi spektrin amplitudissa johtaa efektiiviseen elinikään, joka on kaksi kertaa virtauksen aikaskaala, kun verrataan vaimenemattomaan tapaukseen, johon tulokset yhtyvät alhaisen keskivirtausnopeuden rajalla. Aiemmin mainittu terävä akustinen huippu on edelleen selvästi erotettavissa myös vaimenevassa tapauksessa.

Contents

List of Publications

I. J. Dahl, M. Hindmarsh, K. Rummukainen, and D.J. Weir,
Decay of acoustic turbulence in two dimensions and implications for cosmological gravitational waves,
Phys. Rev. D **106** (Sep, 2022) 063511 [arXiv: 2112.12013]

II. R. Sharma, J. Dahl, A. Brandenburg and M. Hindmarsh,
Shallow relic gravitational wave spectrum with acoustic peak,
JCAP **12** (Dec, 2023) 042 [arXiv: 2308.12916]

III. J. Dahl, M. Hindmarsh, K. Rummukainen and D.J. Weir,
Primordial acoustic turbulence: Three-dimensional simulations and gravitational wave predictions,
Phys. Rev. D **110** (Nov, 2024) 103512 [arXiv: 2407.05826]

Author's contributions

I. The author wrote the simulation code, and did all of the simulations and data analysis. He also derived most of the analytical results, and wrote most of the paper.

II. The paper was created as a result of the author's research visit to Nordita in the autumn of 2022. The author helped in data analysis and verifying the numerical results, and in writing some parts of the paper.

III. The author wrote the simulation code, and did all of the simulations and data analysis. He also derived all of the analytical results, and wrote most of the paper.

List of abbreviations

BBO Big Bang Observer

BH Black Hole

CE Cosmic Explorer

CIT Classical Irreversible Thermodynamics

CMB Cosmic Microwave Background

CP Charge Parity

DECIGO DECi-hertz Interferometer Gravitational Wave Observatory

EM Electromagnetic

EMRI Extreme Mass Ratio Inspiral

EPTA European Pulsar Timing Array

ESA European Space Agency

ET Einstein Telescope

EW Electroweak

FLRW Friedmann-Lemaître-Robertson-Walker

FOPT First-order Phase Transition

GR General Relativity

GW Gravitational Wave

InPTA Indian Pulsar Timing Array

IPTA International Pulsar Timing Array

KAGRA Kamioka Gravitational Wave Detector

LHS Left-hand Side

(a)LIGO (advanced) Laser Interferometer Gravitational-Wave Observatory

LISA Laser Interferometer Space Antenna

MHD Magnetohydrodynamic

NANOGrav North American Nanohertz Observatory for Gravitational Waves

NMSSM Next-to-Minimal Supersymmetric Standard Model

PPTA Parkes Pulsar Timing Array

PT Phase Transition

PTA Pulsar Timing Array

QCD Quantum Chromodynamics

RD Radiation Domination

RHS Right-hand Side

rms root mean square

SGWB Stochastic Gravitational Wave Background

SKA Square Kilometer Array

SM Standard Model

SMBH Super Massive Black Hole

SSM Sound Shell Model

UETC Unequal Time Correlator

WD White Dwarf

Conventions

This thesis works in natural units so that $c = \hbar = k_B = 1$, meaning that the units of length and time, and temperature and energy coincide. We employ the metric signature convention where the sign of the time direction is negative, $(-,+,+,+)$. As for indices, Latin indices are used to refer to the spatial parts of four vectors, and thus run from 1 to 3. Greek indices run from 0 to 3 and also contain the zeroth temporal component. The Einstein summation convention is used, meaning that repeated indices are implicitly summed over.

Vectors are denoted by boldface characters $\mathbf{v}$ and their components by subscript indices v_i. Unit vectors $\mathbf{v}/v$ are denoted by hats $\hat{\mathbf{v}}$, where $v = |\mathbf{v}|$ is the vector length. Angled brackets $\langle \Pi \rangle$ are used to denote the ensemble average of the quantity Π. Depending on the context, a bar is used to denote either a background quantity in perturbation theory, or a root mean square value $\bar{v} = \sqrt{\langle \mathbf{v}^2 \rangle}$ otherwise. Time derivatives with respect to cosmic time t are denoted by overhead dots $\dot{v} = dv/dt$, and time derivatives with respect to the conformal time η by primes $v' = dv/dt$. Partial derivatives with respect to space are occasionally denoted as $\partial_i \equiv \partial/\partial x_i$, and those with respect to time as $\partial_t \equiv \partial/\partial t$. When talking about kinetic energy, we refer to the kinetic energy per unit mass.

The Fourier transform convention used here is

$$f(\mathbf{k}) = \int f(\mathbf{x}) e^{-i\mathbf{k}\cdot\mathbf{x}}\, d^3x\,, \qquad f(\mathbf{x}) = \frac{1}{(2\pi)^3} \int f(\mathbf{k}) e^{i\mathbf{k}\cdot\mathbf{x}}\, d^3k\,, \tag{1}$$

where $\mathbf{k}$ is the Fourier space wave vector, $k = |\mathbf{k}|$ is the wavenumber, and $\mathbf{x}$ is a real space vector. Other commonly used functions that appear are the Kronecker delta

$$\delta_{ij} = \begin{cases} 0 & \text{if } i \neq j \\ 1 & \text{if } i = j \end{cases}\,, \tag{2}$$

the Heaviside step function

$$\theta(x) = \begin{cases} 0 & \text{if } x < 0 \\ 1 & \text{if } x \geq 0 \end{cases}\,, \tag{3}$$

and the Dirac delta function $\delta(x)$, defined via

$$\int f(\mathbf{x})\, \delta(\mathbf{x} - \mathbf{x}')\, d^3x = f(\mathbf{x}')\,. \tag{4}$$

It can also be expressed as

$$\delta(\mathbf{x}) = \frac{1}{(2\pi)^3} \int e^{i\mathbf{k}\cdot\mathbf{x}}\, d^3k\,. \tag{5}$$

This thesis is an article-based dissertation that consists of three peer-reviewed scientific publications. We refer to the first one as Paper I: [1], the second as Paper II: [2], and the third as Paper III: [3]. The thesis is structured so that the research background, motivation, and objectives are discussed in Chapters 1–3, and the results and methods in Chapters 3–5.

In Papers I and III we have scaled all plots containing simulation data dimensionless. However, the plots in Paper II, and some quantities related to the numerical simulations, like values for initial parameters, are sometimes given without units. In such cases, the values are given in the lattice spacing units of the simulations.

1. Gravitational waves

Gravitational waves (GWs) were first predicted in 1916 on the basis of Albert Einstein's theory of general relativity. It provided a new improved description for gravity, one of the four fundamental interactions in nature, where the gravitational attraction between masses results from the geometric properties of a curved four dimensional spacetime. The curvature of spacetime is induced by objects with mass whose movement in turn alters the curvature. If the movement involves acceleration and occurs in a non-rotationally or a non-spherically symmetric way, the alterations in spacetime generate ripples in its fabric that propagate as waves outward from their source at the speed of light. These gravitational waves interact extremely weakly with matter due to the weakness of gravity compared to the other fundamental interactions. This weak coupling with matter means that they propagate through the universe effectively undisturbed, containing nearly unfiltered information on the processes and conditions that led to their formation. These properties make them an ideal probe of the early universe that is beyond the reach of detection methods of conventional astronomy due to the early universe being opaque to electromagnetic radiation until about 370 000 years after the Big Bang [4]. However, the weak coupling to matter also makes the detection of gravitational waves difficult, and extremely sensitive instruments are needed to detect the miniscule distortions in distance caused by a passing wave [5]. For this reason, it took about 100 years from their prediction to the first direct detection in 2015 by the aLIGO gravitational wave observatory that detected a signal from a binary black hole coalescence [6]. At the time of writing this thesis, the current global network of detectors have confirmed nearly 100 detections of astrophysical gravitational waves from compact binary mergers [7, 8], and many future detectors are currently being planned that have the potential to detect cosmological gravitational waves from the early universe.

This chapter provides a short introduction to GWs with the focus being on those of cosmological origin. We first cover how GWs arise from general relativity (GR), and discuss their equations of motion and its solution. We then take a look at stochastic GW backgrounds and how they are characterized using statistical methods. Finally, a short overview of GW astronomy is provided, discussing sources relevant for detection, detection methods, what can be learned by detecting GWs, and both current and future detectors.

1.1 Perturbed spacetime metric

Gravitational waves emerge from general relativity by inspecting small perturbations in some background spacetime [9, 10]. Then in first-order perturbation theory the metric tensor can be written

as

$$g_{\mu\nu} = \bar{g}_{\mu\nu} + \delta g_{\mu\nu}\,, \qquad |\delta g_{\mu\nu}| \ll |g_{\mu\nu}|\,, \tag{1.1}$$

where $\bar{g}_{\mu\nu}$ is the background metric and $\delta g_{\mu\nu}$ is the perturbation. According to the cosmological principle, the universe is highly homogeneous and isotropic at large scales [11]. The metric describing such a universe that also includes its expansion is the Friedmann-Lemaître-Robertson-Walker (FLRW) metric that written in comoving coordinates reads as [12]

$$ds^2 = \bar{g}_{\mu\nu} dx^\mu dx^\nu \tag{1.2}$$

$$= -dt^2 + a^2(t)(dx^2 + dy^2 + dz^2)\,, \tag{1.3}$$

where $a(t)$ is the scale factor that depends on the cosmic time t and accounts for the expansion of the universe through the stretching of the spatial dimensions. Observations indicate that the universe is flat to a high degree of accuracy [13], so the curvature factor has been set to zero and thus vanishes in the above equations. It is often useful to write the metric in terms of the conformal time

$$\eta = \int_0^t \frac{dt'}{a(t')}\,, \tag{1.4}$$

since this introduces the scaling by the scale factor also to the time dimension. The background metric then becomes conformal to the Minkowski metric $\eta_{\mu\nu} = \mathrm{diag}(-1, 1, 1, 1)$, and the perturbed metric tensor can be written as

$$g_{\mu\nu} = a^2(\eta_{\mu\nu} + h_{\mu\nu})\,, \tag{1.5}$$

which defines the perturbation $h_{\mu\nu}$. In first-order perturbation theory all terms of the order $O(h^2)$ are dropped in the equations. The inverse metric is then

$$g^{\mu\nu} = a^{-2}(\eta^{\mu\nu} - h^{\mu\nu})\,, \tag{1.6}$$

and indices are raised and lowered using the background metric

$$h^\mu_\nu = \eta^{\mu\rho} h_{\rho\nu}\,, \qquad h^{\mu\nu} = \eta^{\mu\rho}\eta^{\nu\sigma} h_{\rho\sigma}\,. \tag{1.7}$$

One of the key postulates of general relativity is that the laws of physics must have the same form in all reference frames. In other words, they need to remain invariant under coordinate transformations. This is referred to as the principle of relativity, or the gauge symmetry of general relativity, and in a perturbed spacetime these coordinate transformations are called gauge transformations [14]. It follows from this property that it does not matter which coordinate system is used in the case of physical quantities and observables, as the same results should be recovered in all of them. However, the equations and expressions resulting from GR can be greatly simplified by a certain choice of gauge. This is also useful for determining physical degrees of freedom because only non-physical degrees of freedom can vanish, i.e. be gauged away by gauge transformations. The perturbation $h_{\mu\nu}$ can be separated into scalar, vector, and tensor parts, depending on its transformation properties under rotations in the background space: h_{00} transforms as a scalar, h_{0i} as a vector, and the spatial part can be written as

$$h_{ij} = 2\phi\delta_{ij} + h^T_{ij}\,, \tag{1.8}$$

where $\phi(x)$ is a scalar field, and h^T_{ij} is traceless under the background metric ($\bar{g}^{ij}h^T_{ij} = \delta^{ij}h^T_{ij} = 0$). Much like a Euclidean vector field can be separated into longitudinal (curl free) and transverse (divergence free) parts according to the Helmholtz decomposition, the symmetric and traceless tensor h^T_{ij} can further be decomposed as [15, 16]

$$h^T_{ij} = h^S_{ij} + h^V_{ij} + h^{TT}_{ij}\,, \tag{1.9}$$

where the scalar part is

$$h^S_{ij} = (\partial_i\partial_j - \frac{1}{3}\delta_{ij}\nabla^2)h\,, \tag{1.10}$$

the vector part is

$$h^V_{ij} = -\frac{1}{2}(h_{i,j} + h_{j,i}), \qquad \delta^{ij}h_{i,j} = 0\,, \tag{1.11}$$

and the tensor part is transverse and traceless so that

$$\delta^{ik}h^{TT}_{ij,k} = 0\,, \qquad \delta^{ij}h^{TT}_{ij} = 0\,. \tag{1.12}$$

Here h is a scalar field, h_i is a vector field, and we have introduced the shorthand notation $h_{i,j} \equiv \partial_j h_i \equiv \partial h_i/\partial x_j$. Hence, the metric perturbation $h_{\mu\nu}$ of equation (1.5) has been decomposed into: a scalar part consisting of h_{00}, the first term on the LHS of equation (1.8), and h^S_{ij}; a vector part consisting of h_{0i} and h^V_{ij}; and a tensor part h^{TT}_{ij}. The vector h_{0i} can then be decomposed into curl free (which can be written as a gradient of a scalar) and divergence free parts as $h_{0i} = -B_{,i} + B^V_i$ where $\delta^{ij}B^V_{i,j} = 0$. The metric perturbation $h_{\mu\nu}$ is a symmetric 4×4 tensor, so it has 10 degrees of freedom. By counting the degrees of freedom resulting from the decomposition, we have 4 scalar degrees of freedom (h_{00}, ϕ, h, B), 6 vector degrees of freedom (h_i, B^V_i), and 6 tensor degrees of freedom that follow from the symmetric 3×3 tensor h^{TT}_{ij}, totalling 16. We also have 1 constraint for both B^V_i and h_i, 3 constraints for h^{TT}_{ij} following from the transverse condition, and 1 more from the condition of tracelessness, totalling 6. All in all, this leads to 4 scalar degrees of freedom, $6-2=4$ vector degrees of freedom, and $6-4=2$ tensor degrees of freedom, meaning that all 10 degrees of freedom of the metric perturbation are accounted for by the decomposition. By inspecting how they behave under gauge transformations, it can be shown that two of the scalar and two of the vector degrees of freedom can be gauged away, while h^{TT}_{ij} is gauge-invariant [17]. Therefore, only 6 degrees of freedom (2 scalar, 2 vector, 2 tensor) in $h_{\mu\nu}$ are physical.

In first-order perturbation theory the perturbations of different type are decoupled from each other; they evolve independently and can be treated separately in the equations. The scalar perturbations are important for structure formation, the formation and clustering of galaxies, since they couple to density and pressure perturbations, and display gravitational instability [18]. In the study of scalar perturbations, the two physical degrees of freedom are written in terms of the gauge-invariant Bardeen potentials [19]. Vector perturbations are not interesting from a cosmological point of view, since they contain only decaying modes, so the perturbations disappear quickly after their creation. Finally, the tensor perturbations correspond to gravitational waves that propagate in a FLRW background for modes inside the Hubble horizon. As a result of the decomposition, they are automatically in the so-called transverse-traceless gauge. The two physical degrees of freedom for metric tensor perturbations are the two polarization modes of GWs, the linearly polarized mode

h_+, and the cross polarized mode $h_\times$. In this thesis we consider only GWs, so we are free to drop the scalar and vector perturbations from the equations as a result of the decoupling in first-order perturbation theory. In the next section we will see how to machinery of general relativity can be used to obtain the equations of motion for GWs.

1.2 Metric tensor perturbations

Considering only metric tensor perturbations, the metric in Eq. (1.5) can be written as

$$ds^2 = a^2[-d\eta^2 + (\delta_{ij} + h_{ij}^{TT})dx^i dx^j]\,. \tag{1.13}$$

The equations of motion for gravitational waves follow from the Einstein field equations [20]

$$G_{\mu\nu} = 8\pi G T_{\mu\nu}\,, \tag{1.14}$$

where $G_{\mu\nu}$ is the Einstein tensor, and $T_{\mu\nu}$ is the energy-momentum tensor, also known as the stress-energy tensor. The equation relates the geometry of spacetime (left-hand side) to its matter and energy content (right-hand side). Therefore, the Einstein tensor depends on the metric, through

$$G_{\mu\nu} = R_{\mu\nu} - \frac{1}{2}g_{\mu\nu}R, \qquad R = g^{\mu\nu}R_{\mu\nu} = R^{\mu}_{\mu}\,, \tag{1.15}$$

where $R_{\mu\nu}$ is the Ricci curvature tensor, and R the scalar curvature. The former can be written as a contraction of the Riemann tensor $R_{\mu\nu} \equiv R^{\rho}_{\mu\rho\nu}$ where

$$R^{\rho}_{\sigma\mu\nu} = \partial_\mu\Gamma^{\rho}_{\nu\sigma} - \partial_\nu\Gamma^{\rho}_{\mu\sigma} + \Gamma^{\rho}_{\mu\lambda}\Gamma^{\lambda}_{\nu\sigma} - \Gamma^{\rho}_{\nu\lambda}\Gamma^{\lambda}_{\mu\sigma}\,, \tag{1.16}$$

and $\Gamma^{\rho}_{\nu\sigma}$ are the Christoffel symbols that are functions of the metric tensor

$$\Gamma^{\sigma}_{\mu\nu} = \frac{1}{2}g^{\sigma\rho}(\partial_\mu g_{\nu\rho} + \partial_\nu g_{\rho\mu} - \partial_\rho g_{\mu\nu})\,. \tag{1.17}$$

Substituting the metric of Eq. (1.13) into the above and keeping only terms that are of first order in the perturbation gives the Christoffel symbols as

$$\Gamma^0_{00} = \mathcal{H}\,, \qquad \Gamma^0_{0i} = 0\,, \qquad \Gamma^i_{00} = 0 \tag{1.18}$$

$$\Gamma^0_{ij} = \mathcal{H}(\delta_{ij} + h^{TT}_{ij}) + \frac{1}{2}h^{TT\prime}_{ij} \tag{1.19}$$

$$\Gamma^i_{0j} = \mathcal{H}\delta_{ij} + \frac{1}{2}h^{TT\prime}_{ij} \tag{1.20}$$

$$\Gamma^i_{jk} = \frac{1}{2}\left(h^{TT}_{ij,k} + h^{TT}_{ik,j} - h^{TT}_{jk,i}\right)\,, \tag{1.21}$$

where we have introduced the shorthand notation of marking derivatives with respect to conformal time with primes, i.e. $' \equiv \partial/\partial\eta$, and denoted by $\mathcal{H}$ the conformal, or comoving, Hubble parameter

$$\mathcal{H} \equiv \frac{a'}{a} = aH = \dot{a}\,, \tag{1.22}$$

where H is the Hubble parameter and $\dot{} \equiv d/dt$. The inverse metric can be used to raise one of the indices, giving the Ricci tensor as

$$R^0_0 = 3a^{-2}\mathcal{H}'\,, \qquad R^i_0 = 0 \tag{1.23}$$

$$R^i_j = a^{-2}(\mathcal{H}' + 2\mathcal{H}^2)\delta_{ij} + \frac{1}{2}a^{-2}\left(h^{TT\prime\prime}_{ij} - \nabla^2 h^{TT}_{ij} + 2\mathcal{H}h^{TT\prime}_{ij}\right) \tag{1.24}$$

and the scalar curvature then becomes

$$R = 6a^{-2}(\mathcal{H}' + \mathcal{H}^2)\,. \tag{1.25}$$

Using these, it follows from equation (1.15) that

$$G_0^0 = -3a^{-2}\mathcal{H}^2\,, \qquad G_0^i = G_i^0 = 0 \tag{1.26}$$

$$G_j^i = -a^{-2}(2\mathcal{H}' + \mathcal{H}^2)\delta_{ij} + \frac{1}{2}a^{-2}\left(h_{ij}^{TT\prime\prime} - \nabla^2 h_{ij}^{TT} + 2\mathcal{H}h_{ij}^{TT\prime}\right)\,, \tag{1.27}$$

so only the spatial part of the Einstein tensor ends up being dependent on the perturbations. We can decouple the equations for the background and the perturbations, as the background equations end up giving just the Friedmann equations. Because the tensor perturbations lie in the transverse-traceless gauge, we need the transverse and traceless part of the perturbed energy-momentum tensor in the RHS of (1.14). To this end, we separate the energy-momentum tensor into a background and a perturbation as

$$T_\nu^\mu = \overline{T}_\nu^\mu + \delta T_\nu^\mu\,. \tag{1.28}$$

In FLRW cosmology, it follows from the assumption of the statistical homogeneity and isotropy of the universe that the energy-momentum tensor has a perfect fluid form. Hence, perturbations in $T_{\mu\nu}$ manifest as inhomogeneities or anisotropies over the perfect fluid background*. Due to the isotropy, we can take the fluid to be at rest in the background universe. Then, the most general form for the energy momentum tensor in first-order perturbation theory becomes [17]

$$T_0^0 = -(\bar{\rho} + \delta\rho) \tag{1.29}$$

$$T_0^i = T^i + T_{,i} \tag{1.30}$$

$$T_j^i = (\bar{p} + \delta p)\delta_j^i + \Pi_j^i\,, \tag{1.31}$$

where $\delta\rho, \delta p, T, T^i, \Pi_j^i$ are first-order small perturbations. Here ρ is the energy density, p is the pressure, and Π_j^i is the anisotropic stress tensor. A similar decomposition has been used here as in the previous section for $h_{\mu\nu}$. Likewise, we can also decompose the anisotropic stress tensor into scalar, vector, and tensor parts, where the tensor part Π_{ij}^{TT} is again automatically transverse and traceless as a result of the decomposition. This is the part we are interested in, as it couples to metric tensor perturbations. It can be extracted from the anisotropic stress by moving to Fourier space

$$\Pi_{ij}(\mathbf{x}, t) = \int \frac{d^3k}{(2\pi)^3}\Pi_{ij}(\mathbf{k}, t)e^{-i\mathbf{k}\cdot\mathbf{x}}\,, \tag{1.32}$$

and applying a projector operator [21] in the following way

$$\Pi_{ij}^{TT}(\mathbf{k}) = \Lambda_{ij,lm}(\hat{\mathbf{k}})\Pi_{lm}(\mathbf{k})\,, \tag{1.33}$$

where one can write the projector explicitly as

$$\Lambda_{ij,lm}(\hat{\mathbf{k}}) = P_{il}(\hat{\mathbf{k}})P_{jm}(\hat{\mathbf{k}}) - \frac{1}{2}P_{ij}(\hat{\mathbf{k}})P_{lm}(\hat{\mathbf{k}})\,. \tag{1.34}$$

*For more information about the energy-momentum tensor and its general perfect fluid form, see Eq. (3.16) in section 3.1. Note that in that section the total energy density is denoted by e instead of the ρ used here.

The operators P_{ij} have the form

$$P_{ij}(\hat{\mathbf{k}}) = \delta_{ij} - \hat{k}_i \hat{k}_j \,, \tag{1.35}$$

so they are symmetric and transverse ($k_i P_{ij} = 0$) and are projectors because they fulfil $P_{il}P_{lj} = P_{ij}$. From this it follows that $\Lambda_{ij,lm}$ is also a projector

$$\Lambda_{ij,kl}(\hat{\mathbf{k}})\Lambda_{kl,mn}(\hat{\mathbf{k}}) = \Lambda_{ij,mn}(\hat{\mathbf{k}}) \,, \tag{1.36}$$

and that it is transverse on all indices $k_i \Lambda_{ij,lm} = 0$, $k_j \Lambda_{ij,lm} = 0$, and traceless with respect to the indices (i, j) and (l, m), i.e. $\Lambda_{ii,lm} = \Lambda_{ij,mm} = 0$, and is symmetric under the simultaneous exchange of these indices. Hence, applying the operator (1.34) to any symmetric tensor S_{ij} gives its transverse-traceless part. We can now write the perturbed Einstein field equations

$$\delta G^{\mu}_{\nu} = 8\pi G \delta T^{\mu}_{\nu} \tag{1.37}$$

using the perturbation dependent part of Eq. (1.27), and the transverse and traceless part of the anisotropic stress, yielding

$$h_{ij}^{TT\prime\prime} + 2\mathcal{H} h_{ij}^{TT\prime} - \nabla^2 h_{ij}^{TT} = 16\pi G a^2 \Pi_{ij}^{TT} \,, \tag{1.38}$$

which is the equation of motion for gravitational waves. The left-hand side has the form of a wave equation with a $\mathcal{H}$-dependent damping term that results from the expansion of the universe. The right-hand side can be interpreted as a source term, meaning that GWs are generated by the transverse and traceless part of the anisotropic stress, that is, the shear stresses, with solutions depending on the nature of the source. Inspecting the equation further is convenient in Fourier space. Defining a comoving tensor perturbation $\tilde{h}_{ij} = a h_{ij}^{TT}$ and moving to Fourier space gives

$$\tilde{h}_{ij}''(\mathbf{k}) + \left(k^2 - \frac{a''}{a}\right) \tilde{h}_{ij}(\mathbf{k}) = 16\pi G a^3 \Pi_{ij}^{TT}(\mathbf{k}) \,. \tag{1.39}$$

To inspect GWs that propagate freely in the FLRW background after the source has switched off, we take $\Pi_{ij}^{TT} = 0$. For modes that are well inside the Hubble horizon, $k \gg \mathcal{H}$, resulting in $k^2 \gg a''/a \sim 1/\eta^2$, meaning that we can neglect the a''/a term*. The equation then becomes that of a simple harmonic oscillator, giving the solution

$$\tilde{h}_{ij} \propto \sin(k\eta + \alpha) \qquad (k\eta \gg 1) \,, \tag{1.40}$$

which then in terms of the metric tensor perturbations becomes

$$h_{ij}^{TT} \propto \frac{1}{a} \sin(k\eta + \alpha) \qquad (k\eta \gg 1) \,, \tag{1.41}$$

showing that in the freely propagating regime the metric tensor perturbations are oscillating waves that travel at the speed of light ($c = 1$) and whose amplitude is suppressed by the expansion of the universe. GWs are also insensitive to absorption and scattering by matter during their propagation because the gravitational cross-section is extremely small at energies below the Planck scale [22].

*The scale factor a has a general power law form $a(\eta) \propto a^n$, where $n = 1$ during radiation, $n = 2$ during matter, and $n = -1$ during dark energy dominated eras. Then $a''/a \propto \mathcal{H}^2$. In fact, during RD the a''/a term in the GW equation vanishes altogether.

During the period when the source is still active, the equation for sub-horizon modes becomes

$$\tilde{h}''_{ij}(\mathbf{k}) + k^2 \tilde{h}_{ij}(\mathbf{k}) = 16\pi G a^3 \Pi^{TT}_{ij}(\mathbf{k}) \,, \tag{1.42}$$

which is analogous to that of a driven harmonic oscillator. It can be solved using the Green's function method. For the operator $\partial^2_\eta + k^2$ the Green's function is

$$G(\eta - \eta') = \frac{1}{k} \sin\left[k(\eta - \eta')\right] \theta(\eta - \eta') \,, \tag{1.43}$$

where $\theta(x)$ is the Heaviside step function, which is zero for negative and one for positive arguments. Assuming that the source activates at some initial time η_i with the initial conditions $\tilde{h}_{ij}(\eta_i, \mathbf{k}) = 0$, $\tilde{h}'_{ij}(\eta_i, \mathbf{k}) = 0$, the solution becomes

$$\tilde{h}_{ij}(\eta, \mathbf{k}) = 16\pi G \int_{-\infty}^{\infty} d\eta' \, G(\eta - \eta') a^3(\eta') \Pi^{TT}_{ij}(\eta', \mathbf{k}) \tag{1.44}$$

$$= \frac{16\pi G}{k} \int_{\eta_i}^{\eta} d\eta' \, \sin\left[k(\eta - \eta')\right] a^3(\eta') \Pi^{TT}_{ij}(\eta', \mathbf{k}) \,. \tag{1.45}$$

Gravitational wave sources are active only for a limited amount of time. Assuming that the source switches off at η_f, Eq. (1.45) is valid for times $\eta_i < \eta < \eta_f$. For times $\eta \geq \eta_f$ the source term on the RHS of the GW equation vanishes, and we get the free wave solution in equation (1.40) that more explicitly can also be written as

$$\tilde{h}_{ij}(\eta, \mathbf{k}) = A_{ij}(\mathbf{k}) \sin\left[k(\eta - \eta_f)\right] + B_{ij}(\mathbf{k}) \cos\left[k(\eta - \eta_f)\right] \,. \tag{1.46}$$

At time $\eta = \eta_f$ the solutions in equations (1.45) and (1.46) must match, which fixes the amplitude coefficients A_{ij} and B_{ij} as

$$A_{ij} = \frac{16\pi G}{k} \int_{\eta_i}^{\eta_f} d\eta' \, \cos\left[k(\eta_f - \eta')\right] a^3(\eta') \Pi^{TT}_{ij}(\eta', \mathbf{k}) \tag{1.47}$$

$$B_{ij} = \frac{16\pi G}{k} \int_{\eta_i}^{\eta_f} d\eta' \, \sin\left[k(\eta_f - \eta')\right] a^3(\eta') \Pi^{TT}_{ij}(\eta', \mathbf{k}) \,, \tag{1.48}$$

where the upper equation for A_{ij} is obtained by matching the equations for the derivative $\tilde{h}'_{ij}$. Substituting these into Eq. (1.46) and using the product to sum formula for the sines and cosines leads to some cancellation, and we get that at times after the source has stopped operating, the solution for sub-horizon modes can be written as

$$\tilde{h}_{ij}(\eta \geq \eta_f, \mathbf{k}) = \frac{16\pi G}{k} \int_{\eta_i}^{\eta_f} d\eta' \, \sin\left[k(\eta - \eta')\right] a^3(\eta') \Pi^{TT}_{ij}(\eta', \mathbf{k}) \,. \tag{1.49}$$

A common approximation in studying primordial gravitational wave generation is to assume the duration of the source to be much less than the Hubble time $H_\star^{-1}$ at time η_i. In this case the

expansion of the universe can be neglected, and in Eq. (1.38) we replace $a \to a_\star$, where $a_\star$ is a constant. We can normalize it so that $a_\star = 1$, which means that $\tilde{h}_{ij} \to h_{ij}^{TT}$, $\eta \to t$, and $\mathcal{H} \to H_\star$, where $H_\star$ is a constant in time. The solution then becomes Eq. (1.46) with the same replacements, and the matching of the coefficients proceeds in a similar manner. The equations can also be written for the two polarization states h_+^{TT} and $h_\times^{TT}$ by decomposing h_{ij}^{TT} like in Refs. [22–24]. However, in this thesis we choose to work in the basis of h_{ij}^{TT} instead, as both bases lead to the same results in the statistical treatment introduced in the next section.

1.3 Stochastic gravitational wave background

Much like with the cosmic microwave background (CMB), which consists of the relic radiation from the Big Bang, there is good reason to expect that the universe is also permeated by a stochastic background of gravitational waves (SGWB) generated in the early universe. Such a background would be an incoherent sum of GWs from a large number of various independent unresolved early universe GW sources [25]. As a result, the background is of random nature and its study requires statistical treatment, the Fourier amplitudes* $h_{ij}(k,\eta)$ assumed as random variables characterized by two-point functions that are ensemble averages of the form $\left\langle h_{ij}(\eta,k)h_{ij}^\star(\eta,k')\right\rangle$. Such an average means an average over multiple copies of the system, which is not feasible in the case of the universe. Therefore, to deal with the averages, the following assumptions are made about stochastic GW backgrounds:

- The background is assumed to be stationary so that the two-point correlators depend on time only through time differences $\eta - \eta'$, and not separately on η and η'. This is justified because the timescale for a change in a background created during cosmological epochs is large (of the order of the age of the universe) compared to observation times.

- The background is taken to be Gaussian so that N-point correlator functions can be reduced to a sum of products between two-point correlators using Wick's theorem. The Gaussianity follows from the fact that the GW background is formed from many individual contributions coming from different uncorrelated regions. If the amount of contributions is sufficiently large, then by the central limit theorem such a superposition of signals can then be taken to have a Gaussian distribution [26].

- The early universe was highly isotropic, so like with the CMB, the GW background can be assumed to be isotropic to first approximation. In principle, this along with the homogeneity follows from the same properties of the FLRW background. Intuitively this is also easy to understand, as the physical processes that generate the GWs take place in uncorrelated regions simultaneously and in the same way, so the superposition of these signals ends up being statistically homogeneous and isotropic. As a result, waves coming from different directions

*In order to make the notation more concise, we denote from now on $h_{ij}^{TT} \equiv h_{ij}$ since the danger of confusing this with the spatial part of the cosmological perturbation $h_{\mu\nu}$ is no more. We also drop the bars from background quantities, like $\bar{\rho}$, since we now only consider tensor perturbations.

are uncorrelated, which for the two-point correlators results in

$$\left\langle h_{ij}(\eta,k)h^{\star}_{ij}(\eta,k')\right\rangle \propto \delta(\mathbf{k}-\mathbf{k}')F(k)\,, \tag{1.50}$$

where F is a function of the modulus $k = |\mathbf{k}|$ only, resulting from isotropy, and the delta function results from homogeneity.

- The background is considered unpolarized since the universe is not expected to contain GW sources that are based on parity violating interactions. As a result, in the GW background the two polarizations + and × are uncorrelated

$$\left\langle h_{+}(\eta,k)h^{\star}_{\times}(\eta,k')\right\rangle = 0\,. \tag{1.51}$$

For GW sources that fulfil causality, and assuming a statistically homogeneous and isotropic universe, we can invoke the ergodic hypothesis, which states that observing large enough regions of the universe, or any region for long enough, corresponds to having many realizations of the universe. Then the ensemble averages in the correlators can be replaced by either spatial or temporal averages.

SGWBs are typically characterized by the GW energy density per logarithmic frequency interval. The GW energy density can be extracted from the energy-momentum tensor of gravitational waves that can be calculated by averaging the Ricci tensor in second order perturbation theory over several gravitational wave lengths under a short wavelength approximation that assumes the length scale of the background to be much larger than the GW wavelength. The result is known as the Isaacson tensor as a consequence of the original derivation by Isaacson in Refs. [27, 28]. For other more recent works that discuss the derivation, see Refs. [5, 21, 29]. In the transverse and traceless gauge the Isaacson tensor can be written as

$$T^{\mathrm{GW}}_{\mu\nu} = \frac{\left\langle \nabla_{\mu}h_{ij}\nabla_{\nu}h_{ij}\right\rangle}{32\pi G}\,, \tag{1.52}$$

where ∇_{μ} denotes the covariant derivative with respect to the background metric. The energy density is given by the 00-component, and in first-order perturbation theory with the FLRW metric, $\nabla_0 h_{ij} = \dot{h}_{ij}$, so that

$$\rho_{\mathrm{GW}} = T^{\mathrm{GW}}_{00} = \frac{\left\langle \dot{h}_{ij}(\mathbf{x},t)\dot{h}_{ij}(\mathbf{x},t)\right\rangle}{32\pi G} = \frac{\left\langle h'_{ij}(\mathbf{x},\eta)h'_{ij}(\mathbf{x},\eta)\right\rangle}{32\pi G a^2(\eta)}\,, \tag{1.53}$$

where in the last step Eq. (1.4) was used to convert from cosmic to conformal time. Differentiating the relation $\tilde{h}_{ij} = a h_{ij}$ with respect to the conformal time allows us to write this in terms of the comoving perturbation as

$$\rho_{\mathrm{GW}} = \frac{\left\langle \left(\tilde{h}'_{ij}(\mathbf{x},\eta) - \mathcal{H}\tilde{h}_{ij}(\mathbf{x},\eta)\right)^2\right\rangle}{32\pi G a^4(\eta)} \tag{1.54}$$

$$\approx \frac{1}{32\pi G a^4(\eta)}\left\langle \tilde{h}'_{ij}(\mathbf{x},\eta)\tilde{h}'_{ij}(\mathbf{x},\eta)\right\rangle\,, \tag{1.55}$$

where we have neglected the second term in the parentheses because for sub-horizon modes $\tilde{h}'_{ij} \sim k\tilde{h}_{ij} \gg \mathcal{H}\tilde{h}_{ij}$. The GW energy density now displays the a^{-4} scaling of radiation, which is expected for massless degrees of freedom. To tap into the frequency domain, we Fourier transform the two-point function in the previous equation using the inverse transform. This yields

$$\left\langle \tilde{h}'_{ij}(\mathbf{x},\eta)\tilde{h}'_{ij}(\mathbf{x},\eta)\right\rangle = \int \frac{d^3k}{(2\pi)^3}\int \frac{d^3k'}{(2\pi)^3}\left\langle \tilde{h}'_{ij}(\mathbf{k},\eta)\tilde{h}'_{ij}(\mathbf{k}',\eta)\right\rangle e^{i\mathbf{x}\cdot(\mathbf{k}+\mathbf{k}')} \tag{1.56}$$

$$= \int \frac{d^3k}{(2\pi)^3}\int \frac{d^3k'}{(2\pi)^3}\left\langle \tilde{h}'_{ij}(\mathbf{k},\eta)\tilde{h}^{\star\prime}_{ij}(\mathbf{k}',\eta)\right\rangle e^{i\mathbf{x}\cdot(\mathbf{k}-\mathbf{k}')}\,, \tag{1.57}$$

where we have performed a change of variables $\mathbf{k}' \to -\mathbf{k}'$, and used the property of Fourier transforms of real functions that states $\tilde{h}'_{ij}(-\mathbf{k}',\eta) = \tilde{h}^{\star\prime}_{ij}(\mathbf{k}',\eta)$. Now we postulate that the assumptions listed at the start of this section for h_{ij} also hold for the time derivatives $\tilde{h}'_{ij}$. Then we can define the spectral density of the time derivative of the metric tensor perturbations $P_{h'}(k)$ as

$$\left\langle \tilde{h}'_{ij}(\mathbf{k},\eta)\tilde{h}^{\star\prime}_{ij}(\mathbf{k}',\eta)\right\rangle = (2\pi)^3\delta(\mathbf{k}-\mathbf{k}')P_{h'}(k,\eta)\,. \tag{1.58}$$

Substituting this into the equation above, we can integrate over the delta function and equation (1.55) becomes

$$\rho_{\rm GW} = \frac{1}{32\pi G a^4(\eta)}\int \frac{d^3k}{(2\pi)^3}P_{h'}(k) \tag{1.59}$$

$$= \frac{1}{32\pi G a^4(\eta)}\int_0^\infty \frac{dk}{2\pi^2}k^2 P_{h'}(k)\,. \tag{1.60}$$

The energy density is normalized in a natural way by the critical density of the universe

$$\rho_c = \frac{3H^2}{8\pi G} = \frac{3\mathcal{H}^2}{8\pi G a^2}\,, \tag{1.61}$$

which is the energy density required for a spatially flat universe, that is, one of the Friedmann equations with zero curvature factor. Then the intensity of SGWBs is characterized by the dimensionless fraction

$$\Omega_{\rm GW} \equiv \frac{\rho_{\rm GW}}{\rho_c}\,. \tag{1.62}$$

The GW energy density can also be written as an integral over a logarithmic wavenumber interval $d\ln k$ as

$$\rho_{\rm GW} = \int_{k=0}^{k=\infty} d(\ln k)\,\frac{d\rho_{\rm GW}}{d\ln k}\,, \tag{1.63}$$

which from Eq. (1.62) allows us to define the gravitational wave power spectrum*

$$\mathcal{P}_{\rm GW}(k) \equiv \frac{1}{\rho_c}\frac{d\rho_{\rm GW}}{d\ln k} \tag{1.64}$$

so that

$$\Omega_{\rm GW} = \int_{k=0}^{k=\infty} d(\ln k)\,\mathcal{P}_{\rm GW}(k)\,. \tag{1.65}$$

*In literature, this quantity is also often denoted by $\Omega_{\rm GW}(k)$.

The reason why the spectrum is defined with respect to the logarithmic interval instead of just dk, is that this way the spectrum in Eq. (1.64) is dimensionless. It characterizes the distribution of GW energy to different wavenumbers (or frequencies when written in terms of $f = k/2\pi$), that are related to length scales by their inverse values. Substituting the result for $\rho_{\rm GW}$ in Eq. (1.60) and the critical density of Eq. (1.61) into the definition of the spectrum in Eq. (1.64) allows us to write it as

$$\mathcal{P}_{\rm GW}(k) = \frac{1}{12\mathcal{H}^2 a^2}\frac{k^3}{2\pi^2}P_{h'}(k)\,. \tag{1.66}$$

The above quantities are evaluated at the time of the GW production. Using the fact that the GW energy density dilutes like radiation $\rho_{\rm GW} \propto a^{-4}$, and that the waves propagate freely after production, we find that the GW power spectrum today is given by

$$\mathcal{P}_{\rm GW}(k,t_0) = \left(\frac{a_\star}{a_0}\right)^4 \frac{1}{\rho_0}\rho_\star \left(\frac{1}{\rho}\frac{d\rho_{\rm GW}}{d\ln k}\right)_\star \tag{1.67}$$

$$= \left(\frac{a_\star^2 H_\star}{a_0^2 H_0}\right)^2 \mathcal{P}_{\rm GW}(k,t_\star)\,, \tag{1.68}$$

where the subscript 0 refers to the present day values, and the subscript $\star$ to values during the GW production.

Next, we use the solution of the GW equation in (1.49) to write the GW power spectrum in terms of the GW generating source, the shear stresses Π_{ij}^{TT}. By using the inverse metric to lower the index in Eq. (1.31), the transverse and traceless part of the energy-momentum tensor is

$$T_{ij}^{TT} = a^2\Pi_{ij}^{TT} \equiv a^2(\rho+p)\tilde{\Pi}_{ij}^{TT}\,, \tag{1.69}$$

where we have defined the dimensionless scaled shear stress tensor $\tilde{\Pi}_{ij}^{TT}$ by extracting the enthalpy density $\rho+p$ from the full tensor. In the case of a perfect fluid, like in the FLRW universe, the energy density ρ and the pressure p are related by a barotropic equation of state

$$\rho = wp\,, \tag{1.70}$$

where for radiation, matter, and dark energy one has $w = 1/3$, $w = 0$, and $w = -1$ respectively. For a generic fluid, the pressure is a function of the energy density and the entropy density s, so that

$$\frac{dp}{d\rho} = c_s^2 = \left(\frac{\partial p}{\partial\rho}\right)_s + \left(\frac{\partial p}{\partial s}\right)_\rho \frac{\partial s}{\partial\rho}\,, \tag{1.71}$$

where the first term on the RHS is the adiabatic speed of sound, and the second term is the non-adiabatic speed of sound. Hence, for a barotropic fluid with $p = p(\rho)$, the non-adiabatic term vanishes, and using Eq. (1.70) one finds

$$c_s^2 = \frac{dp}{d\rho} = \frac{\dot{p}}{\dot{\rho}} = w + \frac{\dot{w}}{\dot{p}}\,, \tag{1.72}$$

so that for a constant w, we have simply the relation

$$w = c_s^2\,. \tag{1.73}$$

This result with Eq. (1.70) is known as the ultrarelativistic equation of state. We can now write Eq. (1.69) in terms of the fluid sound speed as

$$\Pi_{ij}^{TT} = (1 + c_s^2)\rho\tilde{\Pi}_{ij}^{TT}\,, \tag{1.74}$$

where we can replace the energy density ρ using the background Friedmann equation (1.61) since we work in first-order perturbation theory. This gives

$$\Pi_{ij}^{TT} = \frac{3(1 + c_s^2)}{8\pi G a^2}\mathcal{H}^2\tilde{\Pi}_{ij}^{TT}\,. \tag{1.75}$$

Substituting this into the GW solution in Eq. (1.49) gives

$$\tilde{h}_{ij}(\mathbf{k}, \eta) = \frac{6(1 + c_s^2)}{k}\int_{\eta_i}^{\eta_f} d\eta'\ \sin\left[k(\eta - \eta')\right] a(\eta')\mathcal{H}^2(\eta')\tilde{\Pi}_{ij}^{TT}(\mathbf{k}, \eta')\,, \tag{1.76}$$

where the dependence on the scale factor has been scaled out of the shear stress. This can now be used in the two-point function on the LHS of equation (1.58) to relate the shear stresses to the spectral density $P_{h'}$. After taking the derivative with respect to the conformal time η and substituting, the averages now hit the random variables of the stochastic GW generating process, that is, the Fourier modes of the shear stress, and one obtains

$$\begin{aligned}\left\langle \tilde{h}'_{ij}(\mathbf{k}, \eta)\tilde{h}^{\star\prime}_{ij}(\mathbf{k}', \eta)\right\rangle = 36(1 + c_s^2)^2 \int_{\eta_i}^{\eta_f} d\eta_1 \int_{\eta_i}^{\eta_f} d\eta_2\ \cos\left[k(\eta - \eta_1)\right]\cos\left[k'(\eta - \eta_2)\right] \\ \times a(\eta_1)a(\eta_2)\mathcal{H}^2(\eta_1)\mathcal{H}^2(\eta_2)\left\langle \tilde{\Pi}_{ij}^{TT}(\mathbf{k}, \eta_1)\tilde{\Pi}_{ij}^{\star TT}(\mathbf{k}', \eta_2)\right\rangle\,.\end{aligned} \tag{1.77}$$

Assuming a statistically homogeneous, isotropic, and stationary source, we can define

$$\left\langle \tilde{\Pi}_{ij}^{TT}(\mathbf{k}, \eta_1)\tilde{\Pi}_{ij}^{\star TT}(\mathbf{k}', \eta_2)\right\rangle = (2\pi)^3\delta(\mathbf{k} - \mathbf{k}')U_\Pi(k, \eta_1, \eta_2)\,, \tag{1.78}$$

where U_Π is the fluid shear stress unequal time correlator (UETC). Using this in Eq. (1.77) and comparing with Eq. (1.58), we can identify

$$\begin{aligned}P_{h'}(k, \eta) = 36(1 + c_s^2)^2 \int_{\eta_i}^{\eta_f} d\eta_1\, a(\eta_1)\mathcal{H}^2(\eta_1) \int_{\eta_i}^{\eta_f} d\eta_2\, a(\eta_2)\mathcal{H}^2(\eta_2) \\ \times \cos\left[k(\eta - \eta_1)\right]\cos\left[k(\eta - \eta_2)\right] U_\Pi(k, \eta_1, \eta_2)\,.\end{aligned} \tag{1.79}$$

This result for the spectrum holds for times after the source has stopped operating, i.e. for $\eta \geq \eta_f$. However, the spectrum still seems to be time-dependent even tough the energy of the GWs should no longer be affected by the source. In order to have a better understanding of this, we can decompose the two cosines as

$$\begin{aligned}\cos\left[k(\eta - \eta_1)\right]\cos\left[k(\eta - \eta_2)\right] = \frac{1}{2}\Big\{\cos\left[k(\eta_1 - \eta_2)\right] + \cos(2k\eta)\cos\left[k(\eta_1 + \eta_2)\right] \\ - \sin(2k\eta)\sin\left[k(\eta_1 + \eta_2)\right]\Big\}\,,\end{aligned} \tag{1.80}$$

which shows that the time dependence on η at late times results from rapidly oscillating contributions in the last two terms. Therefore, we can time average the result over a long enough time interval for which $k\eta \gg 1$ for each meaningful wavenumber k. The last two terms then average to zero, and we are left with

$$P_{h'}(k) = 18(1+c_s^2)^2 \int_{\eta_i}^{\eta_f} d\eta_1\, a(\eta_1)\mathcal{H}^2(\eta_1) \int_{\eta_i}^{\eta_f} d\eta_2\, a(\eta_2)\mathcal{H}^2(\eta_2) \cos\left[k(\eta_1-\eta_2)\right] U_\Pi(k,\eta_1,\eta_2)\,. \quad (1.81)$$

The determination of the GW power spectrum has thus been reduced into determining the unequal time correlator of the shear stress $U_\Pi(k,\eta_1,\eta_2)$ for the particular GW source in question. We take a quick look at various predicted GW sources in the next section, and return to this calculation in Chapter 5, where the GW power spectrum resulting from acoustic turbulence is calculated in the radiation dominated era both in the non-decaying and decaying cases.

1.4 Gravitational wave sources

This section provides a short overview on the potential gravitational wave sources that are the most relevant for GW astronomy. In order to produce a strong enough signal for detection, the gravitational waves need to stem from violent and powerful events, or from extremely massive objects moving at relativistic velocities. The GW sources can be divided into those of astrophysical and cosmological origin depending on the time of production during the evolution of the universe. Astrophysical sources consist of compact objects such as neutron stars and black holes, while cosmological sources originate from processes in the early universe, such as inflation and phase transitions (PTs). For cosmological sources the signal will always be stochastic while for astrophysical sources it can be either depending on the strength of the signal and whether it can be resolved for individual events.

Astrophysical sources

Supernovae

A supernova is a violent event that consists of a collapse and the subsequent explosion of a star during its last evolutionary stage. The process can lead to multiple different sources of gravitational waves [30–32], and can produce a compact object remnant like a black hole (BH), a white dwarf (WD), or a neutron star (NS), all of which are interesting sources when it comes to GW astrophysics.

Neutron stars

Neutron stars are small and extremely dense [33] remnants of massive stars that rotate very rapidly. While a spherically symmetric spinning object does not emit gravitational waves, neutron stars are believed to be capable of sustaining deformations, which are also called 'mountains', that result from the existence of a solid crust [34]. These imperfections lead to GW generation [35] at a constant rate because of the steady spin-rate of the star. This is why neutron stars are sometimes called sources of continuous gravitational waves.

Compact binary inspirals

Compact objects can form binary systems where the orbits of the objects decay over time due to energy being radiated away as gravitational waves [36]. This eventually leads to a coalescence that can be divided into three distinct stages: the inspiral, the merger, and the ringdown. This is the only detected GW source type at the time of writing, with the current GW detectors being able to detect GWs generated just before the merger for sources close enough to Earth [37].

Supermassive black holes

Supermassive black holes (SMBHs) have masses in the range of $10^5 - 10^{10}$ solar masses, and observational evidence points to there being one located at the centre of most (if not all) galaxies [38]. The GWs from SMBHs result from two sources: binary systems containing a stellar-mass compact object along with the SMBH, which lead to so-called extreme mass ratio inspirals (EMRIs) [39], and SMBH binaries in which both objects are SMBHs [40]. The latter can form in the collisions and mergers of galaxies.

Cosmological sources

Cosmic inflation

Cosmic inflation is a period of rapid expansion of space in the very early universe that is the current leading theory to explain some shortcomings in the hot Big Bang Model, like the horizon and flatness problems. Inflation also provides an explanation for structure formation via the stretching of quantum fluctuations [41] that form the required seeds for the development of the large-scale structure of the universe through coupling to the density perturbations [42]. In addition, regardless of the inflation model, this process produces tensor perturbations, that after re-entering the Hubble-radius form a SGWB [43]. Gravitational wave production is also believed to be possible during the reheating phase after inflation [44].

First-order phase transitions

The universe has undergone various phase transitions throughout its history. If these phase transitions are of first order, this would have led to the generation of GWs on the energy scale of the transition. Since this thesis focuses on a GW source that results directly from such phase transitions, we will provide a broader overview of them in Chapter 2.

Cosmic defects

Phase transitions could also lead to a production of topological defects that are relics of an earlier more symmetric phase of the universe [45, 46]. These defects can manifest as strings, domain walls, monopoles, or textures, and are called cosmic defects [47]. They form networks that present a scaling behaviour which leads to generation of GWs regardless of the order of the phase transition, the topology of the defect, or their global or gauge nature [48].

1.5 General overview of gravitational wave astronomy

The first direct detection of gravitational waves in 2015 opened a new window of observation into the universe. Since then, confirmed detections have given new insight on BH-BH [49] and NS-NS mergers [50], confirmed the existence of stellar BHs with masses larger than expected, and have set off the field of multi-messenger astronomy [51], where the data from a GW detection is used along with data from the electromagnetic (EM) counterpart to construct more detailed pictures of the studied phenomena [52]. The GW-EM findings have already provided information about the connection between binary neutron star merger progenitors and short gamma-ray bursts [53, 54], provided evidence that NS-NS mergers play a role in the production of heavy elements via r-process nucleosynthesis [55, 56], have confirmed the first detection of a kilonova [57, 58], and have constrained the fractional GW propagation speed difference to within 10^{-15} from that of the speed of light [53]. The detections have also provided tests of GR in regimes that are inaccessible via other experimental and observational methods [59]. However, these findings cover only a fraction of the potential that GWs have to offer. Hence, many new detectors are currently being planned and worked on [60], and the existing ones are being improved to reach higher sensitivity thresholds [61]. Future GW detectors and instruments working in tandem with each other, and with multi-messenger astronomy, can be used to study and constrain many phenomena in fundamental physics, astrophysics, and cosmology.

In the study of fundamental physics, GWs provide a way to test general relativity and theories of modified gravity. GW observations of SMBHs can be used to study the strong field limit of GR [62], and detections all the way down to the range of stellar mass BHs can be used to test GR over about ten orders of magnitude in length scale and twenty orders of magnitude in curvature [63]. Observing GWs at redshifts $z \sim 20$ will also impose strong constraints on local Lorentz invariance and graviton mass [64], which can be used to validate or rule out certain quantum gravity theories. Information from GW propagation could also shed light on the existence of potential large extra dimensions [65], and the study of their polarization [66] can be used to test some modified gravity theories. Observations of the ringdown from binary neutron star mergers allows for the study of ultra-high density matter and the corresponding equation of state [67]. The nature of matter in the inner core of a neutron star is currently unknown. Future detectors allow for the determination of the central densities and pressures in neutron stars [68], which can provide information on the possible quark matter nature of the inner core [69, 70] or the presence of a quark deconfining phase transitions during the merger [71].

On the side of astrophysics, future detectors enable increased detection rates of compact binary inspirals leading to proper measurement of the populations of binary systems [72], which can be used to model their formation and evolution, and to constrain models of stellar evolution [73]. Detections of WD-WD binaries will also become possible, yielding information on the structure of the Milky Way, and whether such binaries could be progenitors of type Ia supernovae [74], which are important in extragalactic distance measurements due to their role as standard candles. Increased detections of neutron star mergers will help better understand their significance in the formation of heavy elements [75]. Data obtained from detections of SMBH binaries and EMRIs will improve our

understanding of cosmic structure formation by providing constraints on the formation of SMBHs through tests of different models [76, 77]. Determination of the cosmic population of SMBH binaries will also shed light on the occupation fraction of SMBHs in galaxies, the merger rate of galaxies, and the correlation between galaxy masses and the mass of the central SMBH, along with providing information about the dynamical interactions between the SMBH and stellar objects in the galactic core [78]. Detections of SMBH binaries will also help in finding a definitive solution to the final parsec problem [79], i.e. whether SMBHs can be captured by each other and eventually merge in galaxy collisions, which could be a plausible astrophysical process according to evidence from some observations [80, 81], and if so, finding the mechanism behind the process.

Gravitational wave detections may also be of help in giving answers to many of the problems that plague modern cosmology, such as the accelerated expansion of the universe, the Hubble tension, and the nature of dark matter. Currently, the late universe measurements of the Hubble constant by cosmic distance ladder techniques, and early universe measurements from the CMB give results that differ from each other in a statistically significant manner [82]. The discrepancy in the values is known as the Hubble tension [83]. GW measurements provide a third independent way of determining the Hubble constant [84], which with the increased precision of future detectors can help in ruling out whether the tension is due to errors in the measurements, or new physics [85, 86]. Black hole and neutron star binaries can be used to study the properties of dark matter in many ways [87]. Future detectors also have the potential to detect primordial black holes [88] that could act as a dark matter component [89], and as a result, seeds for the formation of early galaxies. Independent measurements of the dark matter and dark energy densities will also be possible, along with measuring the equation of state for dark energy [90]. Lastly, GWs make for an unsurpassed, and seemingly the only viable, probe of the high-energy physics in the early universe that is beyond the reach of electromagnetic detection. Since the propagation of GWs is not influenced by matter, they still to this day contain direct information on the processes that created them and the conditions that prevailed in those times [22]. Therefore, a detection of a relic background of GWs from various early-universe phenomena like first-order phase transitions, inflation, or cosmic defects would give extraordinary information on the evolution of the universe.

However, the small cross-section causing the weak interactivity with matter is also the reason behind the difficulty of detecting GWs. Physically GWs appear as time dependent quadrupolar deformations of spacetime $h = \Delta L/L$, called strains, where L is a distance between two reference points, and ΔL is the displacement caused by a passing GW. These strains are extremely small, of the order of $h \sim 10^{-21}$ for a wave from a typical GW source. To put this into perspective, the distance of two objects separated by the diameter of the Earth would only stretch and squeeze by an amount equal to the size of an atomic nucleus when a gravitational wave passes by. Therefore, detection requires extremely complex instruments with many degrees of freedom that need to be managed with exceptional accuracy. The prevailing detection method is laser interferometry between freely suspended test masses. A Michelson interferometer, like the one in LIGO, consists of two arms that contain totally reflecting mirrors at their ends. A beam-splitter divides a laser beam into both of the arms, and after travelling back and forth a number of times (this increases the effective distance the beam travels), the beam is recombined at the beam-splitter. The resulting beam is sent to a photode-

tector that measures its intensity. Any variations in the arm lengths appear as phase differences in the laser beams, and leads to variations in the beam power at the photodetector. While this is the general principle behind GW interferometry, actual detectors are of course more complicated and need to account for many additional effects like, e.g. the diffraction of the beam, and various noise sources. Each detector has a certain sensitivity window based on its properties and limitations. For a comprehensive review, see Refs. [5, 91].

A SGWB appears as a component of noise in a single detector and can only be resolved if it matches or exceeds the detector noise level. Because the signal is expected to be below the noise level for any existing or planned detectors (except LISA), the strategy for detecting a SGWB involves cross-correlating two or more detectors [92, 93]. This method makes use of the different noise profiles of each individual detector. As an additional complication, the detected signal can consist of multiple individual SGWB signals. For example, a stochastic background from numerous unresolved astrophysical sources can mask a primordial background signal from the early universe, like in the case of extragalactic white dwarf binaries, whose background lies in the millihertz band [94]. There exists many data analysis methods that can be used as tools in separating the GW background from the instrument noise. For more information, see Refs. [95–99].

Each signal of relic GWs possesses a typical present day frequency, called the characteristic frequency, that depends on the redshift due to the expansion of the universe, and the dynamics of the GW production process. Considering a GW produced at time $t_\star$, and the fact that physical length scales are stretched proportionally to the scale factor, we find that its frequency today is redshifted as

$$f_0 = f_\star \frac{a_\star}{a_0} \,. \tag{1.82}$$

The universe can be treated as a closed system that conserves its energy as it expands. Therefore, the expansion can be treated as an adiabatic process, and the entropy per comoving volume S is conserved, giving [100]

$$S \propto g_S(T) T^3 a^3(t) = \text{constant} \,, \tag{1.83}$$

where T is the temperature, and g_S is the effective number of entropic degrees of freedom [101]. Using this to relate the temperature and the scale factor at present and GW production times with $a_0 = 1$, $T_0 = 2.7255\,\text{K}$ [102], the equation for the frequency can be written as

$$f_0 \simeq 7.80 \cdot 10^{-14} f_\star \left(\frac{106.75}{g_S(T_\star)}\right)^{1/3} \left(\frac{1\,\text{GeV}}{T_\star}\right) , \tag{1.84}$$

where g_S has been normalized to its Standard Model value at high energies. The value of $f_\star$ now depends on the GW sourcing process, but some estimates can be made for it on general grounds using causality. By defining a reduced wavelength of the GWs at the time of production using the horizon size as

$$\lambda_\star \equiv \epsilon_\star H_\star^{-1} \,, \tag{1.85}$$

we see that values $\epsilon_\star > 1$ correspond to super-horizon modes. On these length or timescales the source cannot be correlated, and the generation of these modes will be suppressed as a result of the additional damping caused by the expansion. The correlation scale of the GW source manifests itself as a peak in the GW power spectrum, which is thus expected to be smaller than the Hubble

radius. Therefore, the value of $\epsilon_\star$ satisfies $\epsilon_\star \leq 1$ depending on the lifetime of the source. Short-lasting sources include first-order phase transitions and reheating after inflation. For these sources, $\epsilon_\star$ will generally be a few orders of magnitude smaller than one. For sources that produce GWs continuously over long periods of time at constant energy density, like in the case of domain walls and cosmic strings, the source acts over a range of length and timescales, producing a wide spectrum, that today appears approximately flat for sources acting during the radiation dominated era [25]. This is also true for modes from inflation that enter the horizon during RD. In such cases, the only length scale in the spectrum is the Hubble length where the source becomes uncorrelated, and we expect $\epsilon_\star = O(1)$. During RD we can use the Friedmann equation (1.61) with the energy density – temperature relation [101]

$$\rho_{\mathrm{RD}} = \frac{\pi^2}{30} g_\star(T) T^4 \tag{1.86}$$

to write Eq. (1.84) by replacing the $f_\star$ obtained from $2\pi f_\star = H_\star/\epsilon_\star$. One can write the result as

$$f_0 \simeq 2.65 \cdot 10^{-8}\,\mathrm{Hz}\,\frac{1}{\epsilon_\star}\left(\frac{T_\star}{1\,\mathrm{GeV}}\right)\left(\frac{g_\star(T_\star)}{106.75}\right)^{1/6}, \tag{1.87}$$

where it has been assumed that the temperature is high enough that the effective number of relativistic degrees of freedom $g_\star$ equals that of g_S. The effects of the dynamics have now been isolated to the parameter $\epsilon_\star$. The equation shows that different GW sources operating at different times correspond to various characteristic frequencies today. Because $1/\epsilon_\star > 1$, the above equation can be used to determine the lowest possible frequency for a particular GW sourcing process. As a result, it is possible to associate different detectors with various early universe GW sources acting on different times based on their sensitivity and characteristic frequency ranges. Likewise, astrophysical GW sources also operate on a certain characteristic frequency range. These are shown in Figure 1.1 along with the estimated sensitivity curves of current and future detectors, which will be discussed next.

Individual gravitational wave detectors act as a part of a global network of detectors. This is advantageous for several reasons. Firstly, it enables the localization of the GW source by a triangulation process that requires at least three detectors located at different positions on Earth. Secondly, as mentioned before, it is beneficial for recognizing real gravitational wave signals from spurious ones by comparing different noise profiles between the detectors. Lastly, the personnel working as part of the network collaborate with each other by sharing their data and knowledge. A great effort is currently under way in planning and developing new next generation GW detectors to reinforce the network [104]. They can be divided into three categories: ground-based detectors, space-based detectors, and pulsar timing arrays.

Ground-based detectors

The ground based detectors are sensitive to GWs in the frequency range $O(1-10^3)$ Hz. In this range, the dominating GW sources are compact binary inspirals, and the yet to be observed supernovae and isolated neutron stars. The configuration for all ground-based detectors is enhanced Michelson interferometry with arm lengths varying on a detector-to-detector basis. The arms contain test masses in the form of suspended mirrors that are isolated from local forces and disturbances using

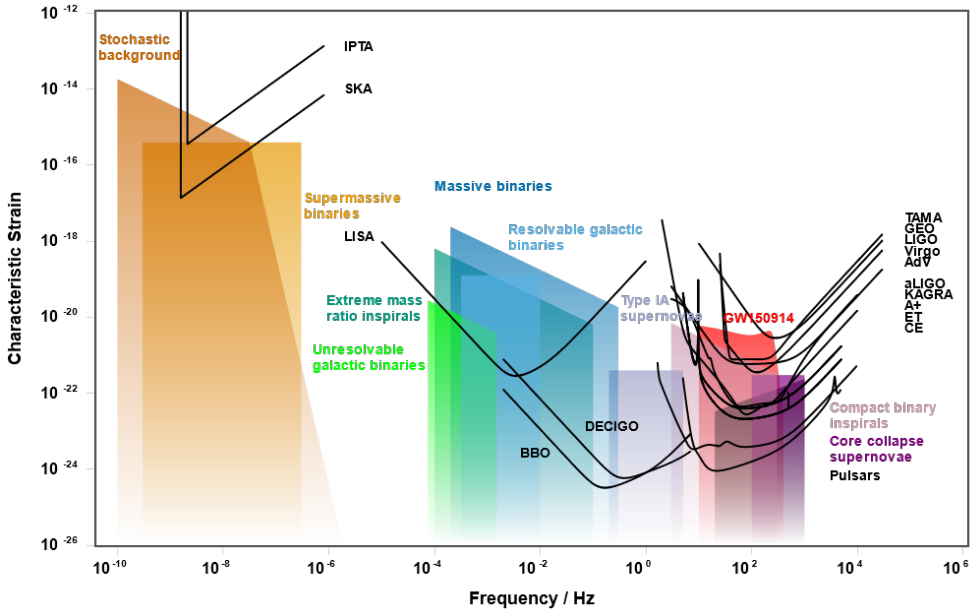

Figure 1.1: Estimated sensitivity curves of current and future GW detectors as a function of the frequency. Also shown are the estimated frequency ranges and characteristic strains for various GW sources. The figure is obtained using the tools of Ref. [103].

various techniques. The sensitivity of ground-based detectors is limited in the low frequency range by seismic noise that is imbued by ambient ground motion [105], in the intermediate frequency range by thermal noise resulting from the test masses and their suspensions [106–108], and in the high frequency range by the so-called laser shot noise that stems from resolution limiting vacuum fluctuations of the EM field in the photodetector [109].

The first generation of GW detectors consisted of four detectors, those being TAMA, GEO 600, Virgo and LIGO. TAMA [110], located in Japan, and GEO 600 [111], located in Germany, are smaller detectors with arm lengths of $L = 300\,\mathrm{m}$ and $L = 600\,\mathrm{m}$ respectively that have been important for testing various technical aspects of second generation detectors. LIGO (Laser Interferometer Gravitational-wave Observatory) [112] is located in the United States at two different locations. The site in Washington state contains two detectors, H1 with arm length $L = 4\,\mathrm{km}$ and H2 with $L = 2\,\mathrm{km}$. The site in Louisiana bases the L1 detector that also has 4 km long arms. Virgo [113] is a European-based detector located in Italy with 3 km arms. With the level of sensitivity reached by these first generation detectors, detection was not guaranteed. The detectors have been regularly upgraded to reduce the noise sources to improve sensitivity. In 2015 LIGO completed an upgrade that transformed it into advanced LIGO (aLIGO) and increased its sensitivity by about a factor of ten, which increased its ability to probe the sky by about a factor of one thousand. This enabled the first direct detection of gravitational waves in February 2016 [6]. The advanced Virgo detector joined the network in spring 2017, and the japanese KAGRA (Kamioka Gravitational Wave Detec-

tor) [114] in February 2020. The advanced versions of LIGO and Virgo along with KAGRA form the current network of second generation detectors. KAGRA ($L = 3\,\text{km}$) also acts as a path-finder for the next generation of detectors by acting as a testbed for new technologies, and by being located underground. LIGO-India [115] is planned to be joining the network in 2030, leading to a great improvement in the network's ability to detect and locate GW sources [116]. After the end of the O4 observation run in 2025, the advanced Virgo and advanced LIGO are both being upgraded, the new improved versions being designated as Adv+ and A+, which is expected to yield a more than twofold improvement in sensitivity levels [117].

However, the current detectors cannot be improved indefinitely due to intrinsic limitations in their infrastructure. Therefore, the design phase for future GW detectors, the so-called third generation detectors (3G), is already under way. The two leading projects are the European-based Einstein Telescope (ET) [118] and the USA-based Cosmic Explorer (CE) [119] that are currently being pursued in parallel. New techniques and increase in the base arm length L are targeting a tenfold increase in the sensitivity compared to the current second generation detectors, leading to another one thousand time increase in the volume of the universe being scanned, and shifting the lowest detectable frequency close to 1 Hz. This makes possible the detection of intermediate-mass black hole mergers with masses in the range of $10^2 - 10^4$ solar masses, which can be used to study the formation of heavier black holes. The detectors can also probe the stochastic GW background [120]. The currently proposed design for ET consists of three co-located interferometers in a triangular configuration with arm lengths $L = 10\,\text{km}$ [121]. This allows for the measurement of the two GW polarization states, and the utilization of a time-delay interferometry technique [122, 123]. ET is also going to be located underground to reduce seismic noise. CE is planned to keep the on-surface L configuration, but with an increase to the arm lengths of up to 40 km [124]. Both detectors are aiming to begin operation in the 2030s. An additional Australian 3G detector called the Neutron star Extreme Matter Observatory (NEMO) [125] has also been proposed to study GWs from neutron stars.

Space-based detectors

Space-based GW detectors operate using the same principles as their Earth-based counterparts, but enable the opening of a completely new observational band in the frequency range $\mathcal{O}(10^{-5}–10^{-1})$ Hz as a result of greatly increased baseline arm lengths of $\mathcal{O}(10^6)$ km, and the lack of seismic noise that is one of the main limiting factors for ground-based detectors. In space the strength of the local gravitational field is also much less than on Earth, erasing the need for the suspension of the test masses, with them being allowed to drift freely. However, operating a detector in space brings about new noise sources and challenges, like gravitational and electromagnetic stochastic noises in the very low frequency induced by thermal drifts. The test masses must also be protected from exposure to various kinds of radiation and residual particles. This is done by shielding the test masses inside the spacecraft with a protective housing, inside which the masses are allowed to drift freely. The test masses are protected from contact with the spacecraft, and from electrostatic and gravitational couplings to it by a controlling technique called drag-free control [126]. The feasibility of space-based detectors and the management of many of these challenges were tested by the LISA

Pathfinder spacecraft in 2016. The results were found to fully meet, and depending on the frequency range, even exceed the requirements [127, 128] for the first upcoming space-based observatory LISA.

Following the success of the Pathfinder, LISA (Laser Interferometer Space Antenna) [129] was approved as one of the main research missions of the European Space Agency (ESA) in 2017. The mission was formally adopted by ESA in January 2024, and the building phase of the spacecraft and its instruments is set to begin in 2025. The launch of LISA is currently planned for circa 2035. It will be the first detector capable of surveying the entire universe with gravitational waves. The configuration of LISA will be as follows: it consists of three drag-free spacecraft that form an equilateral triangle with side-length (i.e. arm length) $L = 2.5 \cdot 10^6$ m. It will orbit on an Earth-like orbit around the Sun, 20 degrees behind the Earth. Because of the large distance between the spacecrafts, reflection of the laser beam by mirrors is not possible. Instead, LISA uses two laser beams on each arm that are being sent and received by the spacecrafts. Hence, each spacecraft contains two test masses and two laser links. The interferometry signal is then constructed from the arm length information of the three arms. The benefits of the three spacecraft configuration include protection against component failures, and the use of the time-delay interferometry technique mentioned earlier when discussing the Einstein Telescope.

The configuration for LISA described above yields a sensitivity range in the band between 0.1 mHz and 0.1 Hz, which is expected to contain signals from various sources, such as stellar-origin BH binaries, galactic WD and NS binaries, massive BH binaries in the range $10^4 - 10^7$ solar masses, and EMRIs. Therefore, LISA will be able to study many of the topics mentioned at the start of this section. For more information, see the LISA science goals in Ref. [129]. Most interestingly, at least when it comes to the topic of this thesis, one of LISA's goals is the direct detection of a stochastic GW background of cosmological origin, whose presence is also expected in the aforementioned frequency band.

Other proposed concepts for space-based detectors include the DECIGO (DECi-hertz Interferometer Gravitational Wave Observatory) [130, 131] and BBO (Big Bang Observer) [132, 133], which are both based on a similar design. Both consist of four LISA configurations so that two of them form a hexagram, and the remaining two triangles are on the same orbit, one ahead, and one behind by an angle of $2\pi/3$. The arm length would also be smaller than in LISA, probing the frequency band between $0.1 - 10$ Hz. The main science objective of these missions would be the detection of a SGWB from inflation. However, these are planned as successors to LISA, putting their potential launch dates many decades into the future.

Pulsar timing arrays

Unlike the detectors in the previous two categories, pulsar timing arrays (PTAs) do not utilize laser interferometry in their search of gravitational waves. Instead, they make use of millisecond pulsars. Pulsars are rotating neutron stars that are highly magnetized. They emit a beam of radiation in the direction of their magnetic axis that does not necessarily align with the rotational one. The pulsar thus has two beams that always sweep the same areas of the sky as the pulsar rotates, similarly to light beams from a lighthouse. This is why pulsars are sometimes called cosmic lighthouses. As a pulsar rotates and keeps sweeping pass the area of the sky that contains Earth, we see it as a

periodic pulsating radio source in the sky. Pulsars with rotational periods of a few milliseconds are extremely stable rotationally, and are comparable to the best atomic clocks as timing sources [134]. This so-called pulsar timing method can be used to detect gravitational waves, since the presence of a SGWB leads to a frequency shift in the arrival time of the pulses. However, there are multiple other sources that could lead to the detection of these timing residuals. Therefore, by observing just a single pulsar, it is not possible to deduce the origin of the individual timing residuals. The strategy thus is to observe multiple pulsars distributed over the sky. Statistical treatment of this array of pulsars will then enable the observation of the GW background, since the timing residuals from different pulsars are correlated for a SGWB [135, 136]. This correlation is a function of only the angular separation of the pulsars on the sky. Enough time is needed in order to properly localize and understand the individual properties of each pulsar in the array. Therefore, the timescale of PTA experiments is measured in years. As the maximum sensitivity is obtained by the inverse of the total observation time, PTAs enable the search of GWs roughly in the frequency band $O(10^{-9} - 10^{-6})$ Hz. The most promising signals that lie in this range are those from SMBH binaries [137, 138]. The first detection is expected to be the SGWB from inspiralling SMBH binaries [139, 140].

Multiple PTA collaborations exist currently, some of which have been collecting data already since the year 2005. The three major PTA consortiums are the Parkes PTA (PPTA) [141] located in Australia, the European PTA consortium (EPTA) [142, 143], and the North American Nanohertz Observatory for Gravitational Waves (NANOGrav) [144]. Together with the Indian Pulsar Timing Array Project (InPTA) [145] they form the International Pulsar Timing Array (IPTA) [146, 147] that times a global array of approximately 100 millisecond pulsars using some of the largest radio telescopes in the world. In June 2023 the consortiums announced that they had found evidence for a SGWB [148–153]. At the time of writing, the results do not yet fulfil the 5σ-significance that is the standard for detection, but this threshold is expected to be reached in the near future as more data is brought in.

The sensitivity of PTAs will be increased in the near future as a result of improvements in the timing precision, total observation time, and an increase in the number of pulsars that will be observed [154]. The soon-to-be finished Square Kilometer Array (SKA) [155] and the proposed ngVLA (next generation Very Large Array) [156] will lead to further improvements in detection, which could make some individual sources separable from the background [157].

2. Cosmological first-order phase transitions

First-order phase transitions (FOPTs) [158] proceed by nucleation and expansion of bubbles containing the new cold-temperature phase, causing violent stirring in the fluid. If such a transition were to take place in the early universe, it would provide a strong source of primordial gravitational waves. This chapter discusses the cosmological phase transitions predicted by the Standard Model, and the motivation for them being of the first order in some beyond the Standard Model theories. We also take a look at the mechanism that governs the phase transition, the dynamics of the phase transition through bubble nucleation and growth, and in the end discuss the various individual GW generating processes that follow.

2.1 Beyond the Standard Model

The Standard Model (SM) is the most successful particle physics theory developed thus far. It classifies all known elementary particles and provides descriptions for the strong, weak, and electromagnetic interactions in the framework of renormalizable quantum field theory [159]. As the universe cools down due to its adiabatic expansion, it will go through phase transitions that lead to changes in its structure when some symmetry in the underlying particle physics theory is being broken. The Standard Model predicts two such transitions.

The most recent phase transition in the universe took place as a result of the spontaneous breaking of the chiral symmetry of QCD (quantum chromodynamics). QCD is the theory of the strong interaction that at low temperatures confines quarks into hadrons through gluons that mediate the interaction. The strong force is said to be asymptotically free because its strength scales with the energy scale, becoming weaker at high energies [160]. At a high enough energy scale, the strong interaction can no longer confine the quarks, and they become deconfined, forming a quark-gluon plasma. In the early universe, the quarks become confined at a critical temperature of about $T = 150\,\mathrm{MeV}$ [161], and the associated phase transition from quark-gluon plasma to hadrons is known as the QCD phase transition.

The other phase transition resulted from the spontaneous breaking of the electroweak (EW) symmetry. At energies above approximately $T = 160\,\mathrm{GeV}$ [162], the weak and the electromagnetic interactions merge into a single electroweak interaction. The splitting of the forces and the breaking of the EW symmetry activates the Higgs mechanism, which gives masses to the $\mathrm{W}^{\pm}$ and Z bosons

through their interactions with the Higgs field. The corresponding phase transition in the early universe is called the electroweak phase transition.

Lattice simulations have shown that in the SM both the QCD [163] and the EW [164] phase transitions are second order transitions corresponding to a crossover. A crossover is a transition where the system (in our case the universe) evolves from the symmetric phase to the broken phase smoothly without significant deviations from thermal equilibrium. Therefore, this kind of transition would not result in significant GW generation. However, this does not definitely rule out the possibility of either or both of these transitions being of the first order. It is known that the SM is not a complete description of fundamental physics as it fails to explain or solve many physical phenomena. It contains only three out of the four fundamental interactions, as there is seemingly a fundamental incompatibility between quantum mechanics and gravity, which is one of the biggest problems in modern physics. Cosmological observations and the Lambda-CDM model indicate that the composition of the universe is about 5% baryonic matter, 27% dark matter, and 68% dark energy [13]. Yet, the SM does not contain any suitable dark matter candidates, and treating dark energy as the energy of the vacuum in the SM leads to the so-called cosmological constant problem – a massive discrepancy of 50 to 120 orders of magnitude in the value of the vacuum energy density compared to observations [165]. Observations of neutrino oscillations confirm that neutrinos should have tiny non-zero masses [166], contradicting the SM, where neutrinos are massless. The universe today has a positive baryon number density, meaning that there must have been some mechanism that led to an asymmetry in the amount of matter and antimatter, assuming they were created in equal amounts to begin with. This process is called baryogenesis [11], and the SM does not contain a viable mechanism for it. There are also hierarchical problems related to the magnitude of some quantities, like that of the Higgs mass [167], and the strong CP problem [168], that hint at physics beyond the Standard Model. Attempts to solve these issues have spawned various extensions to the SM and many theories that go beyond it. The behaviour of matter at energy scales above the electroweak scale is poorly understood because they cannot be probed by the existing particle colliders. This leaves the door open for many of these particle physics theories, and determining which one is most in line with reality can only be carried out via experiments and observations. Current particle collider experiments do not constrain the order of the electroweak phase transition [25], and there are several models within collider bounds that can lead to a first-order transition [169].

A first-order phase transition can be obtained on the electroweak scale by extending the Standard Model with the addition of an extra scalar field. One such model is the Next-to-Minimal Supersymmetric Standard Model (NMSSM) [170, 171] that is a supersymmetric singlet extension of the SM and can lead to a strong first-order transition in a regime where there is a two-step transition [172]. Examples of non-supersymmetric extensions with a FOPT include real scalar singlet models [173–175] and two-Higgs doublet models [176, 177]. In some models, a strong first-order transition is obtained as a result of introducing dimension-six operators in the Higgs potential [178, 179]. There are factors that can also affect the order of the QCD transition, such as the lepton asymmetry, which is poorly constrained by observations [180]. A large lepton asymmetry could render the QCD transition first order [181]. Some models containing warped extra dimensions that are developed to solve the hierarchy problems in the SM, like Randall-Sundrum models, can also lead to FOPTs even

outside the QCD and EW scales [182, 183].

The reason a first-order phase transition at the electroweak energy scale is such a compelling prospect is that it provides one of the most promising mechanisms for baryogenesis [184]. In order for baryogenesis to occur, the interaction responsible for the baryon asymmetry must fulfil the following three so-called Sakharov criteria [185]:

1. Baryon number violation.

2. C and CP violation.

3. Departure from thermal equilibrium.

The first condition is obvious in order to transition from baryon symmetric state to an antisymmetric state. The charge (C) and charge parity (CP) conjugation violations are required in order to shift the interaction to favour the production of baryons instead of antibaryons. A departure from thermal equilibrium is required because otherwise the baryon number and CP violating process would be compensated by a counter process, leading to zero net baryon number variation. The last condition can also only be fulfilled in a homogeneous and isotropic universe if massive particle species are present [186]. Electroweak baryogenesis can satisfy all of these conditions if the corresponding phase transition is of the first order [184, 187]. A FOPT leads to a sudden departure from equilibrium when compared to the Hubble time, and in many models the creation of the baryon asymmetry is explained by the subsequent interaction between the plasma and the expanding bubble walls that act as the phase boundaries. One such explanation is that the interaction produces asymmetries that lead to CP violation through scattering of particles off the bubble walls. This asymmetry then gets transformed into a baryon asymmetry though baryon number violating processes involving non-perturbative electroweak interactions (called sphaleron interactions) that take place in the vicinity of the expanding bubble walls [188].

Cosmological first-order phase transitions are also of interest due to the potential in their detectability. The typical frequency of GWs generated from such a transition can be estimated by the relation $2\pi f_\star = \beta$, where β is the inverse time duration of the transition. Substituting this into the equation for the characteristic GW frequency today obtained in the previous chapter, Eq. (1.87), one approximately obtains

$$f_0 \sim 10^{-6} \left(\frac{\beta}{H_\star}\right) \left(\frac{T_\star}{100\,\mathrm{GeV}}\right) \mathrm{Hz}\,, \tag{2.1}$$

where the PT temperature $T_\star$ has been normalized to the EW energy scale, and $g_\star$ has been replaced by its high temperature value. The peak frequency now depends on the ratio between the expansion rate of the universe, and the PT duration. This dimensionless quantity is a fundamental parameter of the GW signal. The PT must progress faster than the universe expands for it to complete, which means $\beta/H_\star > 1$. From Eq. (2.1) one can then see that in the case of the EW transition the peak of the GW signal lies in the LISA band for values $1 \lesssim \beta/H_\star \lesssim 10^5$. The exact value of the ratio depends on the model, but in general, its typical values are expected to lie in the range $10 - 10^3$ [17]. This means that a GW signal generated by a first-order EW phase transition peaks in the LISA band and should be detectable by LISA if the signal is strong enough to exceed the sensitivity of the instrument.

Normalizing for the QCD transition instead, the characteristic frequency roughly becomes

$$f_0 \sim 10^{-9} \left(\frac{\beta}{H_\star}\right) \left(\frac{T_\star}{100\,\mathrm{MeV}}\right) \mathrm{Hz}\,. \tag{2.2}$$

Therefore, the QCD phase transition lies in the frequency window of PTAs for small values of $\beta/H_\star$.

In conclusion, while the Standard model does not predict a first-order phase transition in the early universe, uncertainties in the cosmological model at early times and uncertainties in the particle physics model at high energies still leave room for factors that could render the QCD or the EW transition first order. The main motivations for studying cosmological FOPTs are that, firstly, they offer a promising mechanism for the baryon asymmetry through electroweak baryogenesis, and, secondly, they would act as strong sources of GWs that could be detectable with future GW detectors. Such a detection would give extraordinary information about high energy physics and conditions in the early universe that could not be obtained by other means.

2.2 Spontaneous symmetry breaking

The mechanism that initiates and describes a phase transition in the early universe is called spontaneous symmetry breaking [189]. In particle physics theories symmetries tend to be restored at high temperatures, an example of which is the previously mentioned unification of the weak and electromagnetic forces into a single electroweak interaction*. Consequently, as the universe cools down, these symmetries are spontaneously broken, which leads to changes in the physical properties of the universe. These changes manifest themselves as phase transitions.

Phase transitions can be described using mean field theory where the degree of order in the system is quantified by an order parameter that usually has the value of zero in the symmetric phase, and a non-zero value in the phase where the symmetry has been broken [190]. The former is also called the ordered or low-temperature phase, and the latter the broken, disordered, or high-temperature phase. The temperature at which the order parameter becomes non-zero is called the critical temperature. The way the order parameter changes from zero determines the phase transition type, also called the order. If the order parameter grows continuously, the phase transition is said to be a continuous or a second-order phase transition. If there is a discrete jump in the value of the order parameter, the phase transition is called a discontinuous or a first-order phase transition.

The mechanism behind a first-order phase transition can be demonstrated using a temperature dependent effective potential [191]

$$V(\phi, T) = D(T^2 - T_0^2)\phi^2 - ET\phi^3 + \frac{1}{4}\lambda(T)\phi^4\,, \tag{2.3}$$

where D, E, and T_0 are strictly positive constants and $\lambda(T)$ is a slowly varying function in the temperature T. This kind of potential is motivated by the computation of the electroweak one-loop effective potential at finite temperature in the SM under the approximation that the Higgs mass is smaller than the mass of the W boson†. The constants D and E, and the function $\lambda(T)$ are then

*This has also led to a prediction that at even higher temperatures the three gauge interactions of the Standard Model could all be united into a single force. These kinds of models are called Grand Unified Theories (GUTs).

†This is not the case in reality, which is why there is no first-order phase transition at the EW scale in the SM.

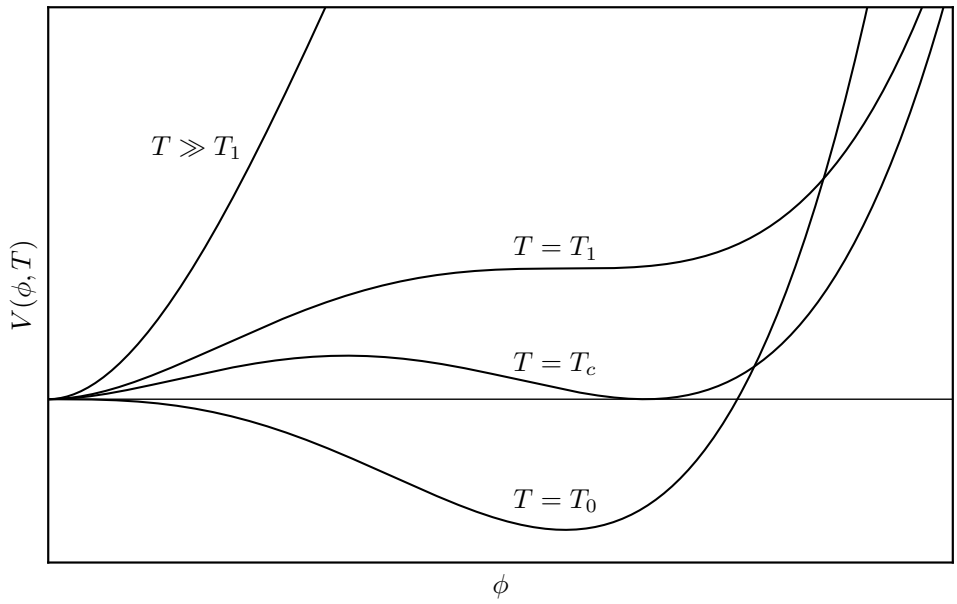

Figure 2.1: The shape of the effective potential of Eq. (2.3) at various temperatures. At T_1 a second extremum develops, which splits into a minimum and a maximum at $T < T_1$. At the critical temperature $T = T_c$ the second minimum becomes degenerate with the minimum at the origin. At $T < T_c$ the second minimum becomes the global minimum, but the field remains trapped in the false vacuum state at the origin due to a potential barrier that is induced by the maximum. The barrier exists at the temperature range $T_0 < T < T_c$, vanishing at $T = T_0$, at which point the origin becomes a maximum.

functions of the SM particle masses [186, 192, 193]. The potential has three extrema, computed from $dV/d\phi = 0$, located at $\phi_0 = 0$ and

$$\phi_\pm(T) = \frac{3ET}{2\lambda(T)}\left(1 \pm \sqrt{1 - \frac{8D\lambda(T)(T^2 - T_0^2)}{9(ET)^2}}\right). \tag{2.4}$$

At temperatures $T > T_1$, where T_1 can be solved from the equation

$$T_1^2 = \frac{T_0^2}{1 - 9E^2/8D\lambda(T_1)}, \tag{2.5}$$

the square root in the previous equation is imaginary, and the only extremum in the system is the minimum at the origin ϕ_0 where $V = 0$. The order parameter of the system is the value of the field ϕ at temperature T that always favours the lowest energy state, that is, the global minimum of the system, also called the true vacuum state. The value of the field in this state is called the vacuum expectation value. Therefore, the field initially lies in the true vacuum at the origin, which is symmetric with respect to $\phi \leftrightarrow -\phi$.

At $T = T_1$ a second extremum, a saddle point, develops at

$$\phi_1 = \frac{3ET_1}{2\lambda(T_1)} \,. \tag{2.6}$$

At $T < T_1$ the saddle point splits into a global maximum located at ϕ_-, and a local minimum at ϕ_+. The value of the potential at the local minimum is called the false vacuum state. As the temperature decreases further, the local minimum gets lower and lower until at a critical temperature T_c it coincides with the true vacuum at the origin, i.e. $V(\phi_+, T_c) = 0$. The critical temperature can be calculated by computing the roots of Eq. (2.3). The true and the false vacua are degenerate when the potential has only a single root in addition to the one at the origin, so using the solution of the resulting quadratic equation gives the result

$$T_c^2 = \frac{T_0^2}{1 - E^2/D\lambda(T_c)} \,. \tag{2.7}$$

Using this in Eq. (2.4) gives the locations of the maximum and the minimum at T_c as

$$\phi_-(T_c) = \frac{ET_c}{\lambda(T_c)} \,, \qquad \phi_+(T_c) = 2\phi_-(T_c) \,. \tag{2.8}$$

At $T < T_c$ the minimum ϕ_+ becomes the global minimum and the new true vacuum state, resulting in a change in the vacuum expectation value of the system. The order parameter would now like to transition from the origin to the new energetically favoured true vacuum but cannot do so because the maximum ϕ_+ acts as a barrier between the two states, meaning that the field is trapped in a metastable state in the false vacuum. The field can tunnel through the barrier either by quantum tunnelling or thermal fluctuations. Crossing the barrier this way leads to an instantaneous and discrete change in the order parameter, breaking the $\phi \leftrightarrow -\phi$ symmetry, and giving rise to a first-order phase transition. The barrier in the potential results from the cubic term in Eq. (2.3) – without it, the origin would become a global maximum at temperatures below the critical temperature, and the field would smoothly and continuously roll to the new true vacuum state, leading to a second-order phase transition.

The details of the phase transition and the temperature at which the phase transition occurs, denoted by T_n, depend on the tunnelling process through the barrier. The tunnelling does not take place instantaneously at $T = T_c$, so the system first supercools until the phase transition takes place at a temperature $T_n < T_c$. At $T = T_0$ the barrier disappears, as $\phi_-(T_0) = 0$, and the origin becomes a global maximum. The minimum is then located at

$$\phi_+(T_0) = \frac{3ET_0}{\lambda(T_0)} \,. \tag{2.9}$$

If the tunnelling effect is small and the field has not yet crossed the barrier by this point, the phase transition would proceed as a second-order one. In the opposite case, the transition occurs at $T_0 < T_n < T_c$ via tunnelling through the potential barrier, which manifests as nucleation of true vacuum bubbles in the false vacuum space. The nucleation of these bubbles and their dynamics is the topic of the next section. The effective potential $V(\phi, T)$ has been sketched in Figure 2.1 at the various labelled temperatures featured in this section.

2.3 Bubble nucleation and growth

The discontinuous jump in the order parameter that triggers the phase transition also leads to a discontinuity in the energy density between the preceding high- and the ensuing low-temperature phase. This energy difference between the phases is called latent heat and the system requires a mechanism that dissipates or transports this released excess energy away. The mechanism in question is the nucleation and expansion of spherical bubbles that contain the new low-temperature phase, with their walls acting as phase boundaries. These bubbles nucleate with an increasing rate randomly all over the fluid as the PT proceeds, and the difference in energy density between the phases causes the bubbles to expand. This in turn transfers the released latent heat into gradient energy of the bubble walls, bulk fluid motions, and thermal energy of the fluid. The phase transition comes to an end when all bubbles have collided and merged with the neighbouring ones, converting the entire system into the new low-temperature phase.

To look at bubble nucleation in more detail, let us denote the energy density released, that is the latent heat, by ρ_{vac}. Then a nucleation of a spherical bubble of radius r at temperature T results in an energy release of $(4\pi/3)r^3\rho_{\text{vac}}(T)$. However, crossing the barrier also requires energy, which manifests as a positive energy contribution associated with the surface tension of the bubble σ, giving the total free energy of the bubble as

$$G(r,T) = 4\pi r^2\sigma - \frac{4\pi}{3}r^3\rho_{\text{vac}}(T)\,. \tag{2.10}$$

The dynamics of the bubble result from the competition between these two terms. Due to their different scaling with respect to the bubble radius, there exists a critical radius

$$r_c(T) = \frac{3\sigma}{\rho_{\text{vac}}(T)}\,, \tag{2.11}$$

at which the two contributions are equal. For a bubble that is nucleated with $r < r_c$, the surface tension dominates, and the bubble collapses and vanishes. Only large enough bubbles with $r > r_c$ survive and begin to expand due to a pressure difference between the phases. The quantity ρ_{vac} depends on the potential difference between the true and the false vacua*, $\Delta V = V(\phi_0,T) - V(\phi_+,T)$, which means that for temperatures just below T_c, the latent heat ρ_{vac} is small, and the critical radius is large. The probability of nucleating a large bubble is small, so the nucleation rate of supercritical bubbles with $r > r_c$ is also small at first. As the temperature decreases, ρ_{vac} increases and r_c gets smaller, increasing the nucleation rate of supercritical bubbles. The expansion rate of the universe sets a timescale against which the bubble nucleation rate must be compared. If the nucleation rate of supercritical bubbles $\Gamma(T)$ is small compared to the Hubble expansion rate $H(T)$, the universe cools down considerably before the nucleation of supercritical bubbles becomes likely. If T_0 is reached before this point, the phase transition would proceed as a second-order one. Hence, a first-order phase transition occurs if for some temperature T_n in the range $T_0 < T_n < T_c$ the nucleation rate satisfies $\Gamma(T_n) \sim H(T_n)$, i.e. if it grows comparable to the Hubble rate before T_0 is reached.

*To be more precise, in addition to the potential difference, the latent heat depends also on the entropy variation so that it can be written as $\rho_{\text{vac}} = -\Delta V - T\Delta s$.

The bubble nucleation rate can be computed as the tunnelling rate through the potential barrier using finite temperature quantum field theory. The derivation is rather long, and its details are not very relevant for the topic of this thesis, so we skip straight to the results. The computation can be found in Refs. [17, 194–197]. In the case where $V(0,T) = 0$, the nucleation rate per unit volume can be written as [198]

$$\frac{\Gamma}{V} = A(T)e^{-S(T)}\,, \tag{2.12}$$

where $A(T)$ is a prefactor proportional to (mass)^4. The only relevant mass scale in the high temperature limit is the temperature itself, so we have $A(T) = aT^4$, where a is of order one*. $S(T)$ is the Euclidean action of an instanton solution (also called the "critical bubble") that for thermal transitions is given by S_3/T, where the three-dimensional action is spherically symmetric in the high temperature limit

$$S_3 = 4\pi \int_0^\infty r^2 dr \left[\frac{1}{2}\left(\frac{d\phi_b}{dr}\right)^2 + V(\phi_b, T)\right] \tag{2.13}$$

and also acts as the free energy of the critical bubble. The quantity ϕ_b is the profile of the critical bubble that satisfies the so-called bounce solution, obtained from the equation

$$\frac{d^2\phi_b}{dr^2} + \frac{2}{r}\frac{d\phi_b}{dr} - \frac{\partial V(\phi_b,T)}{\partial \phi_b} = 0\,, \qquad \left.\frac{d\phi_b}{dr}\right|_{r=0} = 0\,, \qquad \lim_{r\to\infty}\phi_b(r) = 0\,, \tag{2.14}$$

with the two initial conditions also displayed above that make the action finite and regular at the origin. Using this, one can obtain the time t_n at which the phase transition occurs by requiring that the total number of bubbles nucleated between $t = 0$ and $t = t_n$ in a Hubble volume $H^{-3}(t)$ is of order one, giving the relation

$$\int_0^{t_n} dt \frac{\Gamma(t)}{VH^3(t)} = O(1)\,. \tag{2.15}$$

This can also be written in terms of the phase transition temperature T_n by using the scaling relation $T \propto 1/a$ that follows from the adiabatic expansion of the universe in Eq. (1.83), and changing the integration variable with the relation $dT/T = -Hdt$.

The equation (2.12) provides the complete information on the bubble nucleation rate. As a result of the exponential scaling, most of its time variation lies in the action $S(T)$. Taylor expanding it to first order around $t = t_n$ yields

$$S(T) \approx S(T_n) + (t - t_n)\left.\frac{dS(T)}{dt}\right|_{t=t_n}\,, \tag{2.16}$$

from which we define

$$\beta \equiv -\left.\frac{dS}{dt}\right|_{t=t_n} \approx \frac{1}{\Gamma}\left.\frac{d\Gamma}{dt}\right|_{t=t_n} \tag{2.17}$$

as the time variation of the bubble nucleation rate. To obtain the approximate result on the right, equation (2.12) is used with the assumption that the prefactor A varies in time much slower than Γ. After substituting the Taylor expansion to Eq. (2.12), one can write the nucleation rate as

$$\Gamma(t) \approx \Gamma_n e^{\beta(t-t_n)}\,, \tag{2.18}$$

*A more rigorous form for the prefactor $A(T)$ is given in the earlier Refs. that contain the full calculation. In practice, it depends on determinants whose computation requires numerical treatment.

which shows that in the neighbourhood of the phase transition time the bubble nucleation rate grows exponentially. From this approximation it is evident that the parameter β also sets the timescale of the transition, its duration given roughly by $\Delta t \sim \beta^{-1}$. Writing equation (2.17) in terms of the temperature yields

$$\frac{\beta}{H_n} = T_n \frac{dS}{dT}\bigg|_{T=T_n} = T_n \frac{d}{dT}\left(\frac{S_3}{T}\right)\bigg|_{T=T_n}, \tag{2.19}$$

from which the dimensionless ratio β/H at the time of the phase transition can be computed numerically after determining the transition temperature T_n and the potential $V(\phi_b, T)$. This is an important factor in determining the strength of the GW signal from phase transitions, and also affects its characteristic frequency, as seen at the end of section 2.1. The factor β also sets the typical scale of the bubbles at the end of the transition as $R_\star \approx v_w \beta^{-1}$, where v_w is the bubble wall speed that can be taken to be approximately a constant*. It is good to note that the above results are analytic approximations based on the assumption that β is positive and that the action $S(t)$ can be linearized, both of which can break down in the limit of very strong transitions [201]. The linearization in Eq. (2.16) is a very good approximation in the limit $S \gg 1$ and $\beta \gg H$.

Another important quantity in a first-order phase transition is the ratio between the latent heat released in the transition and the radiation energy density of the universe at the time of transition

$$\alpha \equiv \frac{\rho_{\text{vac}}}{\rho_{RD}(T_n)}, \tag{2.20}$$

where the normalization in terms of the radiation energy density ρ_{RD} defined in Eq. (1.86) is chosen because we are interested in transitions taking place during the radiation dominated era. The quantity α tells how much energy is available to be transferred to bubble and fluid motions, and thus characterizes the strength of the transition. The height of the potential barrier $V(\phi_-, T)$ compared to the depth of the minimum $|V(\phi_+, T)|$ also has an effect on the profile of a nucleated bubble. Early on when $V(\phi_-, T) \gg |V(\phi_+, T)|$ for temperatures just below T_c the bounce solution $\phi_b(r)$ in Eq. (2.14) changes very quickly from $\phi_b = 0$ outside the bubble ($r > R$) to $\phi_b = \phi_+$ inside the bubble ($r < R$). These correspond to thin wall bubbles and are formed early on in the transition. In the opposite case where the barrier has decayed away and the minimum is deeper for temperatures close to T_0, i.e. $V(\phi_-, T) \ll |V(\phi_+, T)|$, the change in ϕ_b happens slowly, and thick wall bubbles are obtained. Whether the transition proceeds by thin or thick wall bubbles, or by something from between, depends on the bubble nucleation rate at the transition temperature $\Gamma(T_n)$. The wall thickness is the other important length scale of the system along with $R_\star$, and decreases as a bubble expands.

The bubble wall speed v_w is determined by microscopic interactions between the expanding bubble wall and the surrounding fluid particles. This manifests as a friction that slows down the bubble expansion until an equilibrium is reached when the pressure expanding the bubble and the friction are equal. A typical assumption is that the bubble wall speed becomes a constant quickly

*The result for the mean bubble separation $R_\star$ presented here holds in general only for detonations and is often accompanied by an additional prefactor of $(8\pi)^{1/3}$ that follows from defining $R_\star$ as the inverse cube root of the bubble number density [199]. In the case of deflagrations the situation is more complicated, as the fluid shells preceding the bubble walls affect the dynamics of neighbouring bubbles, suppressing the bubble nucleation rate and increasing the mean bubble separation [200].

after a time of order $1/m$, where m is the mass scale of the transition [202]. If the transition is strong, the friction might not be strong enough to stop the accelerating bubble walls, which could lead to runaway bubbles that continuously accelerate until the speed of light is reached [203]. This kind of scenario is currently not believed to be plausible in the case of the electroweak phase transition [204].

There exists two kinds of modes for the bubble propagation named after classical combustion physics [205]. The mode where the bubble wall is supersonic ($v_w > c_s$) is called a detonation. In this case, the wall hits a fluid that is at rest in the unbroken phase in front of the wall. Inside the bubble in the broken phase, the fluid at the centre remains at rest, but the fluid around the bubble walls is dragged out by the expanding walls. This means that a discontinuity in the fluid velocity (a shock) forms at the bubble wall, and a less dense region of the fluid follows the wall, forming a decompression wave (also known as a rarefaction wave). In the other case where the bubble wall is subsonic ($v_w < c_s$), known as a deflagration, the fluid inside the bubble is at rest, and the fluid in the front is being pushed back by the expanding wall. This leads to a compression wave forming outside the bubble wall with a preceding shock front. For a tiny range of velocities the bubble wall propagation can also obtain unstable solutions called hybrids that are supersonic deflagrations that manifest as superpositions of the two previously mentioned combustion modes.

The regime in which the bubble wall velocity falls into depends on the strength of the phase transition α and the employed particle physics model. There are two approaches to modelling the friction between the fluid and the expanding bubble wall. The first one is a direct treatment of the microscopic interactions by solving coupled Boltzmann equations, which can be rather tedious. This approach has been utilized, for example, in Ref. [206]. When considering gravitational wave generation, a simpler approach can often be used, where the friction is modelled as a phenomenological parameter, and the bubble evolution is studied as a function of it (see Refs. [202, 207]). These interactions also determine the fraction of the released latent heat that gets converted into the bulk kinetic energy in the fluid, and into gradient energy of the bubble walls. Respectively, these are conventionally modelled by the efficiency factors

$$\kappa_w = \frac{\rho_w}{\rho_{\text{vac}}}, \qquad \kappa_\phi = \frac{\rho_\phi}{\rho_{\text{vac}}}. \tag{2.21}$$

In general, the energy fraction that goes into bulk fluid motions is significant for deflagrations and hybrids, and the fraction that goes to bubble walls is significant for detonations. However, detonations can also lead to significant fluid motions in cases where the bubble walls reach terminal velocity before collision because then most of the remaining energy gets transferred to the fluid. In detonations, the dynamics of the bubbles is also not affected by the walls of the surrounding bubbles since v_w is supersonic so that no signal can precede the bubble fronts. The opposite is true for deflagrations where the compression waves preceding the bubble walls affect other bubbles before collision, which makes the treatment of detonations simpler compared to deflagrations.

2.4 Gravitational waves from first-order phase transitions

First-order phase transitions are violent events that can lead to significant gravitational wave generation. An individual expanding spherical bubble does not source any GWs due to spherical symmetry as shown in Ref. [208]. However, bubble collisions and the resulting induced fluid motions

can lead to multiple distinct GW sources, which will be discussed in more detail later in this section. The three primary sources in question are bubble collisions, turbulence, and sound waves. The total GW power spectrum is then a superposition of these contributions, each of which acts on different time and length scales. In each case the resulting power spectrum depends only on a few key quantities that characterize the phase transition. These are the temperature of the thermal bath when the GWs are generated $T_\star$ (i.e. the temperature at the time of bubble percolation), the time variation of the bubble nucleation rate β that sets the time and length scales of the transition (often given as the dimensionless ratio $\beta/H_\star$), the bubble wall speed v_w, and the parameter α that controls the strength of the transition. All of these quantities can in principle be computed from the underlying cosmological and particle physics models, meaning that the properties of the measured GW power spectrum could be related to the conditions that were present at the time the GWs were generated. However, computations of GWs from FOPTs are still subject to many uncertainties as a result of the rather speculative nature of Standard Model extensions, along with the poor understanding of bubble nucleation, evolution, and the subsequent GW generating processes in realistic thermal environments. Both the phase transition and these processes are also stochastic in nature, which makes analytical handling of them challenging. Therefore, numerical simulations play an essential role in studying and understanding the intricacies of the entire process. A lot of effort is currently being put into improving the theoretical framework around the subject, especially in preparation for the upcoming LISA mission [169, 209].

The aforementioned mentioned key parameters are not independent of each other. For example, strong phase transitions with large α ($\gtrsim O(1)$) have longer durations, leading to lower values for the ratio $\beta/H_\star$. This ratio turns out to be important for the amplitude of the GW signal, as the peak value of the GW power spectrum scales as $\mathcal{P}_{\mathrm{GW}}(f_\star) \propto (H_\star/\beta)^n$ where the value of $n \geq 1$ depends on the individual GW generating process. Therefore, small values of the ratio lead to stronger GW signals. In the physical sense this follows from the fact that in strong transitions more energy gets converted to shear stress energy that sources the gravitational waves. This also has the effect of pushing the characteristic frequency of the GWs towards smaller values, as can be seen from Eqs. (2.1) and (2.2). When considering the energy budget of the transition from the point of view of GW generation, the relevant quantity is the fraction of the latent heat that gets transformed into gradient or kinetic energy, as both of these can act as sources of anisotropic stress. The fraction can be approximated by considering a single bubble and its hydrodynamic equations with the bag equation of state [210], which is an approximation for a relativistic gas that contains two phases with different amount of relativistic degrees of freedom and a bag constant that describes a temperature-independent vacuum energy difference*. Extending the single bubble result to estimate the global kinetic energy fraction then gives [212, 213]

$$K = \frac{\kappa\alpha}{1+\alpha}, \tag{2.22}$$

*The bag model is a simplified model that assumes the speed of sound in both phases to be $c_s = 1/\sqrt{3}$, whereas in reality it is a function of the temperature and therefore depends on the phase, and can deviate from this value during a FOPT [211]. As a result, more refined models have recently been presented, like the one in Ref. [212]. Significant departures in the sound speed from $1/\sqrt{3}$ would also promote it to the fifth key parameter that determines the GW power spectrum.

where κ is the efficiency with which vacuum energy is being converted into kinetic energy (see Eq. (2.21)). Its value depends on the particle contents of the fluid and can in general be written as a function of α, v_w, and the friction. The remaining fraction of the energy $1 - K$ gets converted into thermal energy of the fluid, which does not contribute to GW generation.

Very strong transitions with $\alpha \gg 1$ are associated with a large amount of supercooling. In these kinds of transitions, assuming also low friction, most of the energy gets converted into bubble wall motions with $\kappa_\phi \backsimeq 1$, corresponding to a vacuum phase transition. They also lead to large amount of reheating (a phenomenon where the energy accumulated in the vicinity of the bubble walls gets redistributed into the surrounding fluid, increasing its temperature), because in strong detonations most of the kinetic energy is concentrated around the bubble walls. Therefore, the nucleation temperature T_n can differ from the GW generation temperature $T_\star$ by many orders of magnitude in such transitions. On the other hand, for transitions without significant supercooling and reheating, which is believed to be typical for transitions taking place during the radiation dominated epoch, one can approximate $T_\star \approx T_n$.

For a specific model, the parameters α, β, and T_n are computed from an effective potential that is obtained by a perturbative expansion to one- or two-loop order in four dimensions. However, this approach can result in significant uncertainties in the predicted GW parameter values due to the breakdown of perturbation theory for long-wavelength modes and at high temperatures [214, 215]. The parameter α is obtained directly from the effective potential, and β, T_n are obtained by computing the action of the bounce solution that in turn follows from the Euclidean equations of motion and the effective potential. The bubble wall speed v_w is determined by modelling the friction between the fluid and the bubble wall, like mentioned previously, which is a complicated problem and acts as another source of uncertainty. Next, we will inspect the individual independent GW sources that follow from a FOPT in more detail. Only a general overview will be provided here. For more information about the shape of the GW power spectrum etc. see the references in the sections below.

Bubble collisions

The energy-momentum tensor of the fluid near the bubble walls contains shear stress due to the field-fluid coupling and acts as a source of gravitational waves [213]. Scalar field gradients also lead to non-zero anisotropic stresses, which is the only source of GWs for vacuum transitions. For a single bubble, energy and momentum is distributed in a spherically symmetric way, leading to no net generation of gravitational waves. However, this spherical symmetry is broken in bubble collisions where an envelope of two or more merged bubbles forms. The simplest analytical model in this case is the aptly named envelope approximation [216] that assumes all energy to be contained in a thin region inside the bubble walls, and that only the fluid and the scalar field gradients in the uncollided part of the bubble walls contributes to GW generation, ignoring the complicated overlapping regions inside the bubbles. This kind of assumption is only valid for detonations, which is the combustion mode of interest when it comes to bubble wall collisions, since in deflagrations the GW contribution from them is suppressed. The GW power spectrum is then obtained numerically by considering multiple bubbles whose nucleation follows a Poisson distribution with a width set by the bubble

nucleation rate $\Gamma(t)$. After a statistical averaging over multiple such systems the function for the spectrum follows from fits to the simulation data. The result was first obtained in Ref. [213] and later improved in Ref. [217], giving the peak amplitude of the spectrum as

$$h_0^2 \mathcal{P}_{\mathrm{GW}}(f_\star) = 1.84 \cdot 10^{-6} K_\phi^2 \left(\frac{H_\star}{\beta}\right)^2 \left(\frac{v_w^3}{0.42 + v_w^2}\right) \left(\frac{100}{g_\star}\right)^{1/3} , \tag{2.23}$$

where h_0 follows from the relation $H_0 = 100 h_0\,\mathrm{km/s/Mpc}$, and K_ϕ is the kinetic energy fraction of Eq. (2.22) that only takes into account the kinetic energy that goes to the bubble walls (i.e. with replacement $\kappa \longrightarrow \kappa_\phi$). Because of the nature of the envelope approximation, it misses the contribution to the GW generation that comes from the stirring and displacement of the fluid by the bubbles. This contribution ends up being small for very strong transitions with a lot of supercooling and weak coupling where the bubble walls run away ($v_w \longrightarrow 1$), because only a tiny fraction of the kinetic energy is transferred to the fluid in such cases. They would correspond to vacuum transitions, making bubble collisions the dominant source of GWs. Numerical simulations of vacuum transitions can be found in Refs. [218, 219], and of thermal transitions in the strongly supercooled limit in Ref. Ref. [220]. However, the contribution missed by the envelope approximation is by far the most dominant one for transitions taking place in a thermal fluid where the scalar field is strongly coupled to the fluid so that friction prevents the walls from running away.

Sound waves

Depending on the bubble wall speed v_w, the bubble fronts can contain either rarefaction or compression waves (or both in the case of hybrids) that after collision continue to propagate in the fluid as acoustic waves [221]. These sound waves are a significant source of GWs because they can still be present in the fluid long after the PT has completed, until dissipated away by viscosity, or they steepen into shock waves. Their lifetime can be of the order of the Hubble time, which boosts the GW signal by the ratio $\beta/H_\star$. As a result, considering the typical value of $\beta/H_\star \sim 10^2$, the magnitude of the GW signal from sound waves can be up to two orders of magnitude larger than the one from bubble collisions. Hence, the lifetime of the acoustic phase is an important parameter for the intensity of GWs generated in FOPTs.

GW generation from sound waves has been studied numerically in Refs. [222–225]. They simulate a thermal phase transition with a scalar order parameter coupled to a relativistic fluid and model friction with a phenomenological parameter taking into account both deflagrations and detonations. They confirm the long-lasting nature of sound waves in the fluid after the transition has completed, and find that the vorticity generated in the bubble collisions (contributing to the GWs from turbulence) is subdominant compared to the longitudinal modes (only 1-10%). Recent numerical simulations also imply that sound waves might be more efficient at producing GWs than magnetohydrodynamic turbulence [226]. These findings seem to indicate that sound waves are the main source of GWs from FOPTs for a wide range of models. Recently, the GW power spectrum resulting from FOPTs has also been studied numerically by performing simulations that use various methods to make the computations more economical, like the so-called hybrid simulations in Ref. [227], and Higgless simulations in Refs. [228, 229].

The current leading model for gravitational wave generation from sound waves with the most success in explaining the features seen in numerical simulations is the Sound Shell Model (SSM) [230, 231]. It assumes that after the PT has come to an end, the fluid shells driven by the bubble walls continue to propagate as sound waves. The total velocity field after the phase transition is then modelled as a superposition of sound shells resulting from multiple bubbles, which can be treated as a Gaussian random field. The model gives an expression for the GW power spectrum that can be evaluated from the fluid's velocity power spectrum, which depends on the previously mentioned key parameters. The SSM and its predictions will be discussed in more detail in Chapter 5 where it is used to approximate the GW power spectrum from acoustic turbulence.

Turbulence

The fast moving bubble walls stir the fluid in bubble collisions, leading to the generation of vorticity. A turbulent cascade can develop if the stirring is strong enough, mostly in the case of intermediate and strong transitions. When taking place in a plasma, like in the early universe where the plasma is expected to be fully ionized and highly conductive [232], some of the energy in the vortical modes gets converted into magnetic energy, leading to the development of magnetohydrodynamic (MHD) turbulence [233, 234]. Both the turbulent fluid motions and magnetic fields lead to anisotropic stresses which source GWs. However, this is not the whole story, as in this work we include all non-linear phenomena in the fluid that lead to GW generating perturbations under the label of turbulence. Thus, in addition to the MHD turbulence, non-linearities also arise when the sound waves discussed in the previous section steepen into shocks. They also act as a source of GWs [235], and the kind of random collection of propagating shock waves that follows from the superposition of steepening sound waves after a PT is referred to as acoustic turbulence*.

GW generation from vortical MHD turbulence becomes more significant in the case of deflagrations with high fluid friction where more of the available energy gets converted into rotational fluid motions [225]. Turbulence sets in after one eddy turnover time $t_e = L/\bar{v}_\perp$ where L is the length scale where the fluid kinetic energy initially peaks, corresponding roughly to the mean bubble separation $L \sim R_\star$, and $\bar{v}_\perp$ is the root mean square (rms) velocity of the transverse velocity component. In order for the turbulence to fully develop and decay, providing a long-lasting source, it is required that its timescale is much smaller than that of the expansion, i.e. $t_e \ll H_\star^{-1}$, because otherwise the expansion of the universe would suppress the turbulence, or even prevent it from developing altogether. When all bubbles have collided and the phase transition comes to an end, the turbulent energy injection cuts off and the turbulence decays freely as a result of the viscosity of the fluid. In the early universe this decay is expected to be slow due to the extremely high Reynolds number and small kinematic viscosity of the fluid [236], leading to a long-lasting source with a lifetime that can be several Hubble times. However, in practice, the suppression of the turbulent energy caused by

*Referring to a field of shock waves as a type of turbulence can be confusing as turbulence is conventionally associated with vortical turbulence that consists of chaotic motions and eddies of various sizes, while acoustic turbulence does not share these flow characteristics. Nevertheless, we have still opted to adopt this naming convention that has gained some traction in literature. Ultimately, both are non-linear phenomena that share some common properties that are discussed in section 3.3.

the expansion of the universe and the fact that turbulence decorrelates sets the lifetime effectively at one Hubble time [223]. This amplifies the GW signal by a factor $\beta/H_\star$ like in the case of sound waves. Currently, there are no numerical simulations of phase transitions that are strong enough to reach t_e and display clear turbulent behaviour within reasonable simulation times, so we have to rely solely on analytical predictions and numerical studies with initial conditions that approximately correspond to the state of the fluid after the transition. Many models have been presented over the years (see Refs. [213, 237–242]) which differ in the way they model the decorrelation functions of the GW source to determine its time dependence, the parts of the fluid energy spectrum included in the analysis, and whether the turbulence is taken to be stationary or decaying. They also rely on classical turbulence models, usually that of Kolmogorov turbulence [243], since no relativistic turbulence models exist as of yet. The most recent studies of GW generation from decaying turbulence are found in Refs. [241, 242].

Acoustic turbulence develops on a timescale $t_s = L/\bar{v}_\parallel$ after the sound waves generated by the transition steepen into shocks if $t_s \ll H_\star^{-1}$. Here $\bar{v}_\parallel$ is the rms of the longitudinal velocity component. Shock waves dissipate energy by generating entropy, leading to damping of the waves, and eventually the end of the acoustic phase. Shock collisions can also lead to the generation of vorticity, thereby also contributing to vortical turbulence, although the magnitude of this effect is not yet known. Since acoustic turbulence is the primary focus of this thesis, it is discussed in more detail in Chapter 4, while the GW generation from it is covered in Chapter 5.

3. Hydrodynamics

After a cosmological first-order phase transition taking place during the radiation dominated era has come to an end, the fluid motions in the plasma obey the relativistic hydrodynamical equations of motion that can be obtained from the energy-momentum conservation equations

$$\nabla_\mu T^{\mu\nu} = 0\,, \tag{3.1}$$

assuming that the expansion of the universe can be neglected during the observation interval (i.e. the timescale of the flow must be small compared to the Hubble time $H_\star^{-1}$). In Papers I and III we have studied acoustic turbulence in a cosmological setting by numerical simulations. Instead of carrying out the expensive computations of simulating the entire phase transition, we start with random initial conditions that steepen to form a random field of shocks, corresponding to such that would be present after a first-order phase transition in an approximate sense. This allows us to study the evolution of the fluid over multiple flow timescale units in the non-linear regime. We also ignore the magnetohydrodynamics by assuming all pre-existing magnetic fields to be small. In this chapter we lay out how the fluid equations used in the papers are obtained and the assumptions that have been made along the way. We start by discussing relativistic non-perfect fluids and explain the assumptions we have made to obtain the fluid equations of a radiation fluid in the limit of non-relativistic bulk velocities. At the end of this chapter, we also discuss the general properties of non-linearities and turbulence, and go into more detail about our numerical simulations whose results are discussed in Chapter 4.

3.1 Relativistic non-perfect fluids

In this section we follow the notation and conventions of Ref. [244]. The kinematic properties of the fluid are mainly given by two quantities: the four-velocity $\mathbf{u}$ and the four-acceleration $\mathbf{a}$. The former is defined as

$$u^\mu \equiv \frac{dx^\mu}{d\tau} = u^0(1, \frac{dx^i}{dt}) = \gamma(1, v^i)\,, \tag{3.2}$$

where $x^\mu = (t, x^i)$ is the coordinate vector, τ is the proper time of an observer that is comoving with the fluid, and

$$\gamma = \frac{dt}{d\tau} = \frac{1}{\sqrt{1-v^2}} \tag{3.3}$$

is the Lorentz factor. The four-acceleration is defined as

$$a^\mu \equiv u^\nu \nabla_\nu u^\mu\,, \tag{3.4}$$

and together these two quantities satisfy the normalization and orthogonality conditions

$$\mathbf{u}\cdot\mathbf{u} = u^\mu u_\mu = -1\,, \qquad \mathbf{a}\cdot\mathbf{u} = a^\mu u_\mu = 0\,. \tag{3.5}$$

A covariant derivative of the four-velocity can be decomposed into irreducible tensorial parts as

$$\nabla_\nu u_\mu = \omega_{\mu\nu} + \sigma_{\mu\nu} + \frac{1}{3}\Theta h_{\mu\nu} - a_\mu u_\nu\,, \tag{3.6}$$

where

$$h_{\mu\nu} = g_{\mu\nu} + u_\mu u_\nu \tag{3.7}$$

is a projection tensor that projects any tensor on the hypersurface orthogonal to the four-velocity. It satisfies the identities

$$h_{\mu\nu}u^\mu = 0\,, \qquad h^\lambda_\mu h_{\lambda\nu} = h_{\mu\nu}\,, \qquad h^\mu_\mu = 3\,. \tag{3.8}$$

The quantity $\omega_{\mu\nu}$ is the kinematic vorticity tensor, which is the antisymmetric part of $\nabla_\nu u_\mu$ computed in the space orthogonal to the four-velocity, and can be written as

$$\omega_{\mu\nu} = h^\alpha_\mu h^\beta_\nu \nabla_{[\beta} u_{\alpha]} = \nabla_{[\nu} u_{\mu]} + a_{[\mu} u_{\nu]}\,, \tag{3.9}$$

where the brackets are a shorthand notation in analogue to the antisymmetric part of a tensor

$$T_{[\mu\nu]} = \frac{1}{2!}\left(T_{\mu\nu} - T_{\nu\mu}\right)\,. \tag{3.10}$$

The vorticity tensor describes rigid rotations of a fluid element with respect to the local inertial rest frame. The shear tensor $\sigma_{\mu\nu}$ is the corresponding symmetric part of $\nabla_\nu u_\mu$, which is trace-free and can be expressed in the form

$$\sigma_{\mu\nu} = \nabla_{\langle\mu} u_{\nu\rangle} = \nabla_{(\mu} u_{\nu)} + a_{(\mu} u_{\nu)} - \frac{1}{3}\Theta h_{\mu\nu}\,, \tag{3.11}$$

where the angled brackets are a shorthand for the trace-free, symmetric and spatial part of a tensor

$$T_{\langle\mu\nu\rangle} = h^\alpha_\mu h^\kappa_\nu T_{(\alpha\kappa)} - \frac{1}{3} T_{\alpha\kappa} h^{\alpha\kappa} h_{\mu\nu}\,, \tag{3.12}$$

and the round brackets denote the symmetric part of a tensor

$$T_{(\mu\nu)} = \frac{1}{2!}\left(T_{\mu\nu} + T_{\nu\mu}\right)\,. \tag{3.13}$$

The shear tensor, in turn, describes pure deformations in the fluid, its three eigenvalues being the rates of change in the length of a fluid element along its three primary coordinate directions. These deformations take place in such a way that they maintain the total volume of the fluid element due to the trace-free nature of $\sigma_{\mu\nu}$. Lastly, Θ is the four-divergence of the four-velocity, also called the expansion scalar, which can be written in the form

$$\Theta = h^{\mu\nu}\nabla_\nu u_\mu = \nabla_\mu u^\mu\,. \tag{3.14}$$

It describes changes in the volume of the fluid element that occur while maintaining the shape.

The energy-momentum tensor of the fluid $T^{\mu\nu}$ describes the flux of the μth component of the momentum vector across a surface in the ν-direction. In the case of a perfect fluid, its components have clear physical interpretations in the local rest frame of a comoving observer. The T^{00} component is the total energy density of the fluid

$$e = \rho(1+\epsilon)\,, \tag{3.15}$$

which consists of the rest-mass energy density ρ, and the internal energy density $\rho\epsilon$, with ϵ being the specific internal energy. The components T^{0i} represent energy fluxes in the spatial coordinate directions, while components T^{i0} are the corresponding momentum densities. The spatial diagonal entries T^{ii} all contain the isotropic pressure p in the case of an isotropic perfect fluid. Finally, the off-diagonal elements in the spatial part $T^{ij}_{i\neq j}$ contain the shear stresses. Writing the rest frame tensor in terms of the four-velocity u^μ and generalizing it to any reference frame makes it possible to write the perfect fluid part in the form

$$T^{\mu\nu}_{\mathrm{PF}} = (e+p)u^\mu u^\nu + pg^{\mu\nu}\,. \tag{3.16}$$

Another important conserved quantity describing the fluid is the rest-mass density current $\mathbf{J}$ that gives the flux of rest-mass current density in the μ-direction. In a general reference frame it has the form

$$J^\mu = \rho u^\mu\,, \tag{3.17}$$

and its conservation results in the equation of motion

$$\nabla_\mu J^\mu = 0\,. \tag{3.18}$$

Non-perfect fluids differ from perfect fluids in that they also contain internal interactions in the form of heat conduction, and dissipative processes by viscosity. Such fluids can no longer be described by the assumption of a local thermodynamic equilibrium, and the perfect fluid picture needs to be extended with the addition of dissipative terms and heat fluxes. In these cases the definition of the local rest frame of the fluid becomes ambiguous and the fluid four-velocity can no longer be straightforwardly defined. One way to define the four-velocity $\mathbf{u}$ in a unique and natural way under these circumstances is to employ the so-called Eckart frame [245] (also known as particle frame), where $u^\mu = u^\mu_{\mathrm{N}}$, with u^μ_{N} being a timelike vector that is parallel to the rest-mass current density $\mathbf{J}$. The additional features of non-perfect fluids can be clearly distinguished from those belonging to perfect fluids, making it possible to write the tensors $T^{\mu\nu}$ and J^ν as superpositions of the two contributions*

$$T^{\mu\nu} = T^{\mu\nu}_{\mathrm{PF}} + T^{\mu\nu}_{\mathrm{NPF}} \tag{3.19}$$

$$J^\mu = J^\mu_{\mathrm{PF}} + J^\mu_{\mathrm{NPF}}\,, \tag{3.20}$$

where "NPF" refers to the non-perfect fluid contribution. The choice of frame then imposes constraints on the non-perfect fluid terms, which in the Eckart frame become

$$T^{\mu\nu}_{\mathrm{NPF}}\left(u_\mu\right)_N\left(u_\nu\right)_N = T^{\mu\nu}_{\mathrm{NPF}}u_\mu u_\nu = 0 \tag{3.21}$$

$$J^\mu_{\mathrm{NPF}} = 0\,. \tag{3.22}$$

*We have neglected magnetohydrodynamic effects in this work. Their inclusion would result in extra contributions to the energy-momentum tensor and rest-mass current density in Eqs. (3.19) and (3.20).

The tensor $T^{\mu\nu}_{\text{NPF}}$ can be written in terms of thermodynamic fluxes that are the anisotropic stress tensor $\pi^{\mu\nu}$, the viscous bulk pressure Π, and the heat flux q^μ. They fulfil the properties

$$u_\nu \pi^{\mu\nu} = 0\,, \qquad \pi^\mu_\mu = 0 \tag{3.23}$$

$$q^\mu u_\mu = 0\,, \qquad u_\mu q^\nu \nabla_\nu u^\mu = 0\,. \tag{3.24}$$

The non-perfect fluid part of the energy-momentum tensor can now be divided into individual contributions by these fluxes as

$$T^{\mu\nu}_{\text{NPF}} = T^{\mu\nu}_{\text{shear}} + T^{\mu\nu}_{\text{bulk}} + T^{\mu\nu}_{\text{flux}}\,, \tag{3.25}$$

where

$$T^{\mu\nu}_{\text{shear}} = \pi^{\mu\nu} \tag{3.26}$$

$$T^{\mu\nu}_{\text{bulk}} = \Pi h^{\mu\nu} \tag{3.27}$$

$$T^{\mu\nu}_{\text{flux}} = q^\mu u^\nu + q^\nu u^\mu\,. \tag{3.28}$$

Using Classical Irreversible Thermodynamics (CIT) [246] with Eckart's formulation, which considers first-order deviations from equilibrium, makes it possible to relate the thermodynamic fluxes with their corresponding transport coefficients to linear order. The anisotropic stress tensor then becomes

$$\pi_{\mu\nu} = -2\tilde{\eta}\sigma_{\mu\nu}\,, \tag{3.29}$$

where $\sigma_{\mu\nu}$ is the shear tensor of Eq. (3.11), and the transport coefficient $\tilde{\eta}$ is the dynamic shear viscosity that is a measure of the fluid's ability to resist deformations caused by shear stresses. In a similar fashion, to first order the viscous bulk pressure obtains the form

$$\Pi = -\tilde{\nu}\Theta\,, \tag{3.30}$$

with Θ being the expansion scalar defined in Eq. (3.14), and the dynamic bulk viscosity $\tilde{\nu}$ (also known as the volume viscosity) acts as the transport coefficient. It describes the fluid's ability to resist shearless compression or expansion. The dynamic viscosities are related to the kinematic viscosities, which are also known as momentum diffusivities, through the energy density as

$$\eta = \frac{\tilde{\eta}}{\rho}\,, \qquad \nu = \frac{\tilde{\nu}}{\rho}\,. \tag{3.31}$$

Finally, the heat flux can be written in the form

$$q_\mu = -\kappa T \left(\mathcal{D}_\mu \ln T + a_\mu\right)\,, \tag{3.32}$$

where T is the temperature, $\mathcal{D}_\mu$ is the covariant derivative in the space orthogonal to the four-velocity, defined as

$$\mathcal{D}_\mu f = h^\nu_\mu \nabla_\nu f\,, \tag{3.33}$$

and κ is the transport coefficient related to the heat flux, known as the thermal conductivity. The equations (3.29), (3.30), and (3.32) are called the constitutive equations of CIT, and together with the conservation equations of $T^{\mu\nu}$ in (3.1) and J^μ (3.18), and Eqs. (3.26)–(3.28), they represent a complete

description of relativistic non-perfect fluids in a first-order theory. The equations of motion in Eqs. (3.1) and (3.18) provide five equations for six unknown quantities: the three components of the velocity v_i, the rest-mass energy density ρ, the pressure p, and the specific internal energy ϵ. To close the system of equations, it is necessary to introduce the equation of state that relates the pressure p to other thermodynamic quantities, like ρ or ϵ.

3.2 Limit of non-relativistic bulk velocities

Currently, there are no relativistic models for non-linearities. In fact, phenomena like vortical turbulence are poorly understood even in the case of fully classical Navier-Stokes equations, as will be discussed in more detail in the next section. Simulating relativistic fluids with physical viscosity is also extremely difficult, which is why most studies resort to using so-called artificial viscosity – an ad hoc numerical technique which adds extra viscosity-like terms to the fluid equations to stabilize the simulations. In order to avoid having to use these kinds of arbitrary methods, to simplify the execution of the numerical simulations, and to allow for an easier comparison with the current classical turbulence models, we make the following assumptions:

- The spacetime is assumed to be flat so that the metric reduces to the Minkowski one $g_{\mu\nu} \longrightarrow \eta_{\mu\nu} = \text{diag}(-1, 1, 1, 1)$, and the covariant derivatives can be replaced by the ordinary partial derivatives $\nabla_\mu \longrightarrow \partial_\mu$.

- The particles in the fluid on a microscopic level are taken to be relativistic, but macroscopic collective bulk motions are assumed to take place at non-relativistic velocities so that $|\mathbf{v}| \ll 1$. This kind of scenario is relevant in the case of weak and some intermediate strength FOPTs.

- The heat flux contribution to the energy-momentum tensor $T^{\mu\nu}_{\text{flux}}$ is neglected, as it is expected to be less than $O(v^2)$ in this limit.

- In the above non-relativistic regime the specific internal energy satisfies $\epsilon \ll 1$ and the total energy density is essentially given by the rest-mass energy density $e \approx \rho$, following from Eq. (3.15). This eliminates one of the unknown quantities, and thus the equation for J^μ is no longer needed. The complete fluid equations are now given by

$$\partial_\mu T^{\mu\nu} = 0\,. \tag{3.34}$$

- The equation of state is taken to be the ultrarelativistic one

$$p = c_s^2 \rho \tag{3.35}$$

  as appropriate for a radiation fluid, for which $c_s = 1/\sqrt{3}$. However, we still write the equations explicitly in terms of c_s for generality. This is where our assumptions deviate from a pure Newtonian limit that assumes $p/\rho \ll 1$ instead. This now leaves only four unknown quantities, those being the energy density ρ and the three velocity components v_i that can all be solved from the four equations in Eq. (3.34).

- The kinematic viscosities are assumed to be uniform. This means that the dynamic viscosities can be written as $\tilde{\eta}(\mathbf{x}) = \eta\rho(\mathbf{x})$ and $\tilde{\nu}(\mathbf{x}) = \nu\rho(\mathbf{x})$*.

Under these assumptions, the energy-momentum tensor is then expanded to second order in small quantities, which are taken to be the velocities, their derivatives, and the viscosities. This way in the expanded fluid equations all quantities and terms that have the units of velocity end up being small in comparison to the speed of light. We label the order of magnitude of these first-order small quantities by $O(\varepsilon)$. The square of the Lorentz factor then becomes

$$\gamma^2 = (1 - v^2)^{-1} = 1 + v^2 + O(\varepsilon^4)\,, \tag{3.36}$$

and the perfect fluid part of $T^{\mu\nu}$ is obtained straightforwardly from Eq. (3.16) as

$$T^{00}_{\mathrm{PF}} = \rho + (1 + c_s^2)\rho v^2 + O(\varepsilon^4) \tag{3.37}$$

$$T^{0i}_{\mathrm{PF}} = (1 + c_s^2)\rho v^i + O(\varepsilon^3) \tag{3.38}$$

$$T^{ij}_{\mathrm{PF}} = (1 + c_s^2)\rho v^i v^j + \delta^{ij} c_s^2 \rho + O(\varepsilon^4)\,, \tag{3.39}$$

where the ultrarelativistic equation of state (3.35) has been used to write the pressure p in terms of the energy density ρ. In order to calculate the non-perfect fluid part

$$T^{\mu\nu}_{\mathrm{NPF}} = T^{\mu\nu}_{\mathrm{shear}} + T^{\mu\nu}_{\mathrm{bulk}}\,, \tag{3.40}$$

we need $\Pi h^{\mu\nu}$ and $\pi^{\mu\nu}$ expanded to second order, in accordance with Eqs. (3.26) and (3.27). Starting with the bulk part, Eq. (3.30), and expanding Θ as

$$\Theta = \nabla \cdot \mathbf{v} + O(\varepsilon^2) \tag{3.41}$$

gives

$$\Pi = -\tilde{\nu}\nabla \cdot \mathbf{v} + O(\varepsilon^3)\,, \tag{3.42}$$

where the leading order term is $O(\varepsilon^2)$. This means that in order to obtain $T^{\mu\nu}_{\mathrm{bulk}}$ to second order, only terms where $h^{\mu\nu}$ is of the zeroth order survive. This is only possible for the spatial part of the tensor because $h^{00} = O(\varepsilon^2)$ and $h^{0i} = O(\varepsilon)$. Therefore, one obtains

$$T^{00}_{\mathrm{bulk}} = O(\varepsilon^4) \tag{3.43}$$

$$T^{0i}_{\mathrm{bulk}} = O(\varepsilon^3) \tag{3.44}$$

$$T^{ij}_{\mathrm{bulk}} = -\delta^{ij}\tilde{\nu}\nabla \cdot \mathbf{v} + O(\varepsilon^3)\,. \tag{3.45}$$

Similarly, to obtain $T^{\mu\nu}_{\mathrm{shear}}$ to second order, Eq. (3.29) shows that the shear tensor $\sigma^{\mu\nu}$ is needed to first order. Writing out Eq. (3.11) explicitly while taking into account the assumptions made at the start of this section gives

$$\sigma^{\mu\nu} = \frac{1}{2}\left(\eta^{\alpha\mu}\partial_\alpha u^\nu + \eta^{\alpha\nu}\partial_\alpha u^\mu\right) + \frac{1}{2}u^\alpha \partial_\alpha \left(u^\mu u^\nu\right) - \frac{1}{3}\theta h^{\mu\nu}\,. \tag{3.46}$$

*This assumption is actually not valid for relativistic plasmas in the case of the dynamic shear viscosity, as it should be proportional to $\rho^{3/4}$ instead of being linear. This means that the kinematic shear viscosity cannot be uniform. We have discussed how this affects the fluid equations in Appendix B of Paper III, and verified that this leads to only very small differences in the numerical simulations that are within statistical fluctuations resulting from random initial conditions and temporal averaging.

Expanding this gives $\sigma^{00} = O(\varepsilon^2)$ and $\sigma^{0i} = O(\varepsilon^2)$, where in the latter the only surviving first order contributions end up cancelling each other. The spatial part gives a first order contribution

$$\sigma^{ij} = \frac{1}{2}\left(\partial_i v^j + \partial_j v^i\right) - \frac{1}{3}\delta^{ij}\nabla\cdot\mathbf{v} + O(\varepsilon^2)\,, \tag{3.47}$$

where we now define the traceless rate of shear tensor as

$$S_{ij} = \frac{1}{2}\left(\frac{\partial v_i}{\partial x_j} + \frac{\partial v_j}{\partial x_i} - \frac{2}{3}\delta_{ij}\nabla\cdot\mathbf{v}\right)\,. \tag{3.48}$$

Hence, all in all

$$T^{00}_{\text{shear}} = O(\varepsilon^3) \tag{3.49}$$
$$T^{0i}_{\text{shear}} = O(\varepsilon^3) \tag{3.50}$$
$$T^{ij}_{\text{shear}} = -2\tilde{\eta}S^{ij} + O(\varepsilon^3) \tag{3.51}$$

and

$$T^{00}_{\text{NPF}} = O(\varepsilon^3) \tag{3.52}$$
$$T^{0i}_{\text{NPF}} = O(\varepsilon^3) \tag{3.53}$$
$$T^{ij}_{\text{NPF}} = -2\tilde{\eta}S^{ij} - \delta^{ij}\tilde{\nu}\nabla\cdot\mathbf{v} + O(\varepsilon^3)\,. \tag{3.54}$$

The fluid equations are now given by Eq. (3.34) where the $\nu = 0$ case gives an equation corresponding to the continuity equation, and the equations with $\nu = i$ correspond to the Navier-Stokes equations. Starting with the former, one obtains

$$\partial_\mu T^{\mu 0} = 0 \tag{3.55}$$
$$\Rightarrow \partial_t T^{00}_{\text{PF}} + \partial_i T^{0i}_{\text{PF}} + O(\varepsilon^3) = 0\,, \tag{3.56}$$

so that only the perfect fluid part contributes to second order. Substituting the results in Eqs. (3.37) and (3.38) and rearranging gives

$$\left[1 + (1+c_s^2)v^2\right]\frac{\partial\rho}{\partial t} + (1+c_s^2)\nabla\cdot(\rho\mathbf{v}) + (1+c_s^2)\rho\frac{\partial v^2}{\partial t} + O(\varepsilon^3) = 0\,. \tag{3.57}$$

The equation can now be divided by the prefactor of $\partial_t\rho$, and after using the expansion $\left[1 + (1+c_s^2)v^2\right]^{-1} = 1 - (1+c_s^2)v^2 + O(\varepsilon^4)$, it simplifies to

$$\frac{\partial\rho}{\partial t} + (1+c_s^2)\nabla\cdot(\rho\mathbf{v}) + (1+c_s^2)\rho\frac{\partial v^2}{\partial t} + O(\varepsilon^3) = 0\,. \tag{3.58}$$

In the same way the equations with $\nu = i$ become

$$\partial_\mu T^{\mu i} = 0 \tag{3.59}$$
$$\Rightarrow \partial_t T^{0i}_{\text{PF}} + \partial_j T^{ij}_{\text{PF}} + \partial_j T^{ij}_{\text{NPF}} + O(\varepsilon^3) = 0\,. \tag{3.60}$$

Focusing only on the perfect fluid part by substituting Eqs. (3.38) and (3.39), and leaving the non-perfect fluid part untouched for now gives after some modification

$$\rho\frac{\partial v_i}{\partial t} + v_i\frac{\partial\rho}{\partial t} + \nabla\cdot(\rho v_i\mathbf{v}) + \frac{c_s^2}{1+c_s^2}\nabla_i\rho = -\frac{1}{1+c_s^2}\partial_j T^{ij}_{\text{NPF}} + O(\varepsilon^3)\,. \tag{3.61}$$

The continuity equation (3.58) can be used here to replace the partial time derivative of the energy density to obtain time evolution equations for the velocity only. Keeping only terms up to second order, expanding the third term on the left, and rearranging gives

$$\frac{\partial v_i}{\partial t} + (\mathbf{v}\cdot\nabla)v_i - c_s^2 v_i(\nabla\cdot\mathbf{v}) - c_s^2 v_i(\mathbf{v}\cdot\nabla\ln\rho) + \frac{c_s^2}{1+c_s^2}\nabla_i\ln\rho = -\frac{1}{(1+c_s^2)\rho}\partial_j T^{ij}_{\mathrm{NPF}} + O(\varepsilon^3)\,. \quad (3.62)$$

This equation can now in turn be used to replace the velocity time derivative in the continuity equation so that it becomes a time evolution equation for the energy density only. Since $T^{ij}_{\mathrm{NPF}} = O(\varepsilon^2)$, as evident from Eq. (3.54), only one term is of the second order or smaller and survives after contracting the above equation from the left with v_i, yielding

$$\frac{\partial v^2}{\partial t} = -\frac{2c_s^2}{1+c_s^2}\mathbf{v}\cdot\nabla\ln\rho + O(\varepsilon^3)\,, \quad (3.63)$$

which after substituting to (3.58) gives the continuity equation as

$$\frac{\partial\rho}{\partial t} + (1+c_s^2)\nabla\cdot(\rho\mathbf{v}) - 2c_s^2\mathbf{v}\cdot\nabla\rho + O(\varepsilon^3) = 0\,. \quad (3.64)$$

The only thing left to do now is to calculate the viscosity-dependent non-perfect fluid part on the RHS of (3.62)

$$-\frac{1}{(1+c_s^2)\rho}\partial_j T^{ij}_{\mathrm{NPF}} = -\frac{1}{(1+c_s^2)\rho}\left(\partial_j T^{ij}_{\mathrm{shear}} + \partial_j T^{ij}_{\mathrm{bulk}}\right)\,. \quad (3.65)$$

Starting with the bulk viscosity containing part, one obtains

$$-\frac{1}{(1+c_s^2)\rho}\partial_j T^{ij}_{\mathrm{bulk}} = \frac{1}{(1+c_s^2)\rho}\delta_{ij}\partial_j\left(\tilde{\nu}\nabla\cdot\mathbf{v}\right) \quad (3.66)$$

$$= \frac{\nu}{(1+c_s^2)\rho}\nabla_i(\rho\nabla\cdot\mathbf{v}) \quad (3.67)$$

$$= \frac{\nu}{(1+c_s^2)}\left[\nabla_i(\nabla\cdot\mathbf{v}) + (\nabla\cdot\mathbf{v})\nabla_i\ln\rho\right]\,, \quad (3.68)$$

where on the second line the dynamic bulk viscosity has been written in terms of the kinematic one, which is assumed uniform. Similarly, the shear viscosity terms become

$$-\frac{1}{(1+c_s^2)\rho}\partial_j T^{ij}_{\mathrm{shear}} = \frac{2}{(1+c_s^2)\rho}\partial_j(\tilde{\eta}S_{ij}) \quad (3.69)$$

$$= \frac{2\eta}{(1+c_s^2)}\left(\partial_j S_{ij} + S_{ij}\partial_j\ln\rho\right)\,. \quad (3.70)$$

By using the result

$$\partial_j S_{ij} = \frac{1}{2}\left[\nabla^2 v_i + \frac{1}{3}\nabla_i(\nabla\cdot\mathbf{v})\right]\,, \quad (3.71)$$

it can be written as

$$-\frac{1}{(1+c_s^2)\rho}\partial_j T^{ij}_{\mathrm{shear}} = \frac{\eta}{(1+c_s^2)}\left[\nabla^2\mathbf{v} + \frac{1}{3}\nabla(\nabla\cdot\mathbf{v}) + 2\mathbf{S}\cdot\nabla\ln\rho\right]_i\,, \quad (3.72)$$

where we have used the notation $[\mathbf{S}\cdot\nabla\ln\rho]_i \equiv S_{ij}\partial_j\ln\rho$. All in all, after writing the continuity equation also in terms of the logarithmic energy density, the fluid equations up to second order can be written in the form

$$\frac{\partial\ln\rho}{\partial t} + (1+c_s^2)\nabla\cdot\mathbf{v} + (1-c_s^2)\mathbf{v}\cdot\nabla\ln\rho = 0 \quad (3.73)$$

$$\frac{\partial \mathbf{v}}{\partial t} + (\mathbf{v}\cdot\nabla)\mathbf{v} - c_s^2\mathbf{v}(\nabla\cdot\mathbf{v}) - c_s^2\mathbf{v}(\mathbf{v}\cdot\nabla\ln\rho) + \frac{c_s^2}{1+c_s^2}\nabla\ln\rho = \frac{1}{1+c_s^2}\left[\eta\nabla^2\mathbf{v} + \left(\frac{1}{3}\eta+\nu\right)\nabla(\nabla\cdot\mathbf{v}) + 2\eta\mathbf{S}\cdot\nabla\ln\rho + \nu(\nabla\cdot\mathbf{v})\nabla\ln\rho\right]. \quad (3.74)$$

These reduce to the classical continuity and Navier-Stokes equations in the limit $c_s^2 \to 0$, and $c_s^2/(1+c_s^2) \to c_s^2$ in the pressure gradient term, that corresponds to the Newtonian limit with $p/\rho \ll 1$. Like their classical counterparts, these equations are scale invariant, which is why they describe the behaviour of fluids across various different length scales.

We have conducted numerical hydrodynamical simulations using these fluid equations to study the properties of acoustic turbulence both in 2D (Paper I) and 3D (Paper III). Paper I is missing most of the $\nabla\ln\rho$ containing terms because the derivation in that case treats also the energy density as a first-order small quantity, making these terms of the order $\mathcal{O}(\varepsilon^3)$. However, this is an ill assumption since $\nabla\ln\rho$ can grow significant in the immediate vicinity of shock waves due to the presence of sharp features. The continuity equation also contains a new contribution, the last term in Eq. (3.64), that was also missing in Paper I. It follows from carefully expanding the Lorentz factors in the relativistic fluid equations and including all contributions up to second order. This term has also been missing in other studies using similar fluid equations, like those in Refs. [234, 247, 248]. A study of the 3D case with all these terms properly included is carried out in Paper III.

3.3 Non-linearities

The fluid equations corresponding to the Navier-Stokes equations in (3.74) contain non-linear terms on the left-hand side, meaning that the flows they govern can display non-linear dynamics. These include irregular chaotic motions, eddies, vortices, shock waves, and other flow instabilities. In the limit where the non-linearities are strong, the flows are extremely complex, and they span over a wide range of length and timescales. In fact, turbulence has been historically regarded as one of the greatest unsolved problems in physics*, and even the existence of smooth solutions to the classical Navier-Stokes equations has not been proven and stands as one of the Millenium Prize problems in mathematics [249].

A flow that is smooth and regular is called laminar. In the laminar flow regime viscous forces dominate the inertial forces, preventing motions with lateral mixing and cross currents. The transition from laminar to turbulent flow occurs when the characteristic speed of the flow becomes large enough that the inertial forces become dominant. Therefore, the nature of the flow can be determined by inspecting the ratio of these two forces in the fluid. In the classical case the inertial forces are described by the non-linear term $(\mathbf{v}\cdot\nabla)\mathbf{v}$ that represents the acceleration of the fluid. The viscous forces are dominated by the first two terms on the RHS of (3.74), as the $\nabla\ln\rho$ dependent terms can be regarded to be small on average in comparison. Using the identity

$$\nabla(\nabla\cdot\mathbf{v}) = \nabla^2\mathbf{v} + \nabla\times(\nabla\times\mathbf{v}) \quad (3.75)$$

*This statement is not necessarily true any more nowadays, as turbulence has been studied thoroughly since the 1960s, and as a result we today have many theoretical, observational, and experimental results that have also been confirmed by direct numerical simulations. These results provide at least a partial understanding of the physics of turbulence.

the two terms can be approximately combined into a term of the form $\mu\nabla^2\mathbf{v}$, where μ is the effective viscosity that is a linear combination of the viscosity dependent prefactors in the two terms. The order of the ratio between the inertial and the viscous forces can then be approximated as

$$\frac{|(\mathbf{v}\cdot\nabla)\mathbf{v}|}{|\mu\nabla^2\mathbf{v}|} \sim \frac{\bar{v}^2/L}{\mu\bar{v}/L^2} = \frac{\bar{v}L}{\mu}\,, \tag{3.76}$$

where the velocities have been approximated by the characteristic speed of the flow, the root mean square velocity $\bar{v}$, and the derivatives by $\nabla \sim 1/L$, where L is the typical length scale of the flow. The above quantity is called the Reynolds number

$$\mathrm{Re} \equiv \frac{\bar{v}L}{\mu}\,, \tag{3.77}$$

whose small values ($\mathrm{Re} \ll 1$) correspond to laminar flows, and large values ($\mathrm{Re} \gg 1$) to turbulent ones.

The nature of the non-linearities that emerge depend on how the kinetic energy of the fluid is distributed among the longitudinal and transverse modes, as well as on the fluid's compressibility. When the Reynolds number is high and the transverse modes dominate, the fluid forms vortical (also known as solenoidal) turbulence [250–252] that consists of eddies, swirl-like vortices in the fluid. They are formed at many different length scales so that fully developed turbulence consists of a superposition of eddies of various sizes. Each eddy also carries kinetic energy that depends on its vorticity. The largest eddies are comparable with the geometric length scale of the mean flow, while the smallest eddies are determined by the viscosity and the velocity of the mean flow. This is because at the smallest scales the velocity gradients in the eddies become large enough that kinetic energy gets converted into heat by viscosity effects that counteract the eddying motion. The scale separation between the smallest and the largest eddies is large for fully developed turbulence with a large Reynolds number, which makes the concept of scale a profound feature of turbulence. The large eddies are unstable, so over time they break up into smaller eddies, passing and distributing the kinetic energy among their products. The newly formed eddies eventually break up into even smaller ones and this process goes on until the dissipation scale is reached and the eddies along with their kinetic energy are dissipated away by the viscosity. This leads to a formation of an energy cascade where kinetic energy is transferred from large to small length scales. The strong diffusive and dissipative nature of turbulence follows from this property. A turbulent vorticity field displaying vortical turbulence with eddies in a numerical simulation is plotted in Figure 3.1d.

The study of vortical turbulence and the existing models are based almost solely on incompressible fluids for which $\nabla\cdot\mathbf{v} = 0$. This is a valid approximation only for fluids for which the flow speed is well below the speed of sound, and therefore does not hold in the case of relativistic plasmas. The incompressibility assumption completely excludes the longitudinal regime where waves can be excited and contribute to the dynamics. This regime can give rise to another form of turbulence called wave turbulence [253, 254], which is a general framework containing various types of waves, of which acoustic waves is just one application. Because acoustic waves are the primary focus of this thesis, here we consider the nonlinear contribution associated with them, called acoustic turbulence [255, 256]. It can be defined as a random field of acoustic (sound) waves in which the waves are excited in a wide interval in frequencies and wavelengths. For sufficiently large Reynolds numbers

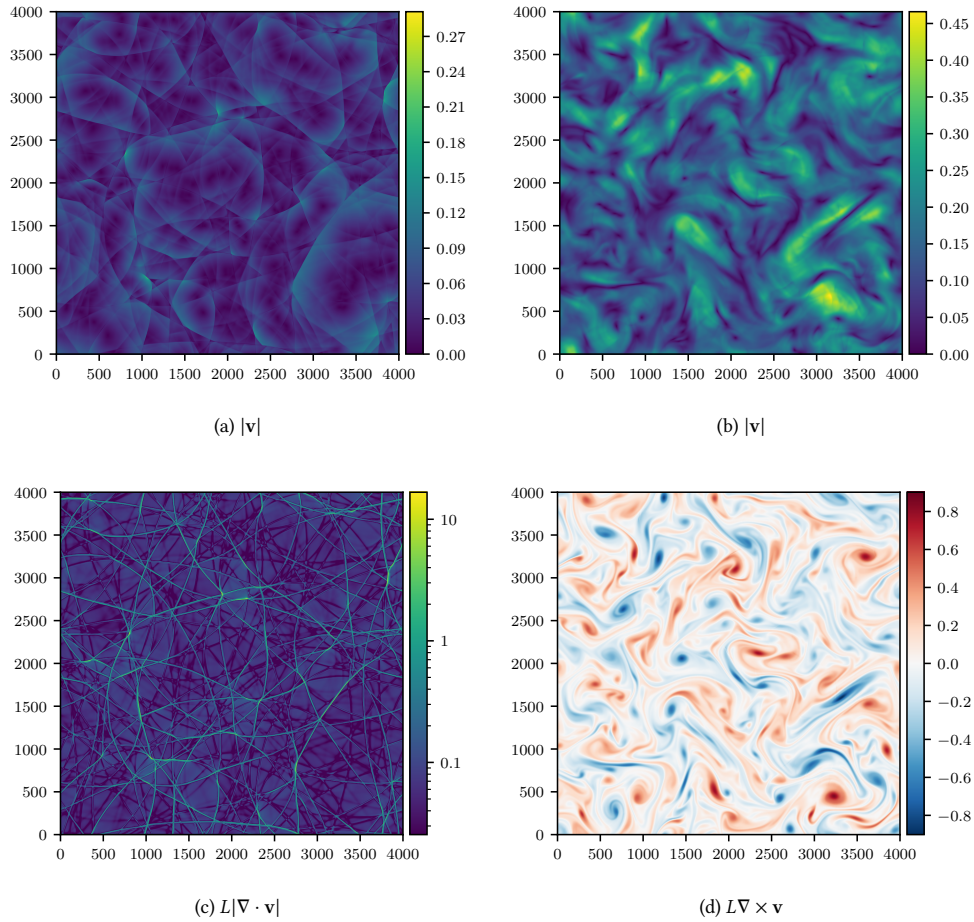

(a) $|\mathbf{v}|$

(b) $|\mathbf{v}|$

(c) $L|\nabla \cdot \mathbf{v}|$

(d) $L\nabla \times \mathbf{v}$

Figure 3.1: The magnitude of the velocity field $v(x, y) = |\mathbf{v}|$ in a 2D simulation in a non-linear regime with Re $\approx$ 230 in the two cases where longitudinal (a), and transverse (b) modes dominate. Figure (c) shows the divergence corresponding to Fig. (a), which highlights the shock waves that are the dominant non-linearities in this case. Likewise, Fig. (d) plots the vorticity (a scalar in 2D) corresponding to Fig. (b). It shows vortical turbulence that consists of eddies of various sizes, and vorticity filaments that stretch between them.

acoustic fields also always develop shock waves [257] that are sharp discontinuity-like features in the flow that propagate faster than the speed of sound in the fluid. Hence, acoustic turbulence is strongly associated with the appearance of shock waves in the flow. This kind of turbulence is also sometimes called compressional or dilatational turbulence. An example of acoustic turbulence is shown in Fig. 3.1c that plots the magnitude of the divergence, highlighting the shock wave fronts in a numerical simulation where the longitudinal modes dominate. In compressible fluids where there is considerable amount of kinetic energy in longitudinal and in transverse modes, both acoustic and vortical turbulence can coexist at the same time. The former also shares many similarities with its vortical counterpart. Acoustic turbulence is associated with strong dissipation as well, similarly to the vortical case, as there is an energy cascade towards the small dissipative length scales that results from wave interactions that excite shorter wavelength modes. It too is characterized by scale separation at high Reynolds numbers, which arises from the property of containing a wide range of waves with different wavelengths. The irregularity of the flows and the sensitivity to initial conditions resulting from the non-linear nature of the fluid equations means that the study of turbulence requires the application of statistical methods. However, this leads to the infamous closure problem of turbulence where the obtained equations contain more unknowns than there are equations, and attempts to derive more equations for the unknowns lead to even more unknowns appearing. Because of this, it is not possible to obtain a total statistical description of turbulence, which holds true also for wave turbulence [253]. Both turbulence types can be analysed using similar techniques, namely spectral methods in Fourier space. It is customary to approximate turbulence to be statistically homogeneous and isotropic in order to allow for analytical treatment, and we adopt these assumptions here as well.

Due to the large number of length scales involved in highly turbulent flows, it is essential for the characterization of turbulence to understand the distribution of kinetic energy across them. To this end, Fourier transforms provide a convenient tool, as in Fourier space each wavenumber corresponds to a certain length scale ($k \sim 1/L$). Therefore, it can be said that the Fourier representation is the natural language of isotropic homogeneous turbulence. We define the spectral density of a statistically isotropic and homogeneous velocity field $P(k)$ as

$$\left\langle v_i(\mathbf{k}) v_i^\star(\mathbf{k}') \right\rangle = (2\pi)^3 \delta(\mathbf{k} - \mathbf{k}') P(k) \,. \tag{3.78}$$

The kinetic energy of the system is proportional to $\left\langle \mathbf{v}^2 \right\rangle$, which after using the inverse Fourier transform for the velocity and proceeding with the calculation in a similar fashion to Eqs. (1.56) – (1.60), using also the definition for the spectral density, gives the result

$$\left\langle \mathbf{v}^2 \right\rangle = \int_0^\infty dk \, \frac{k^2}{2\pi^2} P(k) \equiv \int_0^\infty dk \, E(k) \,, \tag{3.79}$$

where we have defined*

$$E(k) = \frac{k^2}{2\pi^2} P(k) \tag{3.80}$$

*Note that this result depends on the dimensionality! Here we work in 3D, but in Paper I that discusses the 2D case, a different result relation is obtained instead.

as a quantity we call the energy spectrum*, and $E(k)\,dk$ is the contribution that can be related to the kinetic energy that lies on length scales corresponding to the wavenumber interval $[k, k+dk]$. Turbulent flows contain some characteristic length scales that appear as features in the energy spectrum. The aforementioned typical length scale of the flow L is obtained as an expectation value (ensemble average) of the inverse wavenumber $1/k$ using $E(k)/\bar{v}^2$ as a weight function corresponding to the probability density, giving the relation

$$L = \frac{1}{\bar{v}^2}\int_0^\infty \frac{dk}{k} E(k)\,. \tag{3.81}$$

This length scale corresponds to one located near the peak of the energy distribution and therefore characterizes the size of the energy-containing features in the flow. It is the typical length scale of the flow seen earlier in the definition of the Reynolds number in Eq. (3.77). Two other length scales can be obtained on dimensional grounds. On small scales in the dissipative regime the statistics of the flow can be assumed to be uniquely and universally determined by the viscosity and the energy dissipation. The quantity with the units of length that can be constructed from these two quantities is

$$L_K = \left(\frac{\mu^3}{\epsilon}\right)^{1/4}, \tag{3.82}$$

where ϵ is the kinetic energy dissipation rate due to viscosity. It can be obtained from the Navier-Stokes Eq. (3.74) by taking a dot product of the equation with respect to $\mathbf{v}$ from the left, and taking an ensemble average while keeping only the viscosity terms that can give sizable contributions everywhere (i.e. ignoring terms containing $\nabla \ln \rho$ as their averages end up being small under the assumption that the ergodic hypothesis holds for the fluid equations and that the ensemble average can be treated as a volume average instead), yielding†

$$\frac{1}{2}\frac{\partial \left\langle \mathbf{v}^2 \right\rangle}{\partial t} = -\epsilon = \frac{\mu}{1+c_s^2}\left\langle \mathbf{v}\cdot\nabla^2\mathbf{v}\right\rangle\,. \tag{3.83}$$

Using the Fourier inverse transform on the RHS, the viscous dissipation rate ϵ can be written in terms of the energy spectrum as

$$\epsilon = \frac{\mu}{1+c_s^2}\int_0^\infty dk\, k^2 E(k)\,. \tag{3.84}$$

The quantity L_K is known as the Kolmogorov microscale, a name which originates from the study of vortical turbulence, and it characterizes the smallest length scales in the flow where viscous effects are significant. The other quantity with the units of length is

$$L_T = \frac{\bar{v}}{\sqrt{\mathfrak{E}}}\,, \tag{3.85}$$

*Here we have decided not to include the factor $1/2$ into the definition of the kinetic energy spectrum on the LHS of Eq. (3.79), as the fluid equations we are dealing with are not fully classical. The LHS does not therefore correspond to the specific kinetic energy of the system, which with the ultrarelativistic equation of state would be $(1+c_s^2)\bar{v}^2$. We have used the normalization with the $1/2$ factor in Paper I, and switched to this simpler form in Paper III.

†In calculations and when computing values in the numerical simulations, we follow the usual fluid dynamics convention of defining the kinetic energy as $\mathcal{E} = \left\langle \mathbf{v}^2 \right\rangle/2$.

where $\mathfrak{E}$ is the enstrophy

$$\mathfrak{E} = \left\langle \sum_{i,j} |\partial_i v_j|^2 \right\rangle , \tag{3.86}$$

which is a quantity related to the kinetic energy that can be associated with the dissipative effects in the fluid. The length scale L_T is an intermediate length scale in the fluid, $L > L_T > L_K$, below which viscous effects start to become significant. Hence, we have called it the Taylor microscale as an analogue to the quantity used in the study of vortical turbulence. Additionally, the quantity

$$\delta_s = \frac{\mu}{\bar{v}} \tag{3.87}$$

also has units of length, and in the case of longitudinal flows with acoustic turbulence characterizes the width of the shock waves.

According to the Helmholtz decomposition, any differentiable vector field can be written as a sum of divergence- and curl-free vector fields as

$$\mathbf{v} = \mathbf{v}_{\parallel} + \mathbf{v}_{\perp} , \tag{3.88}$$

where

$$\nabla \times \mathbf{v}_{\parallel} = 0 , \qquad \nabla \cdot \mathbf{v}_{\perp} = 0 . \tag{3.89}$$

In the Fourier space their components are given by the transverse projector operator in Eq. (1.35), and the corresponding longitudinal projector as

$$v_i^{\parallel}(\mathbf{k}) = \hat{k}_i \hat{k}_j v_j(\mathbf{k}) \tag{3.90}$$

$$v_i^{\perp}(\mathbf{k}) = (\delta_{ij} - \hat{k}_i \hat{k}_j) v_j(\mathbf{k}) . \tag{3.91}$$

The decomposition can be used in Eq. (3.79), and by utilizing the orthogonality of the longitudinal and transverse components, one obtains on the LHS $\langle \mathbf{v}^2 \rangle = \langle \mathbf{v}_{\parallel}^2 \rangle + \langle \mathbf{v}_{\perp}^2 \rangle$. After defining spectral densities for the longitudinal and transverse velocity fields as

$$\left\langle v_{\parallel,i}(\mathbf{k}) v_{\parallel,i}^{\star}(\mathbf{k}') \right\rangle = (2\pi)^3 \delta(\mathbf{k} - \mathbf{k}') P_{\parallel}(k) \tag{3.92}$$

$$\left\langle v_{\perp,i}(\mathbf{k}) v_{\perp,i}^{\star}(\mathbf{k}') \right\rangle = (2\pi)^3 \delta(\mathbf{k} - \mathbf{k}') P_{\perp}(k) , \tag{3.93}$$

one obtains that the total energy spectrum can be written as

$$E(k) = E_{\parallel}(k) + E_{\perp}(k) \tag{3.94}$$

$$P(k) = P_{\parallel}(k) + P_{\perp}(k) , \tag{3.95}$$

and that the equations (3.79) and (3.80) hold for each of the components $\parallel$ and $\perp$. This decomposition is useful because now the kinetic energy that contributes to acoustic turbulence is contained in $E_{\parallel}$ and the energy that contributes to vortical turbulence is contained in $E_{\perp}$. In the same vein one can define longitudinal and transverse Reynolds numbers

$$\mathrm{Re}_{\parallel} = \frac{\bar{v}_{\parallel} L_{\parallel}}{\mu_{\parallel}} , \qquad \mathrm{Re}_{\perp} = \frac{\bar{v}_{\perp} L_{\perp}}{\mu_{\perp}} , \tag{3.96}$$

where $\mathrm{Re}_\parallel$ and $\mathrm{Re}_\perp$ characterize the strength of acoustic and vortical turbulence respectively. Here $\bar{v}_\parallel = \sqrt{\langle \mathbf{v}_\parallel^2 \rangle}$ and $\bar{v}_\perp = \sqrt{\langle \mathbf{v}_\perp^2 \rangle}$ are the longitudinal and transverse rms velocities, the effective viscosity in the two cases is*

$$\mu_i = \begin{cases} \frac{4}{3}\eta + \nu & i = \parallel \\ \eta & i = \perp \,, \end{cases} \tag{3.97}$$

and the integral length scales associated with the two components of the energy spectrum are

$$L_\parallel = \frac{1}{\bar{v}_\parallel^2} \int_0^\infty \frac{dk}{k} E_\parallel(k) \,, \qquad L_\perp = \frac{1}{\bar{v}_\perp^2} \int_0^\infty \frac{dk}{k} E_\perp(k) \,. \tag{3.98}$$

The Kolmogorov and Taylor microscales of the longitudinal and transverse spectra similarly become

$$L_K^\parallel = \left(\frac{\mu_\parallel^3}{\epsilon_\parallel} \right)^{1/4} , \qquad L_K^\perp = \left(\frac{\mu_\perp^3}{\epsilon_\perp} \right)^{1/4} , \tag{3.99}$$

and

$$L_T^\parallel = \frac{\bar{v}_\parallel}{\sqrt{\mathfrak{E}_\parallel}} \,, \qquad L_T^\perp = \frac{\bar{v}_\perp}{\sqrt{\mathfrak{E}_\perp}} \,, \tag{3.100}$$

where the viscous energy dissipation rates ϵ_i, $i \in \{\parallel, \perp\}$ follow from Eq. (3.84) with replacements $\mu \to \mu_i$ and $E(k) \to E_i(k)$, and the enstrophy in the two cases obtains the form

$$\mathfrak{E}_i = \begin{cases} \left\langle |\nabla \cdot \mathbf{v}|^2 \right\rangle & i = \parallel \\ \left\langle |\nabla \times \mathbf{v}|^2 \right\rangle & i = \perp \,. \end{cases} \tag{3.101}$$

Similarly to the length scales above, one can obtain the timescale of the non-linearities by constructing a quantity with the units of time using the characteristic length scale and velocity of the flow. In the longitudinal case this becomes

$$t_s = \frac{L_\parallel}{\bar{v}_\parallel} \,, \tag{3.102}$$

which, when computed at some initial time before the shocks form, gives the timescale it takes for the sound waves to steepen into shocks, which we call the shock formation time. Correspondingly, in the case of vortical turbulence we have

$$t_e = \frac{L_\perp}{\bar{v}_\perp} \,, \tag{3.103}$$

which is the eddy turnover time of the largest eddies in a turbulent flow.

The energy spectrum of classical turbulence $E(k)$ is a function that is increasing at small wavenumbers, peaks close to $k_p \sim 1/L$, and starts to rapidly fall off in the highly dissipative region at $k > 1/L_K$. When the Reynolds number is large, the integral length scale L and the Taylor microscale

*When considering a situation where $\nabla \times \mathbf{v} = 0$, the dominant two viscosity terms obtain the same form due to Eq. (3.75), and the prefactors can be combined exactly, instead of approximatively like previously. Therefore, in this longitudinal case the inclusion of the bulk viscosity does not alter the behaviour of the fluid apart from modifying to effective viscosity parameter. In the case $\nabla \cdot \mathbf{v} = 0$ the second viscosity term vanishes altogether. We have decided not to include the factor $1/(1 + c_s^2)$ into the effective viscosity (see for example Eq. (3.83)).

L_T are well separated $L \gg L_T$, and the energy spectrum follows a power law form in a wavenumber interval confined by these two length scales

$$E(k) \propto k^{\beta}, \qquad 1/L \ll k \ll 1/L_T\,. \tag{3.104}$$

Because viscous effects only become important for length scales smaller than L_T, inertial effects dominate this power law range, which is why it is called the inertial range. The value of the power law index β is well established for fluids obeying purely classical fluid equations. In the case of vortical turbulence the inertial range behaviour was predicted by Kolmogorov using dimensional analysis, resulting in [243]

$$E_{\perp}(k) \propto k^{-5/3}\,. \tag{3.105}$$

This is known as Kolmogorov's 5/3 law, and it is one of the key results of Kolmogorov's theory for turbulence. Remarkably, even though its derivation is quite simple and is based on various assumptions that might not hold in reality*, it seems to provide a good description of incompressible turbulence and has been observed in many experiments. In the case of compressible flows with acoustic turbulence the presence of shocks induces a characteristic inertial range power law

$$E_{\parallel}(k) \propto k^{-2} \tag{3.106}$$

that was first discovered by Burgers when studying an equation that is today known as Burgers' equation† [258]. The result was later shown to apply also for the classical Navier-Stokes equations in multiple dimensions by Kadomtsev and Petviashvili [257], which is why the power law in Eq. (3.106) is sometimes called the KP spectrum. The general shape for the spectrum described here is universal for both turbulence types in the classical case, meaning that it appears at high enough Reynolds numbers regardless of the initial conditions.

However, the equations we have employed here are not fully classical due to the extra terms that are present, which could potentially alter the inertial range power laws, among other classically established features. Hence, we have studied acoustic turbulence using numerical simulations and compared our results to the classical case in Papers I and III. In the next section we discuss the numerical simulations in more detail.

3.4 Numerical simulations

In Papers I and III, the fluid equations (3.73) and (3.74) have been solved numerically using a Python-based simulation code written by the author of this thesis. The code is public, the older 2D version used in Paper I found in Ref. [259], and the latest 3D version of Paper III found in Ref. [260]. This section provides information about the code, the numerical schemes it takes advantage of, and how the initial conditions are set up in the simulation runs. Here we focus on the latest 3D version of

*These include the turbulence being statistically homogeneous and isotropic at small scales, the behaviour of the fluid at those scales being uniquely determined by the viscosity and the dissipation rate, and statistical self-similarity across the various length scales in the flow.

†The turbulence associated with Burgers' equation is also called Burgers turbulence, which has a rather amusing contraction in the form of "Burgulence" that is sometimes used in the literature.

the code that uses improved higher order numerical schemes and optimization methods compared to the 2D code.

Python is not conventionally the first choice when it comes to high-performance computing because of its interpreted nature. While this property makes Python easy to use because code is compiled on the fly as it is being executed, computational resources are also being wasted on the extra overhead that follows from the interpreter having to read and analyse the code for execution. In computationally heavy tasks such as numerical simulations, this can make the performance of pure Python worse by several orders of magnitude when compared to compiled languages like C or Fortran. Hence, in order to obtain reasonable performance in Python, the most computationally demanding parts of the code need optimization. Luckily, due to its wide and vibrant user base, Python contains multiple tools in this regard in the form of community made packages that can be imported to add functionality or improve the execution of codes. In fact, a properly optimized Python simulation code can obtain near C-like performance.

Python was not originally designed for numerical computing, and most of this base functionality is provided by the NumPy package [261] that adds support for large multidimensional arrays and many operations on them that are implemented as optimized C code. Further speed-ups can be obtained by utilizing Cython [262] that allows for the compilation of Python-like code into C code. This is especially useful in computations containing nested loops, like when computing values for spatial derivatives, as these can be very slow in Python. We have also used the NumExpr [263] package to accelerate the computation of element-wise array operations.

The simulation code we have used has also been parallelized so that the computations that advance the state of the fluid in the simulation can be distributed among multiple processor cores, allowing for simultaneous execution of the code. This is done by assigning slabs of the arrays containing the simulation variables to single processor cores at the start of the simulation, after which setting the initial conditions, all array operations, and the saving of data are done in parallel. The Python package that makes communication between the cores possible is called MPI for Python [264]. Additionally, we have utilized the mpi4py-fft package [265] that contains tools for array distribution among the cores, parallel fast Fourier transforms, and parallel saving of data.

We have also verified the validity of the simulation code by comparing its output and performance against the Pencil Code [266] used in Paper II. The output in time series quantities like the kinetic energy $\mathcal{E}(t)$ is indistinguishable in plots when the initial conditions are correspondingly set between the two codes and the additional term in the continuity equation is disabled. The performance of the Python code is also decent, clocking in at about 20–30% slower than the Pencil Code. The simulation runs featured in Papers I and III have been performed using CSC's (Finnish IT centre for science) supercomputer Puhti. For the 3D simulations featured in Paper III, running with 200 cores, the average time per advance per mesh point is around $2.5 \cdot 10^{-8}$ seconds.

Numerical schemes

In the numerical simulations the fluid is discretized into a cubic mesh* with edge length N, so that the simulations consist of N^3 mesh points and encompass a volume $V = N^3 \Delta x \Delta y \Delta z$. In our simulation code we employ unit spacing so that $\Delta x_i = 1.0$ for all directions. The corresponding mesh in Fourier space, also known as reciprocal lattice, then has the spacing $\Delta k_i = 2\pi / \Delta x_i N$. Because the meshes are centred around the origin, the wavenumbers then span $k \in [-\pi, \pi[$, with the largest wavenumber $k_n = \pi$ corresponding to the Nyquist frequency. In this discrete limit, the integrals become sums over the arrays as

$$\int d^3k \to \frac{(2\pi)^3}{V} \sum_{\vec{k}} . \tag{3.107}$$

The four arrays that are stored and advanced in the simulations are the three components of the velocity v_i and the logarithmic energy density $\ln \rho$. As arrays, their elements can be written as $A[i, j, k] \equiv A_{i,j,k}$, where the indices i, j, k refer to the elements in the x, y, z directions respectively. We also introduce an index with subscript n that denotes points in time. For each of the advanced quantities, the continuity and Navier-Stokes equations (3.73) and (3.74) can be written in the form

$$\frac{dy}{dt} = f(t, y) , \qquad y(t_0) = y_0 , \tag{3.108}$$

where in the case on the continuity equation with $y = \ln \rho$ we have

$$f(\ln \rho) = -(1 + c_s^2) \partial_j v_j - (1 - c_s^2) v_j \partial_j \ln \rho , \tag{3.109}$$

and for the Navier-Stokes with $y = v_i$

$$f(v_i) = -v_j \partial_j v_i + c_s^2 v_i \partial_j v_j + c_s^2 v_i v_j \partial_j \ln \rho - \frac{c_s^2}{1 + c_s^2} \partial_i \ln \rho + \frac{1}{1 + c_s^2} \left[\eta \partial_j \partial_j v_i + \left(\frac{1}{3} \eta + \nu \right) \partial_i \partial_j v_j + 2 \eta S_{ij} \partial_j \ln \rho + \nu \partial_j v_j \partial_i \ln \rho \right] . \tag{3.110}$$

Solving the differential equation requires the use of a numerical scheme. All numerical calculations lead to two kinds of numerical error, the first being the rounding error, which follows from the finite precision of computations with floating-point values, and the second is the truncation error, that is the difference between the exact mathematical solution and the approximate numerical solution. The way the truncation error scales with the step size of the scheme is determined by the order of the scheme. The simplest first-order accurate method is the Euler scheme

$$y_{n+1} = y_n + \Delta t \, f(y_n) \tag{3.111}$$

$$t_{n+1} = t_n + \Delta t , \tag{3.112}$$

where Δt is the step size in time, and $f(y_n)$ is called the increment function. We take it to be time independent because there is no explicit time dependence in Eqs. (3.109) and (3.110). The increment function, as per Eq. (3.108), gives the slope of a tangent line at some point y_n in the

*The code also works with non-cubic grids, like those used in the shock tube runs discussed in section 4.1. For the sake of simplicity, here we focus only on the cubic mesh.

solution curve $y(t)$. Then if Δt is small, the slope has not changed much after a small step at $y(t+\Delta t)$, so y_{n+1} lies close to the actual solution. Consecutively applying the scheme then gives a numerical approximation for $y(t)$. The accuracy of the scheme obviously depends on the time step Δt, and it is called first-order accurate because the local truncation error (error from one iteration) is of the order $O(\Delta t^2)$. The Euler scheme is the simplest so-called Runge-Kutta scheme, which is a family of methods that uses the information on the slope obtained from the differential equation to build a numerical approximation for the solution. In the simulations of Papers I and III, we have used the fourth-order Runge-Kutta scheme (also known as RK4) [267] with a local truncation error of the order $O(\Delta t^5)$. It is widely used in solving ordinary differential equations numerically due to its simplicity, accuracy, and robustness. The accuracy of the scheme compared to the Euler scheme is increased by computing four slopes, one at the start and one at the end of the interval, and two at midpoints between them. The slope used in the advancing is then obtained as a weighted average of the four slopes with more weight given to the midpoints. When formulated, the scheme reads as

$$y_{n+1} = y_n + \frac{\Delta t}{6}(s_1 + 2s_2 + 2s_3 + s_4) \tag{3.113}$$

$$t_{n+1} = t_n + \Delta t\,, \tag{3.114}$$

where the four slopes are given by

$$s_1 = f(y_n) \tag{3.115}$$

$$s_2 = f\left(y_n + \Delta t\,\frac{k_1}{2}\right) \tag{3.116}$$

$$s_3 = f\left(y_n + \Delta t\,\frac{k_2}{2}\right) \tag{3.117}$$

$$s_4 = f(y_n + \Delta t\, k_3)\,. \tag{3.118}$$

The convergence of the numerical solution is described by the Courant-Friedrichs-Lewy condition [268]. In computational fluid dynamics it is characterized by the dimensionless Courant number C that indicates the propagation speed of information, given by the flow velocity u, in comparison to the velocity it takes to move between grid points in a unit of time $\Delta x/\Delta t$. If the former is larger than the latter, information propagates through more than one mesh point in each time step, leading to inaccurate solutions or diverging behaviour. The stability condition then becomes

$$C = \frac{u\Delta t}{\Delta x} \leq C_{\max}\,, \tag{3.119}$$

where the exact value of $C_{\max}$ depends on the scheme used, being close to unity for explicit schemes like the RK4. In order to make sure that the stability condition is always fulfilled, we have used an adaptive timestep of the form

$$\Delta t = \frac{C\Delta x}{u}\,, \qquad u = \frac{c_s + |\mathbf{v}|_{\max}}{1 + c_s|\mathbf{v}|_{\max}}\,, \tag{3.120}$$

where for the flow velocity u we have used the velocity-addition formula of special relativity between the sound speed c_s and the maximum velocity in the flow to ensure that u does not exceed

Derivative	Order	-3	-2	-1	0	1	2	3
1st	2	0	0	-1/2	0	1/2	0	0
	4	0	1/12	-2/3	0	2/3	-1/12	0
	6	-1/60	3/20	-3/4	0	3/4	-3/20	1/60
2nd	2	0	0	1	-2	1	0	0
	4	0	-1/12	4/3	-5/2	4/3	-1/12	0
	6	1/90	-3/20	3/2	-49/18	3/2	-3/20	1/90

Table 3.1: Coefficients for the 2nd, 4th, and 6th order central finite difference schemes used in approximating first and second derivatives with uniform grid spacing. The numbers on the top row are the displacements from the evaluation point along the direction specified by the derivative. The full scheme is a sum of terms with these displacements where each term is accompanied by the listed coefficient.

the speed of light. In paper III we have used a value of $C = 0.5$, which gives a converging solution with good accuracy and performance (In Paper I, a small enough fixed time step was used instead).

Computation of the increments in Eqs. (3.109) and (3.110) requires numerical approximation of spatial derivatives on the simulation mesh. Various schemes can be derived by combining Taylor series approximations of the differentiable function at various points until its derivative has the desired degree of accuracy. In the papers, we have used a central finite difference scheme of the second order accuracy in Paper I, and of the sixth order in Paper III. The algorithm behind the derivation of the scheme is explained in Ref. [269], and the resulting coefficients for the central difference scheme for the first and second derivatives at the different orders implemented in the simulation code are found in Table 3.1. For example, for a general array A, in the case of the sixth order scheme the x-derivative would read as

$$\partial_x A_{i,j,k} \approx (-A_{i-3,j,k} + 9A_{i-2,j,k} - 45A_{i-1,j,k} + 45A_{i+1,j,k} - 9A_{i+2,j,k} + A_{i+3,j,k})/(60\Delta x)\,, \tag{3.121}$$

and the corresponding second derivative as

$$\partial_x^2 A_{i,j,k} \approx (2A_{i-3,j,k} - 27A_{i-2,j,k} + 270A_{i-1,j,k} - 490A_{i,j,k} + 270A_{i+1,j,k} - 27A_{i+2,j,k} + 2A_{i+3,j,k})/(180\Delta x^2)\,. \tag{3.122}$$

Cross derivatives of the type $\partial^2/\partial x_i \partial x_j$ can be evaluated numerically by applying the first derivative scheme twice recursively, but this is computationally less efficient than deriving and implementing a separate scheme for them. These schemes can be obtained in a straightforward, albeit a bit tedious way, by analytically applying the first derivative scheme to $\partial_l A_{i,j,k}$. For example, for the sixth order scheme, the coefficients are shown in Table 3.2. Instead of using the full scheme, which contains 36 terms in total, we have in Paper III used a so-called bidiagonal scheme found in Ref. [248], shown in Table 3.3. It is an approximative scheme for the cross derivatives that only includes terms on the diagonals in the table, leading to a total of only 12 terms, and therefore a faster evaluation in comparison to the full scheme. Evaluation of a derivative at a certain point requires information from the adjacent points that are a distance of half times the order of the scheme away from the

	-3	-2	-1	0	1	2	3
-3	-1	9	-45	0	45	-9	1
-2	9	-81	405	0	-405	81	-9
-1	-45	405	-2025	0	2025	-405	45
0	0	0	0	0	0	0	0
1	45	-405	2025	0	-2025	405	-45
2	-9	81	-405	0	405	-81	9
3	1	-9	45	0	-45	9	-1

Table 3.2: Coefficients for the mixed derivative $\partial^2/\partial x_i \partial x_j$ in the case of the sixth order central finite difference scheme, obtained by applying the corresponding first derivative scheme of Table 3.1 twice. The numbers on the top row are the displacements from the evaluation point along the x_i direction, and the numbers in the first column are displacements along the x_j direction. All values listed in the table are to be divided by $3600\Delta x_i \Delta x_j$.

	-3	-2	-1	0	1	2	3
-3	-2	0	0	0	0	0	2
-2	0	27	0	0	0	-27	0
-1	0	0	-270	0	270	0	0
0	0	0	0	0	0	0	0
1	0	0	270	0	-270	0	0
2	0	-27	0	0	0	27	0
3	2	0	0	0	0	0	-2

Table 3.3: Coefficients for the mixed derivative with the bidiagonal scheme of Ref. [248]. This scheme has been used in the simulations of Paper III. All values listed in the table are to be divided by $720\Delta x_i \Delta x_j$.

point itself. This means that in order to calculate derivatives at the edge of the simulation mesh, boundary conditions need to be specified. We have opted for periodic boundary conditions, so that $A[N+i,l,k] = A[i,l,k]$, and similarly for also the x and y directions, when calculating the derivatives. The consequence of this boundary condition choice is that if some feature in the flow propagates through the edge of the mesh, it will re-emerge on the opposite side with the same shape and velocity. An additional complication to the evaluation of the spatial derivatives using these schemes is introduced when the code is run in parallel. Because the simulation mesh is distributed among many processes, evaluation of the derivatives at the edges of each process's submesh needs information from processes that possess the adjacent submeshes. In practice this is done by adding new elements to the arrays on the boundaries of the submeshes, called ghost zones, that are then communicated the proper values from adjacent processes. For example, the sixth order scheme requires 6 ghost zone elements on each direction, 3 on each side of the mesh. This is one of the factors that lead to diminishing returns when increasing the core count, as high number of cores means a large number of ghost zones, which leads to extra workload in the form of communicating values between the processes. Additionally, one of the drawbacks of using high order central difference schemes is that at high Reynolds numbers they can lead to the appearance of spatial oscillations at the crest of the waves. These numerical artefacts are also sometimes called "wiggles", and their appearance limits the range of viscosity values that can be used in the simulations*.

While the time advancement in the simulations is performed in real space, the arrays for the velocity components v_i are occasionally Fourier transformed numerically using a fast Fourier transform algorithm when data is saved. Assuming that the ergodic hypothesis holds, one can repeat the calculation to obtain Eq. (3.79), this time regarding the ensemble average as a volume average of the type

$$\langle A \rangle = \frac{1}{V} \int_V A \, d^3x \,. \tag{3.123}$$

The average then instead hits the exponential function $e^{i\mathbf{x}\cdot(\mathbf{k}+\mathbf{k}')}$, that by Eq. (5) becomes the delta function. Then comparing the end result to Eq. (3.80) gives

$$P(k) = \frac{1}{V} \sum_i |v_i(\mathbf{k})|^2 \,, \tag{3.124}$$

where the index i runs over the number of dimensions D. When computed numerically from the simulation data using the Fourier transformed velocity component arrays, $P(k)$ also becomes an array with N^D elements. Quantities like the kinetic energy resulting from Eq. (3.79), and the integral length scale in Eq. (3.81) can then be computed in Fourier space using the spectral density array with Eq. (3.80) and the discrete limit of Eq. (3.107). The spectrum data that is saved in the simulations is a 1D array of length $N/2-1$ that is created by radially averaging the full 3D spectrum array over spherical shells of width Δk up to the Nyquist frequency k_n. This means that the corners of the cubic array are not included in the averaging, and the nth element of the resulting array corresponds to the wavenumber $2\pi n/N\Delta x$.

*Other factors limiting the range of obtainable Reynolds numbers in the simulations are the box size that sets a bound for the initial peak wavenumber $k_p \sim 1/L$, and the approximation of the non-relativistic bulk velocities used to derive the fluid equations, which sets a bound for the allowed rms-velocities.

Initial conditions

The initial conditions are given in terms of the longitudinal and transverse spectral densities, defined as

$$P_{\parallel}(|\mathbf{k}|) = \frac{1}{V}\left(|v_x^{\parallel}(\mathbf{k})|^2 + |v_y^{\parallel}(\mathbf{k})|^2 + |v_z^{\parallel}(\mathbf{k})|^2\right) \tag{3.125}$$

$$P_{\perp}(|\mathbf{k}|) = \frac{1}{V}\left(|v_x^{\perp}(\mathbf{k})|^2 + |v_y^{\perp}(\mathbf{k})|^2 + |v_z^{\perp}(\mathbf{k})|^2\right), \tag{3.126}$$

where each spectral density component is a broken power law with an exponential suppression of the form

$$P(k) = A\frac{(k/k_p)^{\xi}}{\left[1+(k/k_p)^{\alpha/\delta}\right]^{\delta}} e^{-(k/k_d)^2}. \tag{3.127}$$

The values of ξ and α control the steepness of the two power laws, δ controls the shape of the peak, and k_d sets the wavenumber at which the exponential suppression becomes significant, cutting off the power law behaviour. The initial values for the parameters in the equation for each of the featured runs have been listed in Table IV for Paper I, and in Table IX for Paper III. The longitudinal and transverse velocity components in Eqs. (3.125) and (3.126) are related to the Cartesian velocity components $v_i(\mathbf{k})$ by the projector operators in Eqs. (3.90) and (3.91). The velocity components in Fourier space can also be written in an orthogonal basis as

$$v(\mathbf{k}) = v^{\parallel}(\mathbf{k})\hat{\mathbf{k}} + v_{t_1}(\mathbf{k})\hat{\mathbf{e}}_1(\mathbf{k}) + v_{t_2}(\mathbf{k})\hat{\mathbf{e}}_2(\mathbf{k}), \tag{3.128}$$

where the unit vectors $\hat{\mathbf{e}}_1$ and $\hat{\mathbf{e}}_2$ are

$$\hat{\mathbf{e}}_1(\mathbf{k}) = \hat{\mathbf{q}} \times \hat{\mathbf{k}}, \qquad \hat{\mathbf{e}}_2(\mathbf{k}) = \hat{\mathbf{k}} \times \hat{\mathbf{e}}_1(\mathbf{k}). \tag{3.129}$$

The transverse component consists of two vectors perpendicular to the unit vector $\hat{\mathbf{k}}$. The direction of the components, controlled by the vector $\hat{\mathbf{q}}$, and how the transverse power in $P_{\perp}(k)$ is distributed to the two transverse velocity components v_{t_1} and v_{t_2} can be chosen freely to generate, for example, helical velocity fields. Because here we only consider purely longitudinal initial conditions that form shocks and acoustic turbulence, we have $P_{\perp}(k) = 0$, and we have chosen the direction of $\hat{\mathbf{q}}$ so that there is no anisotropy in the rms velocity for the Cartesian components v_i in real space.

The real space velocity components $v_i(\mathbf{x})$ advanced in the simulations are obtained from the initial spectral density in Eq. (3.127) as follows. First, the longitudinal and transverse spectral densities are transformed into 3D arrays using the 3D component arrays k_i with $k = \sqrt{\sum_i k_i^2}$. Using the fact that a random field generated from three components will have longitudinal and transverse rms velocities in the proportion 1:2 makes it possible to find the real parts of the velocity components $v^{\parallel}(\mathbf{k})$, $v_{t_1}(\mathbf{k})$, and $v_{t_2}(\mathbf{k})$ by scaling the initial spectral densities (one would also need to decide here the distribution of $P_{\perp}(k)$ on the two transverse components). The imaginary part of these components is filled with random phases φ as

$$v_i(\mathbf{k}) = v_i(\mathbf{k})e^{i\varphi}, \tag{3.130}$$

where $\varphi \in [-\pi, \pi[$ in such a way that $v_i(-\mathbf{k}) = v_i^{\star}(\mathbf{k})$, giving a real valued velocity array in real space. This leads to random initial conditions in real space that also automatically fulfil the periodic boundary conditions. Equations (3.125) and (3.126) with Eq. (3.128) and the projectors can be

solved for the Cartesian Fourier space components $v_i(\mathbf{k})$, and can then be computed in terms of the aforementioned three Fourier space components and the unit vectors $\hat{k}_i$, that we on the mesh write as

$$\hat{k}_i = \frac{\sin\left(k_i \Delta x_i\right)}{\sqrt{\sum_i \sin^2\left(k_i \Delta x_i\right)}}, \tag{3.131}$$

which results from using the eigenvalues of the derivative operator. The real space velocity components are then finally obtained by inverse fast Fourier transforming the arrays $v_i(\mathbf{k})$. The initial energy density ρ in the simulations is taken to be uniform in Paper III, and initialized from a spectral density similarly to the velocity in Paper I.

The dataset in the 2D simulations of Paper I consists of 11 runs with 10080^2 resolution, and in the 3D simulations of Paper III of 15 runs that have resolutions of 1000^3. The runs have differing initial conditions with Reynolds numbers ranging between 10-225 for Paper I and 10-192 for Paper III, with the highest initial rms velocities around 0.22, fulfilling the requirement of the non-relativistic bulk velocity approximation used in deriving the fluid equations. The flows have been simulated for 60 shock formation times in the case of Paper I and 20 shock formation times in Paper III, which is long enough to extract information on the decay characteristics. More information on the runs and their initial flow characteristics can be found in Table IV of Paper I and Table IX of Paper III.

4. Acoustic turbulence

In Papers I and III, we have studied decaying acoustic turbulence arising from the fluid equations (3.73) and (3.74) using the numerical simulations described in the previous section. This chapter provides a summary of both the numerical and analytical results obtained in the two papers.

4.1 Shock waves

The shape of an individual shock wave can be solved analytically directly from the fluid equations in the limit where the fluid velocity is much less than the shock propagation speed. There is a difference between the results obtained in Papers I and III because in the case of the latter new terms were introduced that were missing in the earlier analysis. Here we follow the complete description with all the terms included. To start with, in the simplest non-trivial case one can consider the solutions to these equations to be right-moving wave profiles propagating along some fixed direction. Taking this direction to be along the x-axis, the solutions can be written as

$$\ln \rho(\mathbf{x}, t) = L(k_s(x - u_s t)) \,, \qquad \mathbf{v}(\mathbf{x}, t) = V(k_s(x - u_s t))\hat{\mathbf{e}}_x \,, \tag{4.1}$$

where $\hat{\mathbf{e}}_x$ is a unit vector along the x-axis, u_s is the velocity at which the wave (shock) profile propagates, and k_s is a quantity that controls its steepness. The fluid equations were expanded in the low velocity limit, so we have $V \ll 1$, and the limit mentioned at the start of this section implies $V \ll u_s$. The ansatzes can then be substituted into the fluid equations to obtain differential equations for V and L. It is convenient to define the argument of these functions as $y = k_s(x - u_s t)$, after which the continuity equation (3.73) becomes

$$\frac{dL(y)}{dy}\frac{\partial y}{\partial t} + (1 + c_s^2)\frac{dV(y)}{dy}\frac{\partial y}{\partial x} + (1 - c_s^2)V(y)\frac{dL(y)}{dy}\frac{\partial y}{\partial x} = 0 \,. \tag{4.2}$$

Now because

$$\frac{\partial y}{\partial t} = -u_s k_s \,, \qquad \frac{\partial y}{\partial x} = k_s \,, \tag{4.3}$$

after factoring one obtains

$$\left[u_s - (1 - c_s^2)V(y)\right]\frac{dL(y)}{dy} = (1 + c_s^2)\frac{dV(y)}{dy} \,. \tag{4.4}$$

Like in the previous chapter when deriving the fluid equations, we expand the equations to second order in small quantities. This way one finds

$$\frac{dL(y)}{dy} = \frac{1+c_s^2}{u_s\left[1-(1-c_s^2)\frac{V(y)}{u_s}\right]}\frac{dV(y)}{dy} \tag{4.5}$$

$$= \frac{1+c_s^2}{u_s}\left[1+(1-c_s^2)\frac{V(y)}{u_s}\right]\frac{dV(y)}{dy} + O(\epsilon^3)\,, \tag{4.6}$$

where the denominator has been expanded for $V/u_s \ll 1$. The process can now be repeated for the Navier-Stokes equation (3.74). However, from Eq. (4.6) we can see that dL/dy is a first-order small quantity as it is proportional to the derivative of $V(y)$ at its lowest order. This renders the $\nabla \ln \rho$ dependent viscosity terms to be of the third order along with the velocity containing $\nabla \ln \rho$ term on the LHS of the equation. After dropping these terms, the result can be written as

$$\left[(1-c_s^2)V(y)-u_s\right]\frac{dV(y)}{dy} + \frac{c_s^2}{1+c_s^2}\frac{dL(y)}{dy} = \frac{\mu k_s}{1+c_s^2}\frac{d^2V(y)}{dy^2} + O(\varepsilon^3)\,, \tag{4.7}$$

where $\mu = 4/3\eta + \nu$ is the effective viscosity. Eq. (4.6) can now be used here to obtain a differential equation for the velocity profile $V(y)$ only. The resulting equation can be simplified to

$$\frac{d^2V(y)}{dy^2} + \frac{1}{\mu k_s}\left[a + bV(y)\right]\frac{dV(y)}{dy} = 0\,, \tag{4.8}$$

where we have defined the coefficients a and b as

$$a = u_s(1+c_s^2)\left(1-\frac{c_s^2}{u_s^2}\right) \tag{4.9}$$

$$b = (c_s^4-1)\left(1+\frac{c_s^2}{u_s^2}\right)\,. \tag{4.10}$$

Solving this differential equation naturally requires specifying the boundary conditions. We take them to be

$$V(+\infty) = V_+ \tag{4.11}$$

$$V(-\infty) = V_- \tag{4.12}$$

$$\left.\frac{dV(y)}{dy}\right|_{y=\pm\infty} = 0 \tag{4.13}$$

that correspond to a velocity profile that approaches a constant value of V_+ on the right-hand side, and a constant value of V_- on the left-hand side, and for the wave to be right-moving, we require $V_- > V_+$. Eq. (4.8) can be readily integrated, yielding

$$\frac{dV(y)}{dy} + \frac{1}{\mu k_s}\left[aV(y) + \frac{b}{2}V^2(y)\right] = C\,, \tag{4.14}$$

with C being an integration constant. Applying the boundary conditions, it can be expressed in terms of V_- and V_+ as

$$C = \frac{1}{\mu k_s}\left(aV_- + \frac{b}{2}V_-^2\right) = \frac{1}{\mu k_s}\left(aV_+ + \frac{b}{2}V_+^2\right)\,, \tag{4.15}$$

which also gives an equation for the shock velocity u_s when a and b are replaced using Eqs. (4.9) and (4.10), resulting in

$$u_s^3 - c_s^2 u_s + \frac{1}{2}(c_s^2 - 1)(u_s^2 + c_s^2)(V_- + V_+) = 0\,. \tag{4.16}$$

Continuing the solution, the differential equation (4.14) can be separated to yield

$$\int dy = \int \frac{dV}{C - \tilde{a}V - \frac{\tilde{b}}{2}V^2}\,, \tag{4.17}$$

where to simplify the notation we have absorbed the factor $1/\mu k_s$ into the factors $\tilde{a} = a/\mu k_s$ and $\tilde{b} = a/\mu k_s$. Because the shocks move faster than the speed of sound in the medium, i.e. $u_s > c_s$, we also have that $\tilde{a} > 0$ and $\tilde{b} < 0$. Using the roots of the quadratic equation in the denominator, the equation becomes

$$\int dy = -\frac{2}{\tilde{b}} \int \frac{dV}{\left(V + \frac{\tilde{a}}{\tilde{b}} + \frac{\sqrt{\tilde{a}^2 + 2\tilde{b}C}}{\tilde{b}}\right)\left(V + \frac{\tilde{a}}{\tilde{b}} - \frac{\sqrt{\tilde{a}^2 + 2\tilde{b}C}}{\tilde{b}}\right)} \tag{4.18}$$

$$= -\frac{2\tilde{b}}{\tilde{a}^2 + 2\tilde{b}C} \int \frac{dX}{\frac{\tilde{b}^2 X^2}{\tilde{a}^2 + 2\tilde{b}C} - 1} \tag{4.19}$$

$$= \frac{2}{\sqrt{\tilde{a}^2 + 2\tilde{b}C}} \int \frac{dZ}{1 - Z^2}\,, \tag{4.20}$$

where a change of variables $X = V + \tilde{a}/\tilde{b}$ has been performed when moving from the first line to the second line, and another one with $Z = \tilde{b}X/\sqrt{\tilde{a}^2 + 2\tilde{b}C}$ when moving from the second line to the third. The integral is now elementary, which after integrating and substituting Z and X gives

$$y = \frac{2}{\sqrt{\tilde{a}^2 + 2\tilde{b}C}} \tanh^{-1}\left[\frac{\tilde{b}}{\sqrt{\tilde{a}^2 + 2\tilde{b}C}}\left(V + \frac{\tilde{a}}{\tilde{b}}\right)\right] + D'\,, \tag{4.21}$$

with D' being the integration constant. After solving for V and writing the result in terms of a and b, one obtains

$$V(y) = \frac{\sqrt{a^2 + 2bC_s}}{b} \tanh\left(\frac{\sqrt{a^2 + 2bC_s}}{2\mu k_s} y + D\right) - \frac{a}{b}\,, \tag{4.22}$$

where we have defined

$$C_s = \mu k_s C = aV_- + \frac{b}{2}V_-^2 = aV_+ + \frac{b}{2}V_+^2\,. \tag{4.23}$$

The integration constant D sets the initial position of the wave on the x-axis. Therefore, after substituting y, the velocity $V(x,t)$ has a profile that is determined by a hyperbolic tangent as

$$V(x,t) = \frac{\sqrt{a^2 + 2bC_s}}{b} \tanh\left[k_s(x - u_s t - x_0)\right] - \frac{a}{b}\,, \tag{4.24}$$

where x_0 is the initial position, and we have identified

$$k_s = \frac{\sqrt{a^2 + 2bC_s}}{2\mu}\,. \tag{4.25}$$

All viscosity dependence lies in this factor that controls the steepness of the wave, being an inverse of the shock width $\delta_s \sim 1/k_s$. Hence, small values of the viscosity lead to narrow and steep shocks and vice versa.

The continuity equation can be used to find the relation between the energy density and velocity profiles. Integrating Eq. (4.5) gives

$$L(y) = -\frac{1+c_s^2}{1-c_s^2}\ln\left[1-\frac{1-c_s^2}{u_s}V(y)\right] + C' \tag{4.26}$$

that after using the definition of L in Eq. (4.1) and the initial condition $\rho = \langle\rho\rangle \equiv \rho_0$ when $V = 0$ gives

$$\rho(x,t) = \frac{\rho_0}{\left[1-\frac{1-c_s^2}{u_s}V(x,t)\right]^{\frac{1+c_s^2}{1-c_s^2}}}. \tag{4.27}$$

The energy density can be written as a superposition of the conserved mean value ρ_0 and a perturbation around it as $\rho(x,t) = \rho_0 + \delta\rho(x,t)$. Defining a fractional density perturbation as $\widetilde{\delta\rho} = \delta\rho/\rho_0$ gives

$$\widetilde{\delta\rho}(x,t) = \frac{1}{\left[1-\frac{1-c_s^2}{u_s}V(x,t)\right]^{\frac{1+c_s^2}{1-c_s^2}}} - 1 \tag{4.28}$$

$$\Rightarrow \widetilde{\delta\rho}(x,t) \backsimeq \frac{1+c_s^2}{u_s}V(x,t) \tag{4.29}$$

to first order in the limit $V/u_s \ll 1$. This result can be used to replace the velocity values V_+ and V_- by the corresponding (fractional) energy density values $\widetilde{\delta\rho}_+$ and $\widetilde{\delta\rho}_-$ in the shock speed equation (4.16). This has the benefit of transforming the equation from a cubic to a quadratic one, making it possible to obtain a simple approximate analytical result for u_s. Solving for the shock velocity then gives the result

$$u_s \approx c_s\sqrt{\frac{2(1+c_s^2)+(1-c_s^2)(\widetilde{\delta\rho}_+ + \widetilde{\delta\rho}_-)}{2(1+c_s^2)-(1-c_s^2)(\widetilde{\delta\rho}_+ + \widetilde{\delta\rho}_-)}}, \tag{4.30}$$

that clearly displays the property of shocks propagating faster than the speed of sound, and that an asymptotically weak shock wave (small values of $\widetilde{\delta\rho}_+ + \widetilde{\delta\rho}_-$) tends to a sound wave.

In order to study the validity of these results, we have conducted numerical simulations on a narrow grid that essentially corresponds to a one-dimensional situation. In these so-called shock tube runs the initial conditions are taken to be a rectangular-like wave in the energy density that has steep tanh-profiles on the sides. As the simulation is advanced, this wave breaks into a left- and a right-moving shock wave. We have compared the profile seen in the simulations to the one obtained analytically, and we find very good agreement between them in Paper I (Fig. 16) and an excellent match in Paper III (Fig. 7). Shock speeds obtained by observing the propagation of a single point in the waveform in the shock tube simulations are also found to be within 1% of the values obtained numerically from Eq. (4.16).

4.2 Energy spectrum

Like discussed in the previous chapter, the energy spectrum of classical acoustic turbulence settles to a universal form where a k^{-2} power law appears in the inertial range when shocks are present in the flow. We have confirmed with our numerical simulations in Papers I and III that the universality

of the energy spectrum still holds with the fluid equations we have employed and that an additional power law appears at small wavenumbers below the peak of the spectrum whose value depends on the dimensionality. This shape for the spectrum is obtained regardless of the initial conditions as long as the Reynolds number is high enough, making it possible to model the spectrum as a broken power law at wavenumbers below the dissipation range

$$E(k) = A\frac{(k/k_p)^\beta}{1+(k/k_p)^\alpha}\,, \quad k \ll 1/L_T\,, \tag{4.31}$$

where β is the low-k power law index, and $\beta - \alpha$ the inertial range power law index.

To extract the power law indices from the simulations, we have made fits to the energy spectra obtained numerically from the simulation data. In both of our studies the fitting function is the broken power law function above. At early times the spectrum from the simulations is subject to oscillations at small wavenumbers. This effect is also known as ringing, and it follows from two primary contributions. The first results from applying Fourier transforms to functions that contain discontinuities or steep discontinuity-like features, like shocks, which can lead to oscillating behaviour. Fast Fourier Transforms have trouble dealing with discontinuities and can lead to reduced accuracy and ringing effects in cases where discontinuities are present (for example, see information about the Gibbs effect [270]). Fourier transforms of discontinuities can also produce oscillating functions in Fourier space; for example, a Fourier transform of a rectangular function gives the sinc-function. When considering a velocity field, this would induce oscillations of the sinc^2 type into the energy spectrum that dampen with increasing wavenumber, similar to what is seen in our simulations. The second effect follows from the way the simulations are initialized. Because the energy density is initially uniform, the continuity equation is not satisfied at the initial time. When the state of the fluid is advanced, the velocity field generates blops of energy density on the uniform background that spread out in the shape of spherical shells. The Fourier transform of such a spherical shell can also be related to the sinc-function, and therefore lead to oscillations in the energy spectrum. A similar effect in a slightly different context has been discussed in Ref. [271]. All in all, these oscillations affect the fits, so in order to deal with them, we have introduced averaging in time over the fitting parameters. The averaging interval should be chosen so that therein the oscillations have already significantly dampened while still being early enough for the energy dissipation not to considerably affect the power law ranges. In Paper I we have decided the suitable limits to be $[1/6L, 1/L_T]$ for the fitting range in wavenumbers, and $8 \leq t_s/t \leq 12$ for the averaging interval that results in about 120 data points per run. In Paper III these limits, in turn, are $2/3L_K$ from above and unbounded from below for the wavenumbers, and $9 \leq t_s/t \leq 11$ in time leading to about 80 data points in the time averaging. The fitting results along with the standard deviations from the time averaging are found in Table II of both papers. The runs are listed in the order of increasing Reynolds number and two trends can be picked up from them, namely that the uncertainty in the results for the low-k power law index tends to increase with increasing Reynolds number, and that the uncertainty of the inertial range power law index conversely decreases. This is explained by the way the high Reynolds number runs are initialized. The initial Reynolds number in these runs is boosted by moving the peak of the spectrum towards larger scales, which leads to an increase in the value of the integral scale L. In turbulent flows L increases over time, moving the spectrum further

towards smaller wavenumbers. Therefore, in these high Re runs, the wavenumber corresponding to the location of the peak and the smallest wavenumber in the simulation k_1 are close to each other and the range in which the low-k power law can be measured ends up being small. Furthermore, the first few bins in the energy spectrum are subject to oscillations that lead to variation in the measured fit parameters. This lack of dynamic range explains the increasing uncertainty in β, while the decrease in the uncertainty of the inertial range power law follows from the fact that in high Reynolds number runs the inertial range is wider, which makes it easier to fit to. In the 2D simulations of Paper I the average power law values are found to be about $k^{-2.1}$ for the inertial range and $k^{2.5}$ at low wavenumbers while the corresponding values are about $k^{-2.3}$ and $k^{4.0}$ in the 3D case of Paper III. In both cases the obtained values are slightly steeper than the classically expected KP spectrum of k^{-2}. However, the results of Paper III display an approach towards this value with increasing Reynolds number (see Fig. 10) but higher Reynolds number runs would be needed to determine whether there is a convergence.

As acoustic turbulence decays, the universal broken power law form for the energy spectrum in Eq. (4.31) is maintained on wavenumbers below the dissipation range, which can be seen in Figure 4 of Paper I. The two time dependent effects on the spectrum in this region are the decrease in the amplitude as a result of the loss in kinetic energy due to viscous dissipation, and a shift in the peak towards larger scales due to increase in the integral length scale over time. The time dependence embedded into these two processes can be extracted from the spectrum by considering the constraints the definitions of the energy spectrum and the integral length scale impose on the broken power law function defined at the start of this section. Substituting Eq. (4.31) into (3.81) and computing the integral gives a relation between the integral length scale, the peak wavenumber, and the power law indices as

$$k_p L \equiv \kappa_p \approx \frac{\sin\left[\frac{\pi(\beta+1)}{\alpha}\right]}{\sin\left(\frac{\pi\beta}{\alpha}\right)}, \tag{4.32}$$

which defines the dimensionless quantity κ_p. Here the result is approximate because we have extended the integration range from $1/L_T$ to infinity, which is justified at high Reynolds numbers where the inertial range is long and by far the largest contribution to the integral is obtained around the peak of the spectrum and in the inertial range power law range. The other condition follows from substituting (4.31) into (3.79), which after computing the integral in a similar way and using the previous result to replace k_p gives the amplitude as

$$A \approx \bar{v}^2 L \frac{\alpha}{\pi} \sin\left(\frac{\pi\beta}{\alpha}\right). \tag{4.33}$$

These conditions imply that only two of the four parameters in the broken power law function are independent for strong turbulence. Using these results with a dimensionless wavenumber scaled by the integral length scale $\kappa = kL$ makes it possible to write the time dependence of the spectrum as

$$E(\kappa, t) = L(t)\mathcal{E}(t)\Psi(\kappa), \quad \kappa = L(t)k, \tag{4.34}$$

where $\mathcal{E} = \left\langle \mathbf{v}^2 \right\rangle /2$ is the kinetic energy, and $\Psi(\kappa)$ is a self-similar spectral shape function of the form

$$\Psi(\kappa) = \Psi_0 \frac{(\kappa/\kappa_p)^\beta}{1 + (\kappa/\kappa_p)^\alpha}, \quad \kappa \ll L/L_T \tag{4.35}$$

with an amplitude

$$\Psi_0 \approx \frac{2\alpha}{\pi} \sin\left(\frac{\pi\beta}{\alpha}\right) . \tag{4.36}$$

Here the time dependence is only through L and $\mathcal{E}$ because the power law indices remain approximately constant as long as the fluid remains shocky enough. Therefore, when the function $\Psi(\kappa)$ is plotted, it remains constant in time, and various spectra plotted at different times in the simulations collapse onto each other in the region where the broken power law form holds, as can be seen in Fig. 5 of Paper I. In the high-κ region ($\kappa \gg L/L_T$) there is still some time dependence due to a reduction in the length of the inertial range as the Reynolds number decreases, followed by a decrease in the amplitude. This is the small scale dissipative region of the spectrum, and we have ascribed the time dependence here to be induced by the change of the shock wave shape over time due to viscous dissipation. Hence, we have proposed that the overall spectrum, valid also outside the self-similar decay region, can be written as the broken power law function (4.35) that is modulated by a function that depends on the shock width.

In order to find the modulating function, and to establish a connection to the shock width parameter $\delta_s \sim 1/k_s$, we have used the tanh shock profile found in the previous section. In this effectively 1D situation the energy spectrum can be obtained as the square of the modulus of the Fourier space velocity profile, yielding

$$E_1(k) = |\mathcal{F}(\tanh(k_s x))|^2 = \frac{\pi^2}{k_s^2} \mathrm{csch}^2\left(\frac{\pi k}{2k_s}\right) , \tag{4.37}$$

where the Fourier transform operation has been denoted by $\mathcal{F}$, and $\mathrm{csch}(x) = 1/\sinh(x)$ is the hyperbolic cosecant function. We take this to be the contribution to the energy spectrum associated with individual shocks in the flow. The 1D energy spectrum can be obtained by integrating the D-dimensional energy spectrum over all possible directions in the wavenumber space except the direction the 1D spectrum is associated with, that is

$$E_1(k_1) = \int E_D(|\mathbf{k}|) d\mathbf{k}_\perp , \tag{4.38}$$

where D is the number of dimensions, and $\mathbf{k} = \mathbf{k}_\perp + \mathbf{k}_1$ with $\mathbf{k}_\perp = \mathbf{k}_2 + \cdots + \mathbf{k}_D$ containing all the coordinate wavevector components parallel to $\mathbf{k}_1$. Because k_1 is kept constant in the integration, we have in D dimensions using spherical coordinates that

$$d\mathbf{k}_\perp = k_\perp^{D-1} dk_\perp d\Omega_{D-1} \tag{4.39}$$

$$= (k^2 - k_1^2)^{\frac{D-1}{2}} dk\, d\Omega_{D-1} \tag{4.40}$$

$$= \frac{1}{2}(s^2 - k_1^2)^{\frac{D-3}{2}} ds^2\, d\Omega_{D-1} , \tag{4.41}$$

where $d\Omega_{D-1}$ is the $D-1$ dimensional solid angle containing the angular part of the integration, and we have denoted $s \equiv k$ on the last line to make the integration variable stand out better. Using this and carrying out the angular integration gives

$$E_1(k_1) = \frac{1}{2}\Omega_{D-1} \int_{k_1^2}^{\infty} E_D(s)(s^2 - k_1^2)^{\frac{D-3}{2}} ds^2 , \tag{4.42}$$

where

$$\Omega_{D-1} = \frac{2\pi^{\frac{D-1}{2}}}{\Gamma\left(\frac{D-1}{2}\right)} \tag{4.43}$$

is the solid angle of a $(D-2)$-sphere, with Γ being the gamma function. This is where the dimensionality of the problem comes in, meaning that we find different modulating functions in the 2D and 3D cases of Papers I and III. Here we follow the simpler 3D case and mention the result of the 2D derivation at the end. For $D = 3$ using the result for $E_1(k)$ one gets the relation

$$\int_{k_1}^{\infty} sE_3(s)\, ds = \frac{\pi}{2k_s^2}\operatorname{csch}^2\left(\frac{\pi k_1}{2k_s}\right), \tag{4.44}$$

which can be readily inverted to solve for the 3D spectrum $E_3(k)$. Denoting $f(s) = sE_3(s)$ and its integral function by $F(s)$ means that

$$\int_{k_1}^{\infty} sE_3(s)\, ds = \lim_{s\to\infty} F(s) - F(k_1), \tag{4.45}$$

and since

$$\lim_{s\to\infty} \operatorname{csch}^2(s) = 0, \tag{4.46}$$

one finds that

$$f(s) = sE_3(s) = -\frac{\pi}{2k_s^2}\frac{d}{ds}\operatorname{csch}^2\left(\frac{\pi s}{2k_s}\right) \tag{4.47}$$

$$= \frac{\pi^2}{2k_s^3}\frac{\cosh\left(\frac{\pi k}{2k_s}\right)}{\sinh^3\left(\frac{\pi k}{2k_s}\right)}, \tag{4.48}$$

from which it follows that the 3D spectrum is

$$E_3(k) = \frac{\pi^2}{2k_s^3 k}\frac{\cosh\left(\frac{\pi k}{2k_s}\right)}{\sinh^3\left(\frac{\pi k}{2k_s}\right)}. \tag{4.49}$$

Because we intend to use this as a modulating function, we are not concerned about the overall amplitude, which can be scaled away by writing

$$E_3 = \frac{\pi^3}{4k_s^4}\mathcal{I}, \qquad P = \frac{\pi k}{2k_s}, \tag{4.50}$$

giving the modulating function $\mathcal{I}$ as

$$\mathcal{I}(P) = \frac{1}{P}\frac{\cosh(P)}{\sinh^3(P)} \sim \begin{cases} \dfrac{1}{P^4}, & P \ll 1 \\ \dfrac{4}{P}e^{-2P}, & P \gg 1, \end{cases} \tag{4.51}$$

which also shows the function's asymptotic behaviour at small and large values of the argument. Applying this as a modulating function to the spectral shape function $\Psi(\kappa)$ gives

$$\Psi(\kappa) = \widetilde{\Psi}_0\frac{(\kappa/\kappa_p)^{\beta+4}}{1+(\kappa/\kappa_p)^{\alpha}}\mathcal{I}\left(\frac{\pi\kappa}{2\kappa_s}\right), \tag{4.52}$$

where the low wavenumber behaviour of the modulating function has been taken into account, scaling the power law index in the numerator so that β still denotes the low-k power law of the energy spectrum, leading to the relation

$$\widetilde{\Psi}_0 = \left(\frac{\pi\kappa_p}{2\kappa_s}\right)^4 \Psi_0 \tag{4.53}$$

in the amplitude so that at $\kappa \ll L/L_T$ Eq. (4.35) is recovered. The time dependence is introduced through the parameter k_s in $\kappa_s = k_s L$ that gets smaller over time as the shock width increases, applying an exponential suppression to the spectrum at length scales much smaller than the shock width. In the 2D case of Paper I Eq. (4.42) becomes more complicated and the resulting modulating function can be written as an integral

$$I_{2\mathrm{D}}(P) = \int_1^\infty \frac{ds}{\sqrt{s^2-1}} \frac{\cosh(Ps)}{\sinh^3(Ps)} \sim \begin{cases} \dfrac{\pi}{4P^3}, & P \ll 1 \\ 2\sqrt{\dfrac{\pi}{P}} e^{-2P}, & P \gg 1, \end{cases} \tag{4.54}$$

which does not have a closed form solution.

The validity of the spectral shape function $\Psi(\kappa)$ has been tested by fitting it to the simulation data. Examples of the fits in low Reynolds number runs can be seen in Fig. 7 of Paper I and Fig. 8 of Paper III at $t = 20t_s$, showing a good agreement with the obtained result. The fits get slightly worse as the Reynolds number increases because of effects that deform the spectrum, like the previously discussed oscillations, and the so-called bottleneck effect [272, 273] that can lead to a formation of a bump in the spectrum at wavenumbers just below the dissipation range. In Paper III we have performed fits similar to those seen in the figures for all featured runs and extracted the values of the power law indices and the κ_s parameters that can be found in Table I. The results for the former are not as reliable in this case as with the averaged broken power law fits discussed at the start of this section, but they do allow us to tap into the shock width parameter via κ_s. The fits show a clear increasing trend in its value with increasing Reynolds number, and when plotted against the value of the Reynolds number at the fitting time, a linear trend emerges, illustrated in Fig. 9. With a linear fit $\kappa_s = d\mathrm{Re}$ we find a slope of $d = 0.630 \pm 0.014$. On the other hand, using the definition of the Reynolds number in Eq. (3.77), one can write

$$\kappa_s = k_s L = d\mathrm{Re} = d\frac{\bar{v}L}{\mu} \tag{4.55}$$

$$\Rightarrow k_s = d\frac{\bar{v}}{\mu}. \tag{4.56}$$

Using the numerical value for d from the fit then gives the shock width as

$$\delta_s = \frac{1}{k_s} = \frac{1}{d}\frac{\mu}{\bar{v}} \approx 1.588\frac{\mu}{\bar{v}}, \tag{4.57}$$

which is in line with the shock width formula of Eq. (3.87) resulting from dimensional analysis with a constant of proportionality close to unity. The result demonstrates and confirms the connection between the steepness of the shocks and the high wavenumber behaviour of the spectrum.

Our numerical simulations show a generation of small amounts of vortical energy even though the initial conditions are purely longitudinal. The vorticity generation can be studied analytically by taking a curl of the Navier-Stokes equation (3.74). Here we skip the details of the calculation found in section IIIE of Paper III and only discuss the result. When there is no initial vorticity, so that $\boldsymbol{\omega} = \nabla \times \mathbf{v} = \mathbf{0}$, the equation can be written as

$$\frac{\partial \boldsymbol{\omega}}{\partial t} = c_s^2 \left[\nabla(\nabla \cdot \mathbf{v}) + (\nabla \ln \rho \cdot \nabla)\mathbf{v} + (\mathbf{v} \cdot \nabla)\nabla \ln \rho\right] \times \mathbf{v} + \frac{2\eta}{1+c_s^2}\nabla \times (\mathsf{S} \cdot \nabla \ln \rho) + \frac{\nu}{1+c_s^2}\nabla(\nabla \cdot \mathbf{v}) \times \nabla \ln \rho\,, \quad (4.58)$$

where the term containing the shear rate tensor S_{ij} has the explicit form

$$\nabla \times (\mathsf{S} \cdot \nabla \ln \rho) = (\nabla \times \mathsf{S}) \cdot \nabla \ln \rho + \varepsilon_{ijk} S_{\ell j} \partial_i \partial_\ell \ln \rho \, \hat{\mathbf{e}}_k \quad (4.59)$$

with

$$\nabla \times \mathsf{S} = \varepsilon_{ijk} \partial_i S_{\ell j} \hat{\mathbf{e}}_k \otimes \hat{\mathbf{e}}_\ell\,, \quad (4.60)$$

where $\hat{\mathbf{e}}_i$ are Cartesian basis vectors. The first three terms on the RHS are proportional to the speed of sound, therefore resulting from the use of the ultrarelativistic equation of state when deriving the fluid equations. Because of it, these terms would not be present in the purely classical case and the only term contributing would be the viscosity term. The first term on the RHS is the dominant one while the rest of the $\nabla \ln \rho$ terms give sizable contributions only in the vicinity of shock waves. The magnitude of the emerging vorticity field in a simulation run has been plotted in Fig. 12 of Paper I and Fig. 13 of Paper III. The vorticity field, in a descriptive sense, can be divided into two components, the first being the slowly evolving background vorticity, and the second the quickly evolving contribution resulting from the moving shock fronts. The latter contribution dominates at early times and the vorticity reaches its largest values in regions containing overlapping shock waves (i.e. in shock collisions). These features are short-lived and change location as the shocks propagate. At late times when the shocks get dissipated, the background vorticity becomes the dominant one, and the shock fronts are only faintly visible in the vorticity field. In our 2D simulations we see an emergence of vortex-like structures in the background vorticity in the largest Reynolds number runs (see Fig. 12d in Paper I) that appear in pairs of different signs. We do not see these in the corresponding 3D simulations, but this could be due to the vorticity being more difficult to visualize compared to 2D. Generally speaking, the higher the Reynolds number of the run is, the higher the fraction of the kinetic energy that ends up in transverse modes. However, in the range of Reynolds numbers we have studied in the papers, the generated vorticity ends up being small and not strong enough to show any features characteristic to vortical turbulence, like high values of the transverse Reynolds number $\mathrm{Re}_\perp$, a presence of a clear inertial range in the transverse energy spectrum $E_\perp(k)$, or fully developed vortices in the vorticity fields, like in Fig. 3.1d.

4.3 Decay

After a first-order phase transition has completed, no more energy is being injected into the fluid, causing it to decay freely due to the viscous dissipation. The free decay is also a feature of our

fluid equations (3.73) and (3.74) since they lack a forcing term. The dissipation rate of the kinetic energy $\mathcal{E} = \left\langle \mathbf{v}^2 \right\rangle /2$ can be computed in a similar way as in the derivation of the viscous dissipation rate in Eq. (3.83) but this time including all terms and not just the viscosity containing ones. That means taking a dot product with respect to the velocity and averaging both sides of the equation. Assuming that the averages can be treated as volume averages, gradients of the logarithmic energy density can be considered first order small quantities, since they give significant contributions only at shock fronts, which constitute only a small part of the total volume. This leads to the last two terms on the RHS and the second to last term on the LHS (in reference to Eq. (3.74)) being of the order $O(\epsilon^4)$ in the resulting equation. Further assuming the energy in the rotational modes to be small in comparison to the longitudinal energy ($\nabla \times \mathbf{v} \approx \mathbf{0}$), one obtains

$$\frac{1}{2}\frac{\partial \left\langle \mathbf{v}^2 \right\rangle}{\partial t} + \langle \mathbf{v} \cdot (\mathbf{v} \cdot \nabla)\mathbf{v} \rangle - c_s^2 \left\langle v^2 (\nabla \cdot \mathbf{v}) \right\rangle + \frac{c_s^2}{1+c_s^2} \langle \mathbf{v} \cdot \nabla \ln \rho \rangle = \frac{\mu}{1+c_s^2} \left\langle \mathbf{v} \cdot \nabla^2 \mathbf{v} \right\rangle + O(\epsilon^4) \,. \tag{4.61}$$

Two of the terms on the LHS can be modified using vector calculus

$$\langle \mathbf{v} \cdot (\mathbf{v} \cdot \nabla)\mathbf{v} \rangle = \frac{1}{2} \left\langle \nabla \cdot (v^2 \mathbf{v}) \right\rangle - \frac{1}{2} \left\langle v^2 (\nabla \cdot \mathbf{v}) \right\rangle \tag{4.62}$$

$$\langle \mathbf{v} \cdot \nabla \ln \rho \rangle = \langle \nabla \cdot (\mathbf{v} \ln \rho) \rangle - \langle (\nabla \cdot \mathbf{v}) \ln \rho \rangle \,, \tag{4.63}$$

where the first terms on the RHS in both equations vanish after writing the volume average in an integral form (see Eq. (3.123)) and using the divergence theorem while imposing that the velocity vanishes at the infinite boundary. Up to third order in the small quantities, the differential equation for the kinetic energy $\mathcal{E}$ then becomes

$$\frac{\partial \mathcal{E}}{\partial t} = \frac{\mu}{1+c_s^2} \left\langle \mathbf{v} \cdot \nabla^2 \mathbf{v} \right\rangle + \frac{c_s^2}{1+c_s^2} \langle (\nabla \cdot \mathbf{v}) \ln \rho \rangle + \frac{1}{2} \left(1 + 2c_s^2\right) \left\langle v^2 (\nabla \cdot \mathbf{v}) \right\rangle \,. \tag{4.64}$$

All in all, there are three terms that contribute to the change in the kinetic energy. The first one is the viscous dissipation, which we derived already in Chapter 3. The second one follows from the pressure gradient term, and the last term from a combination of the two non-linear terms. From this it is evident that in an incompressible fluid ($\nabla \cdot \mathbf{v} = 0$) only the viscous dissipation contributes to the kinetic energy decay (note that in the incompressible case the viscous dissipation term maintains its form, but the effective viscosity should be replaced by the shear viscosity $\mu \longrightarrow \eta$ because one of the viscosity terms vanishes in the derivation). Because of this, the decay is simpler for irrotational flows, but for acoustic turbulence that only appears in compressible flows, all three terms contribute. In Paper I we incorrectly took into account only the viscous dissipation term, which was corrected in Paper III.

To verify that these three terms describe the decay of kinetic energy, we have measured their magnitude over a simulation run and used the values to reconstruct the kinetic energy using the fourth order Runge-Kutta scheme to solve Eq. (4.64). The result is plotted in Fig. 12 of Paper III along with the kinetic energy measured from simulation data. The curves match each other well, with the remaining differences being attributed to the neglected fourth order small terms. Figure 11 displays each term's contribution to the dissipation rate of the kinetic energy fraction $\mathcal{E}_r = \mathcal{E}/\mathcal{E}_0$, where $\mathcal{E}_0$ is the initial kinetic energy. At early times before the shocks form ($t/t_s < 1$) the oscillating pressure

gradient term dominates and is strongly negative, leading to the sharp decrease in the kinetic energy seen in Fig. 12. The oscillations are believed to be primarily caused by the ringing effect that follows from the way the energy density is initialized in the simulations, like discussed earlier. Therefore, the effect could potentially be lessened by initializing the energy density in a way that the continuity equation is initially satisfied. The oscillations quickly begin to dampen after shock formation and in the range $t/t_s > 2$ the pressure gradient contribution remains positive on average, meaning that it increases the kinetic energy. The other two terms are negative in this range, dissipating energy. The contribution from the non-linear term approaches zero, and becomes negligible compared to the two other terms at late times when $t/t_s > 10$. The dashed dark line shows the total dissipation rate, which at late times approximately follows the viscous dissipation contribution when averaged over the oscillations. This is because on average the pressure gradient contribution approaches zero faster than the viscous one. The kinetic energy as a function of the number of shock formation times is plotted in Fig. 8 of Paper I for multiple simulation runs. At times corresponding to the aforementioned late time-time regime ($t/t_s > 10$), the kinetic energy decays as a power law, and the oscillations induced by the pressure gradient term are clearly seen as small ripples in the kinetic energy curves. In order to extract this power law analytically, based on the behaviour of the terms in Fig. 11 of Paper III, we have approximated that in this late time range the decay is given on average only by the viscous dissipation term so that

$$\frac{\partial \mathcal{E}}{\partial t} \approx \frac{\mu}{1+c_s^2}\left\langle \mathbf{v}\cdot\nabla^2\mathbf{v}\right\rangle = -\frac{\mu}{1+c_s^2}\int_0^\infty k^2 E(k)\,dk\,, \tag{4.65}$$

where we have moved to Fourier space like when deriving Eq. (3.84). To make progress analytically, we split the energy spectrum into three parts using the previously obtained result for it in Eq. (4.34) with the spectral shape function (4.52). At low wavenumbers we extend the low-k power law all the way to the peak of the spectrum, cutting it off at the peak wavenumber k_p. From this point onwards we assume the k^{-2} KP spectrum at the inertial range characteristic to acoustic turbulence, and we take the modulation by the function I of Eq. (4.51) to kick in at the wavenumber corresponding to the shock width length scale. All in all, when formulated, this means that the spectrum is

$$E(k) \approx \begin{cases} \dfrac{L^{\beta+1}\mathcal{E}\Psi_0}{\kappa_p^\beta}k^\beta & k < k_p \\ \dfrac{\mathcal{E}\Psi_0\kappa_p^2}{L}\dfrac{1}{k^2} & k_p \le k \le \delta_s^{-1} \\ \dfrac{\mathcal{E}\Psi_0\kappa_p^2}{L}\left(\dfrac{\pi}{2}\right)^3\delta_s^3 k\dfrac{\cosh(\pi\delta_s k/2)}{\sinh^3(\pi\delta_s k/2)} & k > \delta_s^{-1}\,. \end{cases} \tag{4.66}$$

This approximation leads to an overestimation of the integral in two regions. The first is the overestimation due to the sharp peak that follows from extending the two power law ranges, but this is negligible at high Reynolds numbers because of the additional k^2 scaling of the integrand. The second overestimation results from extending the inertial range to $k = \delta_s^{-1}$ when in reality the spectrum has already started to fall off by this point. The approximation causes the integral in Eq. (4.65)

to split into three parts

$$\int_0^\infty k^2 E(k) = \mathcal{E}\Psi_0 \left[\frac{L^{\beta+1}}{\kappa_p^\beta} \int_0^{k_p} dk\, k^{\beta+2} + \frac{\kappa_p^2}{L} \int_{k_p}^{\delta_s^{-1}} dk + \left(\frac{\pi}{2}\right)^3 \frac{\kappa_p^2 \delta_s^3}{L} \int_{\delta_s^{-1}}^\infty dk\, k^3 \frac{\cosh(\pi\delta_s k/2)}{\sinh^3(\pi\delta_s k/2)} \right] \tag{4.67}$$

$$= \mathcal{E}\Psi_0\kappa_p^2 \left[\frac{\kappa_p}{\beta+3}\frac{1}{L^2} + \frac{\delta_s^{-1}}{L} - \frac{\kappa_p}{L^2} + \frac{\delta_s^{-1}}{L}\frac{2}{\pi} \int_{\pi/2}^\infty dx\, x^3 \frac{\cosh(x)}{\sinh^3(x)} \right], \tag{4.68}$$

where in the last integral a change of variables $x = \pi\delta_s k/2$ has been performed. After combining terms, Eq. (4.65) becomes

$$\frac{\partial \mathcal{E}}{\partial t} = -\frac{\mu}{1+c_s^2} \mathcal{E}\Psi_0\kappa_p^2 \left(\mathcal{A}\frac{\delta_s^{-1}}{L} - \frac{\beta+2}{\beta+3}\frac{\kappa_p}{L^2} \right), \tag{4.69}$$

where the numerical factor $\mathcal{A}$ has been defined as

$$\mathcal{A} = 1 + \frac{2}{\pi} \int_{\pi/2}^\infty x^3 \frac{\cosh x}{\sinh^3 x}\, dx \approx 1.62\,. \tag{4.70}$$

We want to make this into a differential equation for $\mathcal{E}(t)$ only so that the kinetic energy can be solved from it. At high Reynolds numbers κ_p and Ψ_0 are approximatively given be Eqs. (4.32) and (4.36), meaning that they can be treated as constants in time. Hence, all time dependence lies in the parameters $\delta_s(t)$ and $L(t)$. The former can be written in terms of the kinetic energy by using Eq. (4.57) with the constant of proportionality d, and the definitions of the rms velocity and the kinetic energy to yield

$$\delta_s^{-1}(t) = d\frac{\sqrt{2\mathcal{E}(t)}}{\mu}\,. \tag{4.71}$$

The integral length scale can be related to the kinetic energy by inspecting the behaviour of the spectrum at low wavenumbers. Figure 4 of Paper I shows that in this region the spectrum does not change much during the decay, so it can be approximated as a constant. From Eq. (4.66) it then follows that

$$\mathcal{E}(t) L^{\beta+1}(t) = \text{const.} \tag{4.72}$$

which when related to some initial values at an initial time t_0 gives

$$L^{-1}(t) = L_0^{-1} \mathcal{E}_r^{1/(1+\beta)}(t)\,, \tag{4.73}$$

where $\mathcal{E}_r = \mathcal{E}/\mathcal{E}_0$ is the kinetic energy fraction. When the differential equation is written in terms of it after replacing the shock width and the integral length scale using the previous results, one can write

$$\frac{d\mathcal{E}_r}{dt} = -B\left(\mathcal{E}_r^{\frac{3\beta+5}{2(\beta+1)}} - D\mathcal{E}_r^{\frac{\beta+3}{\beta+1}} \right) \tag{4.74}$$

where the coefficients B and D are

$$B = \mathcal{A}d\frac{\Psi_0\kappa_p^2}{1+c_s^2}\frac{1}{t_s} \tag{4.75}$$

$$D = \frac{\kappa_p}{\mathcal{A}d}\frac{\beta+2}{\beta+3}\frac{1}{\mathrm{Re}_0}\,, \tag{4.76}$$

with Re_0 being the initial Reynolds number, and $t_s = L_0/\bar{v}_0$ the shock formation time. The solution of the differential equation can be expressed in terms of the hypergeometric function ${}_2F_1$ as

$$\mathcal{E}_r(t)^{-\frac{\beta+3}{2(\beta+1)}}\,{}_2F_1\left(1, \frac{\beta+3}{\beta-1}; \frac{2(\beta+1)}{\beta-1}; D\mathcal{E}_r(t)^{\frac{1-\beta}{2(\beta+1)}}\right) = C\frac{t}{t_s} + C', \tag{4.77}$$

where C' is an integration constant, and we have used the notation

$$C = \frac{\mathcal{A}d}{2}\frac{\beta+3}{\beta+1}\frac{\Psi_0\kappa_p^2}{1+c_s^2}. \tag{4.78}$$

The hypergeometric series is close to unity when

$$\frac{\mathcal{E}(t)}{\mathcal{E}_0} \gg \left(\frac{\kappa_p}{\mathcal{A}d}\frac{\beta+2}{\beta+3}\frac{1}{\mathrm{Re}_0}\right)^{\frac{2(\beta+1)}{\beta-1}}, \tag{4.79}$$

or in terms of the integral length scale

$$\frac{L(t)}{L_0} \ll \left(\frac{\mathcal{A}d}{\kappa_p}\frac{\beta+3}{\beta+2}\mathrm{Re}_0\right)^{\frac{2}{\beta-1}}. \tag{4.80}$$

In other words, the subsequent terms in the series become important at low Reynolds numbers where the inertial range is short and the contributions to the viscous dissipation integral around the peak of the spectrum are more prominent. We have checked in Paper III that all of our simulation runs fulfil these conditions well for $\beta = 4$ and $d = 0.63$, so we do not expect the subleading terms in the series to contribute much. Therefore, at high Reynolds numbers ${}_2F_1 \approx 1$, and the kinetic energy can be easily solved with the initial condition $\mathcal{E}(0) = \mathcal{E}_0$, yielding

$$\mathcal{E}(t) = \frac{\mathcal{E}_0}{\left(1 + C\frac{t}{t_s}\right)^{\zeta}}, \quad \zeta = \frac{2(\beta+1)}{\beta+3}, \tag{4.81}$$

which can be used to also solve for the integral length scale $L(t)$ using the relation in Eq. (4.72), resulting in

$$L(t) = L_0\left(1 + C\frac{t}{t_s}\right)^{\lambda}, \quad \lambda = \frac{2}{\beta+3}. \tag{4.82}$$

At late times the kinetic energy and the integral length scale power laws ζ and λ respectively are thus given by the low-k power law β of the energy spectrum. The parameter C is the decay constant that sets the number of shock formation times it takes for the flow to start decaying with small values leading to slower decay. These results are of course only valid at late times when the pressure gradient term in the energy dissipation equation no longer dictates the decay, so they describe how the flow would have decayed from the start if only the viscous dissipation contributed. The derivation relies on the universal properties of the k^{-2} KP spectrum of acoustic turbulence and the stationarity of the spectrum at low wavenumbers, meaning that it does not depend on the dimensionality. Therefore, these same results were also found in the 2D study of Paper I, although using a different derivation method based on Saffman's analysis of the vortical case [274] that we applied to acoustic turbulence. The power law values for ζ and λ in terms of the low-k power law index are also similar to those found for classical vortical turbulence [275]. Rather interestingly, the result in

Eq. (4.81) and the decay constant C in Eq. (4.78) that sets the kinetic energy decay rate are independent of the viscosity even though it is responsible for the decay. This independence in the limit of high Reynolds numbers is known as the zeroth law of turbulence. There are also relations that the results and the used assumptions impose on the power law indices. The first one results from the stationarity condition in Eq. (4.72) as

$$\lambda(\beta + 1) - \zeta = 0\,, \tag{4.83}$$

and another from solving for and replacing β in the results for ζ and λ, yielding

$$\zeta - 2(1 - \lambda) = 0\,. \tag{4.84}$$

We have tested the results of this section by fits to the simulation data in Papers I and III. In Paper I the fitting range is unbounded from above, capping at the end of the run at about 60 shock formation times, and the lower bound is varied between $1 \leq t/t_s \leq 3$ to introduce time averaging to the results. Examples of individual fits to the kinetic energy and the integral length scale are plotted in Fig. 10. The results for the power law indices ζ and λ obtained this way are listed in Table I along with the values that follow from the measured low-k power laws β using Eqs. (4.81) and (4.82). The results show that these values are in a relatively good agreement with each other. The results from the fits have also been used to test the relations between the power law indices in Eqs. (4.83) and (4.84), whose numerical values along with the uncertainties resulting from the standard deviations associated with the time averaging for the fit parameters* are listed in Table III of Paper I. They are also visualized in Fig. 11 that plots the data points in a $\zeta\lambda$-plane, with the values of β corresponding to the slopes of lines passing through the origin, and the relation in Eq. (4.84) resulting in the solid black line in the plot. Similar plots have also been presented in Ref. [276]. For the majority of the runs, the relations are fulfilled well, and the values are within the standard deviations. For relation (4.84) the standard deviations end up being smaller because it does not involve β, whose measurement is prone to oscillations. The figure however shows that the distribution of the data points around the line following from this relation is quite even and symmetrical, indicating that their mean lies close to it.

In Paper III the simulation runs are shorter, ending after about $20t_s$ in contrast to the earlier $60t_s$. Based on our tests with the 2D data of Paper I, this should be long enough to precisely extract the power law indices ζ and λ from the simulation data by fitting. The fits are still unbounded from above, but the lower bound has been increased and is now varied between $10 \leq t/t_s \leq 13$ so that the fits lie in the late time region where Eq. (4.81) is valid. We have not included the measurements for the integral length scale power law index λ in this case. This is because most of the simulation runs show a decrease in the value of the integral length scale right after shock formation that lasts for a few shock formation times. This feature was not present in the 2D case, and it makes accurately fitting into the data difficult since the fitting function in Eq. (4.82) does not account for decreasing behaviour. We believe that this might be caused by the reduction in the dynamic range in the

*The errors from the fits themselves (fitting covariances) are found to be negligible compared to the standard deviations from the time averaging. We have also measured the magnitude of the statistical fluctuations from using random initial conditions, and those are found to be at the largest comparable in magnitude to the errors from time averaging.

simulations when moving from 2D to 3D, as we have ruled out the possibility of it being due to improvements made between the papers, like changes in the numerical schemes or the introduction of additional terms into the fluid equations. The decrease is also not reproduced when using the measured decay rates to solve for the integral length scale akin to what was done in Fig. 12, and it is not present in Run I, which has its peak at the highest wavenumber out of all the runs, and thus the largest range between Δk and k_p. The peak being close to the lowest wavenumber also makes it subject to oscillations that show up in the measured values of L as well, which also affects the fits in a negative way. Of these quantities, only L is sensitive to the lack of dynamic range, while the kinetic energy seems to behave as expected, which makes us think this might be a numerical issue stemming from this limitation. This is why we have only included the measurements for the kinetic energy decay power law ζ, and concluded that larger resolution runs with more dynamic range are needed to measure L accurately and to study the origin of its decrease seen in the simulations. The time averaged fitting results for ζ are listed in Table III for each of the runs, and they are on average found to be a bit steeper than in the 2D case, as expected due to a change in the low-k power law index β. Like before, the values predicted by the measured low-k power law indices are also listed alongside, and they are, generally speaking, found to be quite close to the measured values, and within the standard deviations for about half of the runs.

5. Gravitational waves from acoustic turbulence

In this chapter we calculate the gravitational wave power spectrum resulting from acoustic turbulence in the radiation dominated era using the properties found for it in the previous chapter. The starting point is equation (1.81) for the spectral density $P_{h'}(k)$ at the end of section 1.3, which read

$$P_{h'}(k) = 18(1+c_s^2)^2 \int_{\eta_i}^{\eta_f} d\eta_1\, a(\eta_1)\mathcal{H}^2(\eta_1) \int_{\eta_i}^{\eta_f} d\eta_2\, a(\eta_2)\mathcal{H}^2(\eta_2) \cos\left[k(\eta_1-\eta_2)\right] U_\Pi(k,\eta_1,\eta_2)\,, \quad (5.1)$$

where $U_\Pi(k,\eta_1,\eta_2)$ is the UETC of the fluid shear stress, which describes the GW generating source. During the radiation dominated era the scale factor and the Hubble parameter scale as

$$a(\eta) = a_\star \frac{\eta}{\eta_\star}\,, \qquad \mathcal{H}(\eta) = \frac{1}{\eta}\,, \quad (5.2)$$

where the subscript refers to values evaluated at the source activation time, i.e. at the time of the phase transition which generates the turbulence. The spectral density is related to the power spectrum through Eq. (1.66), which had the form

$$\mathcal{P}_{\rm GW}(k) = \frac{1}{12\mathcal{H}^2a^2}\frac{k^3}{2\pi^2}P_{h'}(k)\,. \quad (5.3)$$

Using the RD time scalings above and substituting the equation for $P_{h'}(k)$ into Eq. (5.3) gives

$$\mathcal{P}_{\rm GW}(k) = \frac{3(1+c_s^2)^2}{4\pi^2}k^3 \int_{\eta_i}^{\eta_f}\frac{d\eta_1}{\eta_1}\int_{\eta_i}^{\eta_f}\frac{d\eta_2}{\eta_2}\cos\left[k(\eta_1-\eta_2)\right] U_\Pi(k,\eta_1,\eta_2)\,. \quad (5.4)$$

In the articles featured in this thesis, we have also worked in the limit where the timescale of the turbulence t_s is assumed to be small compared to the Hubble time $H_\star^{-1}$. The expansion of the universe can then be neglected during the sourcing, and a along with $\mathcal{H}$ can be treated as constants in time. Then using the conversion rules introduced at the end of section (1.2), i.e. $a \to a_\star = 1$, $\eta \to t$, and $\mathcal{H} \to H_\star$, the GW power spectrum becomes

$$\mathcal{P}_{\rm GW}(k) = \frac{3(1+c_s^2)^2}{4\pi^2}H_\star^2k^3 \int_{t_i}^{t_f} dt_1 \int_{t_i}^{t_f} dt_2 \cos\left[k(t_1-t_2)\right] U_\Pi(k,t_1,t_2)\,. \quad (5.5)$$

To take into account both the short- and long-lived sources simultaneously, we introduce the notation

$$\mathcal{P}_{\rm GW}(k) = \frac{3(1+c_s^2)^2}{4\pi^2} k^3 \int_{\eta_i}^{\eta_f} d\eta_1 \int_{\eta_i}^{\eta_f} d\eta_2 \, \sigma(\eta_1,\eta_2) \cos\left[k(\eta_1-\eta_2)\right] U_\Pi(k,\eta_1,\eta_2)\,, \tag{5.6}$$

where

$$\sigma(\eta_1,\eta_2) = \begin{cases} \dfrac{1}{H_\star^{-2}} & \text{without expansion } (t_s \ll H_\star^{-1}) \\ \dfrac{1}{\eta_1\eta_2} & \text{with expansion}\,, \end{cases} \tag{5.7}$$

and where in the non-expanding case η corresponds to the cosmic time t.

5.1 Shear stress correlator for acoustic waves

Calculating the GW power spectrum now requires the determination of the UETC function $U_\Pi(k,\eta_1,\eta_2)$. However, the behaviour of the spectrum at low wavenumbers can be determined already from Eq. (5.6) for any stochastic source that is active after inflation. For super-horizon scales ($k < \mathcal{H}$) the stochastic signal consists of contributions from patches of the universe that are not in causal contact with each other. This means that the anisotropic stresses $\tilde{\Pi}_{ij}$ are uncorrelated on these length scales, and the UETC function U_Π has a white noise (flat) spectrum in k. Then from Eq. (5.6) it follows that $\mathcal{P}_{\rm GW}(k) \propto k^3$ for scales that were super-horizon at the time of production [277].

The energy momentum tensor can be written as

$$T_{ij}(\mathbf{x},\eta) = a(\eta)^2(\rho+p)v_i(\mathbf{x},\eta)v_j(\mathbf{x},\eta)\,, \tag{5.8}$$

where we have assumed non-relativistic fluid bulk velocities and dropped the diagonal trace contribution that does not source any gravitational waves. We had already scaled out the enthalpy density $\rho + p$ in Eq. (1.69) to define the dimensionless anisotropic stress tensor $\tilde{\Pi}_{ij}$. Fourier transforming the above equation and comparing with (1.69) gives

$$\tilde{\Pi}_{ij}(\mathbf{k},\eta) = \int \frac{d^3q}{(2\pi)^3} v_i(\mathbf{q},\eta)v_j(\mathbf{k}-\mathbf{q},\eta)\,, \tag{5.9}$$

where the Fourier convolution theorem has been used to write the Fourier transform of $\tilde{\Pi}_{ij}(\mathbf{x})$ as a convolution of the Fourier transforms of $v_i(\mathbf{x})$ and $v_j(\mathbf{x})$. Using this, we can then calculate the UETC two-point function as

$$\begin{aligned} \left\langle \tilde{\Pi}_{ij}^{TT}(\mathbf{k},\eta_1)\tilde{\Pi}_{ij}^{\star TT}(\mathbf{k}',\eta_2)\right\rangle &= \Lambda_{ij,lm}(\mathbf{k})\Lambda_{ij,rs}(\mathbf{k}')\left\langle \tilde{\Pi}_{lm}(\mathbf{k},\eta_1)\tilde{\Pi}_{rs}^{\star}(\mathbf{k}',\eta_2)\right\rangle \\ &= \Lambda_{ij,lm}(\mathbf{k})\Lambda_{ij,rs}(\mathbf{k}') \int \frac{d^3q_1}{(2\pi)^3}\frac{d^3q_2}{(2\pi)^3} \left\langle v_l(\mathbf{q}_1,\eta_1)v_m(\mathbf{k}-\mathbf{q}_1,\eta_1)v_r^\star(\mathbf{q}_2,\eta_2)v_s^\star(\mathbf{k}'-\mathbf{q}_2,\eta_2)\right\rangle\,, \end{aligned} \tag{5.10}$$

where we have used the transverse-traceless projector of Eq. (1.33). We are now met with an average over four velocity factors that are evaluated at two different times. For turbulence, there are no known general solutions for such expressions, so the best we can do is to assume that the four-point function factors into a product of pairs of two-point functions like in the case of a Gaussian

field. This could be a somewhat ill approximation in the case of acoustic turbulence, as the velocity field is believed to lose its Gaussianity as the sound waves steepen into shocks. We assume the deviations from Gaussianity to be small, but we acknowledge this as a potential source of error in the calculation. Using Wick's theorem to contract the pairs of velocities gives

$$\left\langle \tilde{\Pi}_{ij}^{TT}(\mathbf{k},\eta_1)\,\tilde{\Pi}_{ij}^{\star TT}(\mathbf{k}',\eta_2)\right\rangle = \Lambda_{ij,lm}(\mathbf{k})\Lambda_{ij,rs}(\mathbf{k}')\int \frac{d^3q_1}{(2\pi)^3}\frac{d^3q_2}{(2\pi)^3}\Big[\tag{5.11}$$

$$\left\langle v_l(\mathbf{q}_1,\eta_1)v_m^\star(\mathbf{q}_1-\mathbf{k},\eta_1)\right\rangle\left\langle v_s(\mathbf{q}_2-\mathbf{k}',\eta_2)v_r^\star(\mathbf{q}_2,\eta_2)\right\rangle$$
$$+\left\langle v_l(\mathbf{q}_1,\eta_1)v_r^\star(\mathbf{q}_2,\eta_2)\right\rangle\left\langle v_m(\mathbf{k}-\mathbf{q}_1,\eta_1)v_s^\star(\mathbf{k}'-\mathbf{q}_2,\eta_2)\right\rangle$$
$$+\left\langle v_l(\mathbf{q}_1,\eta_1)v_s^\star(\mathbf{k}'-\mathbf{q}_2,\eta_2)\right\rangle\left\langle v_m(\mathbf{k}-\mathbf{q}_1,\eta_1)v_r^\star(\mathbf{q}_2,\eta_2)\right\rangle\Big], \tag{5.12}$$

where any non-Gaussianities would lead to extra contributions. In the first term we have also used the fact that the velocities are real to convert from $v_l^\star \to v_l$ and $v_s^\star \to v_s$ using the property $v(-\mathbf{k}) = v^\star(\mathbf{k})$. Since we are dealing with acoustic turbulence, the velocity field is expected to be irrotational. Assuming a statistically homogeneous and isotropic velocity field, we can then define

$$\left\langle v_i(\mathbf{k},\eta_1)v_j^\star(\mathbf{k}',\eta_2)\right\rangle = (2\pi)^3\delta(\mathbf{k}-\mathbf{k}')\hat{k}_i\hat{k}_jG(k,\eta_1,\eta_2)\,, \tag{5.13}$$

where the longitudinal projector operator $P_{ij}^{\parallel}(\mathbf{k}) = \hat{k}_i\hat{k}_j$ has been used to extract the irrotational part [278] of the velocity field UETC function G that is related to the fluid spectral density $P_v(k)$. Substituting this into the previous equation leads to delta functions in the first term that are nonvanishing only for $\mathbf{k} = \mathbf{k}' = 0$, and therefore it does not contribute. The latter two terms both give a product of two delta functions, one of which can be used to carry out the integration over $\mathbf{q}_2$. In both terms the remaining delta function then becomes $\delta(\mathbf{k}-\mathbf{k}')$ that justifies the replacement $\mathbf{k}' \to \mathbf{k}$. Denoting $\mathbf{q} \equiv \mathbf{q}_1$ and $\tilde{\mathbf{q}} = \mathbf{q}-\mathbf{k}$, the result can be written as

$$\left\langle \tilde{\Pi}_{ij}^{TT}(\mathbf{k},\eta_1)\tilde{\Pi}_{ij}^{\star TT}(\mathbf{k}',\eta_2)\right\rangle = \delta(\mathbf{k}-\mathbf{k}')\int d^3q\, G(q,\eta_1,\eta_2)G(\tilde{q},\eta_1,\eta_2)\Lambda(\mathbf{k},\mathbf{q})\,, \tag{5.14}$$

where

$$\Lambda(\mathbf{k},\mathbf{q}) = \Lambda_{lm,rs}(\mathbf{k})\left(\hat{q}_l\hat{\tilde{q}}_m\hat{q}_r\hat{\tilde{q}}_s + \hat{q}_l\hat{\tilde{q}}_m\hat{q}_s\hat{\tilde{q}}_r\right), \tag{5.15}$$

and we have used Eq. (1.36) to combine the two projectors. This can be calculated by applying the projector of Eq. (1.34). Inspecting the latter term gives

$$\Lambda_{lm,rs}(\mathbf{k})\hat{q}_l\hat{\tilde{q}}_m\hat{q}_s\hat{\tilde{q}}_r = \left[P_{lr}(\mathbf{k})P_{ms}(\mathbf{k}) - \frac{1}{2}P_{lm}(\mathbf{k})P_{rs}(\mathbf{k})\right]\hat{q}_l\hat{\tilde{q}}_m\hat{q}_s\hat{\tilde{q}}_r \tag{5.16}$$

$$= \frac{1}{2}P_{lr}(\mathbf{k})P_{ms}(\mathbf{k})\hat{q}_l\hat{\tilde{q}}_m\hat{q}_s\hat{\tilde{q}}_r\,, \tag{5.17}$$

because for each projector P one of the indices couples to q and the other to $\tilde{q}$, so each term gives the same result and they can be combined. Equation (5.15) then becomes

$$\Lambda(\mathbf{k},\mathbf{q}) = \left[P_{lr}(\mathbf{k})P_{ms}(\mathbf{k}) - \frac{1}{2}P_{lm}(\mathbf{k})P_{rs}(\mathbf{k})\right]\hat{q}_l\hat{\tilde{q}}_m\hat{q}_r\hat{\tilde{q}}_s + \frac{1}{2}P_{lr}(\mathbf{k})P_{ms}(\mathbf{k})\hat{q}_l\hat{\tilde{q}}_m\hat{q}_s\hat{\tilde{q}}_r\,, \tag{5.18}$$

where for the same reason as before, the last two terms cancel each other. We are then left with just

$$\Lambda(\mathbf{k},\mathbf{q}) = P_{lr}(\mathbf{k})\hat{q}_l\hat{q}_rP_{ms}(\mathbf{k})\hat{\tilde{q}}_m\hat{\tilde{q}}_s \tag{5.19}$$

$$= \left[1-(\hat{\mathbf{k}}\cdot\hat{\mathbf{q}})^2\right]\left[\hat{\tilde{\mathbf{q}}}\cdot\hat{\tilde{\mathbf{q}}} - (\hat{\mathbf{k}}\cdot\hat{\tilde{\mathbf{q}}})^2\right], \tag{5.20}$$

where Eq. (1.35) for the transverse projector was used. Writing out each of the terms in the brackets as

$$\mu \equiv \hat{\mathbf{k}} \cdot \hat{\mathbf{q}} \tag{5.21}$$

$$\hat{\tilde{\mathbf{q}}} \cdot \hat{\tilde{\mathbf{q}}} = \widehat{\mathbf{q}-\mathbf{k}} \cdot \widehat{\mathbf{q}-\mathbf{k}} = \frac{(\mathbf{q}-\mathbf{k})^2}{|\mathbf{q}-\mathbf{k}|^2} = \frac{1}{\tilde{q}^2}\left(q^2 - 2kq\mu + k^2\right) \tag{5.22}$$

$$(\hat{\mathbf{k}} \cdot \hat{\tilde{\mathbf{q}}})^2 = \left[\frac{\mathbf{k}\cdot(\mathbf{q}-\mathbf{k})}{k\tilde{q}}\right]^2 = \frac{1}{\tilde{q}^2}(q\mu - k)^2 = \frac{1}{\tilde{q}^2}(q^2\mu^2 - 2qk\mu + k^2) \tag{5.23}$$

gives after simplification the result

$$\Lambda(\mathbf{k},\mathbf{q}) = (1-\mu^2)^2\frac{q^2}{\tilde{q}^2}\,. \tag{5.24}$$

Now comparing Eq. (5.14) with Eq. (1.78) gives us the shear stress UETC function as

$$U_\Pi(k,\eta_1,\eta_2) = \int \frac{d^3q}{(2\pi)^3}(1-\mu^2)^2\frac{q^2}{\tilde{q}^2}G(q,\eta_1,\eta_2)G(\tilde{q},\eta_1,\eta_2)\,. \tag{5.25}$$

The next step is to define the time dependence of the UETC through the function $G(q,\eta_1,\eta_2)$. In the studies of GW production from turbulence, it is customary to assume the turbulence to be stationary. In such a case the function G becomes

$$G(q,\eta_1,\eta_2) = 2P(q)D(q,\eta_1-\eta_2)\,, \tag{5.26}$$

where $P(q)$ is the velocity spectral density defined in Eq. (3.78), and D is a decoherence function whose time dependence is only through the time difference $\eta_1-\eta_2$ because of the stationarity. The decoherence function has been determined for acoustic waves and non-relativistic velocities in the SSM in Ref. [231] using linearized wave equations for the fluid variables, yielding

$$D(q,\eta_1-\eta_2) \simeq \cos\left[c_s q(\eta_1-\eta_2)\right] \tag{5.27}$$

in the high frequency limit. We also adopt this result here for acoustic turbulence. However, we are interested in a case where the turbulence is decaying and therefore the spectral density $P(q)$ should also be dependent on time, meaning that Eq. (5.26) needs to be generalized. We have opted for a locally stationary function where the time dependence of the spectral density is introduced through a geometric mean of two spectral densities evaluated at different times as

$$G(q,\eta_1,\eta_2) = 2\sqrt{P(q,\eta_1)P(q,\eta_2)}\cos\left[c_s q(\eta_1-\eta_2)\right]\,. \tag{5.28}$$

A similar approximation has been used, for example, in Refs. [279, 280], and the result reduces to Eq. (5.26) in the non-decaying limit where the spectral density loses its time dependence.

5.2 Gravitational wave power spectrum

The result in Eq. (5.25) with Eq. (5.28) defines the shear stress UETC for acoustic waves. Substituting it to the result for the GW spectrum in Eq. (5.6) allows us to write

$$\mathcal{P}_{\rm GW}(k) = \frac{6(1+c_s^2)^2}{\pi^2} k^3 \int \frac{d^3q}{(2\pi)^3}(1-\mu^2)^2 \frac{q^2}{\tilde{q}^2} \int_{\eta_i}^{\eta_f} d\eta_1 \int_{\eta_i}^{\eta_f} d\eta_2 \times \sqrt{P(q,\eta_1)P(\tilde{q},\eta_1)P(q,\eta_2)P(\tilde{q},\eta_2)}\,\Delta(\eta_1,\eta_2,k,q,\tilde{q})\,, \quad (5.29)$$

where we have defined a time-dependent kernel function

$$\Delta(\eta_1,\eta_2,k,q,\tilde{q}) = \frac{1}{2}\sigma(\eta_1,\eta_2)\cos\left[k(\eta_1-\eta_2)\right]\cos\left[c_s q(\eta_1-\eta_2)\right]\cos\left[c_s\tilde{q}(\eta_1-\eta_2)\right] \quad (5.30)$$

$$= \frac{1}{8}\sigma(\eta_1,\eta_2)\sum_{\pm\pm}\cos\left[\omega_{\pm\pm}(\eta_1-\eta_2)\right]\,, \quad (5.31)$$

where the product of cosines has been decomposed into a sum of cosines with

$$\omega_{\pm\pm} = k \pm c_s q \pm c_s\tilde{q}\,, \quad (5.32)$$

so that the sum runs over all possible sign combinations. Now using the definition for μ we can write

$$\mu = \hat{\mathbf{k}}\cdot\hat{\mathbf{q}} = \frac{\mathbf{k}\cdot\mathbf{q}}{kq} = \cos\theta\,, \quad (5.33)$$

where θ is the angle between the two wavevectors k and q. This means that after moving to spherical coordinates we can parametrize the angular part of the q-integral in terms of μ, yielding

$$\int d^3q \longrightarrow 2\pi\int_0^\infty q^2 dq \int_{-1}^{1} d\mu\,. \quad (5.34)$$

We can now conduct a change of variables $\mu \rightarrow \tilde{q}$ in the integral, which is useful because the integrand is expressed in terms of it. To this end, from the definition $\tilde{\mathbf{q}} = \mathbf{q} - \mathbf{k}$ it follows that

$$\mathbf{k}\cdot\mathbf{q} = \frac{1}{2}(q^2 + k^2 - \tilde{q}^2) \quad (5.35)$$

that with Eq. (5.33) gives the relation between μ and $\tilde{q}$ as

$$\mu = \frac{q^2 + k^2 - \tilde{q}^2}{2kq}\,. \quad (5.36)$$

Using this, the change of variables is straightforward and one obtains

$$\int d^3q \longrightarrow \frac{2\pi}{k}\int_0^\infty q\,dq \int_{|q-k|}^{q+k} \tilde{q}\,d\tilde{q}\,. \quad (5.37)$$

In the papers we have additionally written the expression for the GW spectrum in terms of the energy spectrum $E(k)$. However, Papers I and II, and III use different normalization for the spectrum,

where in the case of the former two, Eq. (3.79) contains a factor of $1/2$ on the LHS. To take into account both cases, we introduce a parameter n so that from Eq. (3.80) one obtains

$$P(k,\eta_1) = \frac{2n\pi^2}{k^2} E(k,\eta_1)\,, \tag{5.38}$$

where $n = 2$ when the factor of one half is included, and $n = 1$ when it is not. Also, in order to simplify the expression for the time integrals and to get rid of the square roots, we have approximated

$$\sqrt{E(q,\eta_1)E(\tilde{q},\eta_1)E(q,\eta_2)E(\tilde{q},\eta_2)} \approx E(q,\eta_1)E(\tilde{q},\eta_2) \tag{5.39}$$

in the integrand, which is a reasonable approximation for the integrals in Eq. (5.37) when the energy spectrum has a broken power law shape. We have also verified the approximation with numerical integration, and it does not have a noticeable effect on the shape or the amplitude of the GW power spectrum. Putting all of this together, the spectrum can be written as an expression containing four integrals as

$$\mathcal{P}_{\mathrm{GW}}(k) = \mathcal{P}_0 \int_0^\infty dq \int_{|q-k|}^{q+k} d\tilde{q}\, \rho(k,q,\tilde{q}) \int_{\eta_i}^{\eta_f} d\eta_1 \int_{\eta_i}^{\eta_f} d\eta_2\, E(q,\eta_1)E(\tilde{q},\eta_2)\Delta(\eta_1,\eta_2,k,q,\tilde{q})\,, \tag{5.40}$$

where

$$\mathcal{P}_0 = 6n^2(1+c_s^2)^2 \tag{5.41}$$

and

$$\rho(k,q,\tilde{q}) = \frac{\left[4k^2q^2 - (q^2+k^2-\tilde{q}^2)^2\right]^2}{16q^3\tilde{q}^3k^2}\,. \tag{5.42}$$

5.3 Shape of the spectrum – stationary turbulence

In the non-decaying case assuming exact radiation domination, the gravitational wave power spectrum from linear sound waves is approximated by the Sound Shell Model [231]. The model assumes that the phase transition completes in much less than a Hubble time $H_\star^{-1}$ so that the expansion of the universe can be neglected. This makes the model valid only for transitions for which the mean bubble separation $R_\star$ is much less than the Hubble time at the time of the transition. For a kinetic energy spectrum that goes as k^4 at low wavenumbers the model predicts a broken power law GW power spectrum that has a very steep k^9 power law before the peak, and a k^{-3} power law beyond it. The steep low-k power law had not been seen in numerical simulations studying the sound wave contribution.

One of the main objectives when we started working on Paper II was to confirm the existence of the steep k^9 power law predicted by the SSM. We also corrected an oversight in the SSM calculation where in the calculation of the time integrals over the growth rate of the kernel function Δ of Eq. (5.30) an asymptotic limit $t \to \infty$ was taken. This makes the result a sum of delta functions and extends the low-k power law all the way to $k = 0$, concealing the true low wavenumber behaviour of the spectrum, including the k^3 range required by causality. Another research group, independent of us and unaware of our work (and vice versa), was simultaneously studying the same subject, their

results in Ref. [281] sharing many features with our findings in Paper II. The e-prints of both papers were made public on the same day.

In the stationary case, the time dependence of the energy spectrum vanishes. Then all time dependence lies in the kernel function Δ, and assuming a broken power law form for the energy spectrum with power laws of k^4 and k^{-2}, as appropriate for shocks, it can be written as

$$E(k) = \frac{3}{2\pi}\frac{\bar{v}^2}{k_p}\frac{(k/k_p)^4}{1+(k/k_p)^6} \equiv \frac{3}{2\pi}\frac{\bar{v}^2}{k_p}\tilde{E}(k)\,, \tag{5.43}$$

where $\tilde{E}(k)$ is the spectral shape function, and the prefactor is fixed so that the condition $\left\langle \mathbf{v}^2 \right\rangle /2 = \int E(k)dk$ is fulfilled. The spectrum in Eq. (5.40) then reduces to

$$\mathcal{P}_{\rm GW}(k) = \mathcal{P}_0 \int_0^\infty dq \int_{|q-k|}^{q+k} d\tilde{q}\, \rho(k,q,\tilde{q})\tilde{E}(q)\tilde{E}(\tilde{q})\Delta(k,q,\tilde{q})\,, \tag{5.44}$$

with

$$\mathcal{P}_0 = \frac{54(1+c_s^2)^2}{\pi^2}\left(\frac{\bar{v}^2}{k_p}\right)^2 \tag{5.45}$$

and

$$\Delta(k,q,\tilde{q}) = \frac{1}{8}\sum_{\pm\pm}\int_{\eta_i}^{\eta_f} d\eta_1 \int_{\eta_i}^{\eta_f} d\eta_2\, \sigma(\eta_1,\eta_2)\cos\left[\omega_{\pm\pm}(\eta_1-\eta_2)\right] \tag{5.46}$$

corresponding to Eqs. (2.12)–(2.16) of Paper II. Note that the spectrum here is computed at the time the source switches off at η_f unlike in Paper II where the amplitude is that of the present day, thereby differing by the factor in Eq. (1.68). The kernel function Δ can be computed analytically both in the non-expanding and expanding cases. In the former, one obtains

$$\Delta_M(k,q,\tilde{q}) = \frac{1}{8}\sum_{\pm\pm}\left\{\left[\int_{t_i}^{t_f} dt_1\, \cos\left(\omega_{\pm\pm}t_1\right)\right]^2 + \left[\int_{t_i}^{t_f} dt_1\, \sin\left(\omega_{\pm\pm}t_1\right)\right]^2\right\} \tag{5.47}$$

$$= \frac{1}{2}\sum_{\pm\pm}\left(\frac{\sin\left[\omega_{\pm\pm}(t_f-t_i)/2\right]}{\omega_{\pm\pm}}\right)^2\,, \tag{5.48}$$

and in the latter

$$\Delta_{\rm exp}(k,q,\tilde{q}) = \frac{1}{8}\sum_{\pm\pm}\left\{\left[\int_{\eta_i}^{\eta_f} d\eta_1\, \frac{\cos\left(\omega_{\pm\pm}\eta_1\right)}{\eta_1}\right]^2 + \left[\int_{\eta_i}^{\eta_f} d\eta_1\, \frac{\sin\left(\omega_{\pm\pm}\eta_1\right)}{\eta_1}\right]^2\right\} \tag{5.49}$$

$$= \frac{1}{8}\sum_{\pm\pm}\left\{\left[{\rm Ci}(\omega_{\pm\pm}\eta_f) - {\rm Ci}(\omega_{\pm\pm}\eta_i)\right]^2 + \left[{\rm Si}(\omega_{\pm\pm}\eta_f) - {\rm Si}(\omega_{\pm\pm}\eta_i)\right]^2\right\}\,, \tag{5.50}$$

where Ci and Si are the sine and cosine integral functions respectively. In both cases the kernel consists of four terms with different combination of signs in $\omega_{\pm\pm}$ of Eq. (5.32). To inspect the contribution from each of these terms, we have separated the GW spectrum into components as

$$\mathcal{P}_{\rm gw} = \mathcal{P}_{++} + \mathcal{P}_{+-} + \mathcal{P}_{-+} + \mathcal{P}_{--}\,. \tag{5.51}$$

The evaluation of the spectrum now becomes that of computing the q and $\tilde{q}$ integrals, which can be done numerically. We have used the `NIntegrate` routine in Mathematica with the adaptive Monte Carlo method to perform the integration with $\eta_i = 1$ and a cutoff in the q-integral at $10k_p$, which is large enough that the results coincide with those from using the infinite upper limit in the observed wavenumber range.

Starting with the non-expanding case ($t_s \ll H_\star^{-1}$), the components in Eq. (5.51) have been plotted in Figure 7 of Paper II for $t_f = 5$. The contribution from the $\mathcal{P}_{++}$ component is tiny compared to the other components at all wavenumbers, so it does not contribute to the overall spectrum in a meaningful way. The steep k^9 power law follows from the $\mathcal{P}_{--}$ component that dominates at high wavenumbers. In Ref [231] it was the only term considered because it is the only one that does not vanish when the $t \to \infty$ limit that was used in the derivation of the spectrum is taken. At some lower wavenumber, that depends on the source lifetime t_f, the $\mathcal{P}_{+-}$ and $\mathcal{P}_{-+}$ components, both of which are equal due to symmetries in the integral, become dominant and start dictating the shape of the spectrum. They induce a linearly increasing regime into the overall spectrum at intermediate wavenumbers below the steep power law range, and give the causal k^3 scaling at low wavenumbers. The shift from the linear scaling to the steep power law results in a sharp peak for the spectrum that is only seen in the longitudinal case. The overall GW power spectrum with a peak wavenumber $k_p = 30$ in the non-expanding case has been plotted in Figure 1 of Paper II for various t_f. Due to the stationarity, there is a constant energy injection to the fluid at a length scale corresponding to the peak wavenumber k_p that leads to a linear increase in the peak amplitude of the GW spectrum over time. However, the amplitude of the spectrum does not change in the linear scaling region, leading to an extension in the k^9 power law range so that the point at which the spectrum turns over between the two power laws moves towards lower wavenumbers with a speed proportional to $t^{1/8}$. At early times the linearly scaling region develops gradually with a saturation timescale that is inversely proportional to the wavenumber as $t_k = 2\pi/k$ (see Appendix B and Fig. 8). Since the k^3 range can be associated with super-horizon scales, the point at which it turns into the linear range corresponds to the horizon wavenumber. It moves towards lower wavenumbers as $1/t$, causing the linearly increasing region to lengthen over time. At high wavenumbers past the peak the GW power spectrum goes as k^{-3}. For an analytical derivation of the k^3, k, k^9, and k^{-3} power law ranges in the overall spectrum, see Ref. [282]

If the timescale of the acoustic phase t_s is comparable to the Hubble time, the expansion of the universe can no longer be neglected. The additional suppression of the GW signal caused by the expansion sets an effective duration for the acoustic source. This causes the spectrum to saturate after the source has been suppressed enough so that it no longer leads to a noticeable increase in the amplitude of the spectrum. The GW power spectrum in the expanding universe case has been plotted for various η_f in Fig. 5 for $k_p = 10$ and in Fig. 6 for $k_p = 30$. In both cases the spectrum has saturated after $\eta_f \approx 5$, and while the k^3, k, and k^{-3} power law ranges can still be seen in the spectrum, the sharp power law below the peak has saturated into a shallower one. The value of the power law index depends on the amount of effective evolution the fluid goes through during the time the source remains active. As k_p, which can be related to the integral length scale L through Eq. (4.32), increases, the flow timescale t_s decreases, meaning that for a fixed η_f the fluid goes through more

evolution as k_p increases ($t_s \ll \eta_f$). The effect this has on the power law index is seen in Table 2 where the spectral index has been obtained by fitting to the wavenumber range from $0.5k_p$ to $0.9k_p$. As k_p increases, we approach the non-expanding $t_s \ll H_\star^{-1}$ limit, and therefore the steep k^9 result for the peak power law.

We have also conducted numerical simulations to study the GW power spectrum using the Pencil Code [248, 266] in Paper II. The code computes the shear stresses and solves the GW equation numerically so that GW power spectra can be obtained directly from the hydrodynamic simulations, which is a feature that has not been implemented into the Python code described in section 3.4. We have simulated random synthesized sound waves in the non-expanding case by initializing a random irrotational velocity field in Fourier space as

$$\tilde{\mathbf{v}}(\mathbf{k}, \eta) = i\mathbf{k}\tilde{\phi}(\mathbf{k}) \cos(c_s k \eta) \,, \tag{5.52}$$

where the velocity scalar potential $\tilde{\phi}$ is constructed so that the energy spectrum is a broken power law that goes as k^4 at low wavenumbers and has a k^{-2} inertial range. The potential is also given random phases to create random initial conditions. The energy and GW power spectra obtained numerically from the simulations have been plotted in Fig. 3 against the previously obtained semi-analytical results from numerically integrating Eq. (5.44) in the non-expanding case. The results are in a very good agreement with each other and confirm the appearance of the steep k^9 power law. We have also used the Pencil Code to perform direct numerical simulations akin to those described in section 3.4 of this thesis. The runs contain both purely longitudinal and purely transverse initial conditions whose parameters are listed in Table 1 of Paper II. The GW power spectra arising from rotational and vortical runs with similar initial parameters have been plotted against each other in Fig. 4. The result shows that while the k^3 and the shallow power law ranges are present both in the irrotational and vortical cases, only irrotational runs display the presence of a sharp peak in the GW spectrum, which is similar to that predicted by the semianalytical approach (although the power law below the peak ends up being shallower than k^9 in these simulations). This acoustic peak could be an important characteristic of GWs produced by sound waves and acoustic turbulence.

5.4 Shape of the spectrum – decaying turbulence

The previous section discussed a stationary case where energy is being constantly injected into the system at some length scale. However, in reality the energy injection is cut off after the phase transition completes, and shocks develop after a single shock formation time t_s, leading to energy dissipation. In Papers I and III we have approximated the GW power spectrum resulting from decaying acoustic turbulence by using the properties found for its energy spectrum and decay in Chapter 4. Since we want to study the effects of the decay only, we work in the $t_s \ll H_\star^{-1}$ limit so that the expansion of the universe can be neglected. The calculation in Paper I is based on Ref. [231] where an asymptotic limit $t \to \infty$ was taken when computing the growth rate of the time-dependent kernel function Δ, which extends the k^9 power law to $k = 0$. In Paper III we applied the model for the decay to the corrected description of Paper II and Ref. [281], which makes the computation of Paper I obsolete. Therefore, in this section we focus only on the calculation in Paper III, where Eq. (5.40)

becomes

$$\frac{1}{(H_\star L_0)^2}\mathcal{P}_{\rm gw}(k,t_{H_\star}) = \mathcal{P}_0 \int_0^\infty dq \int_{|q-k|}^{q+k} d\tilde{q}\,\rho(k,q,\tilde{q}) \int_0^{t_{H_\star}} dt_1 \int_0^{t_{H_\star}} dt_2\, E(q,t_1)E(\tilde{q},t_2)\Delta(t_1,t_2,k,q,\tilde{q})\,, \tag{5.53}$$

where

$$\mathcal{P}_0 = \frac{6(1+c_s^2)^2}{L_0^2} \tag{5.54}$$

and

$$\Delta(t_1,t_2,k,q,\tilde{q}) = \frac{1}{8}\sum_{\pm\pm}\cos\left[\omega_{\pm\pm}(t_1-t_2)\right]\,. \tag{5.55}$$

Here we have fixed an error in Paper III where in $\mathcal{P}_0$ the wrong definition for the energy spectrum with $n = 2$ was used in Eq. (5.41), leading to a wrong prefactor (24 instead of 6). Also, because of the way the shear stresses decay and correlate in an expanding universe, the effective lifetime of the GW source is the Hubble time [223], which is why we have taken $t_f = t_{H_\star} \approx H_\star^{-1}$. The time dependence of the spectrum was extracted in Eq. (4.34) as

$$E(\kappa,t) = L(t)\mathcal{E}(t)\Psi(\kappa)\,, \quad \kappa = L(t)k\,, \tag{5.56}$$

where $\Psi(\kappa)$ is the spectral shape function of Eq. (4.52). Because the contribution to the GW power spectrum from small length scales is negligible, we ignore the dissipation scale here, and extend the inertial range power law so that $\Psi(\kappa)$ is given by

$$\Psi(\kappa) = \Psi_0 \frac{(\kappa/\kappa_p)^\beta}{1+(\kappa/\kappa_p)^{\beta+2}}\,, \tag{5.57}$$

which also gives the k^{-2} inertial range scaling associated with shocks. The parameters κ_p and Ψ_0 are given by Eqs. (4.32) and (4.36) respectively with $\alpha = \beta+2$. We approximate that the time evolutions of the kinetic energy and the integral length scale are given by their late time behaviours in Eqs. (4.81) and (4.82). The stationarity of the energy spectrum at low wavenumbers imposes the condition in Eq. (4.73) that can be used to write the expression for the power spectrum in terms of $L(t)$ only. The energy spectrum then becomes

$$E(k,t) = \Psi_0\mathcal{E}_0 L_0 \frac{\left[kL_0/\kappa_p\right]^\beta}{1+\left[kL(t)/\kappa_p\right]^{\beta+2}}\,. \tag{5.58}$$

Using this in Eq. (5.53), performing a change of variables into dimensionless variables x and y via $q = kx$, $\tilde{q} = ky$, and decomposing the cosines in Δ like when obtaining Eq. (5.47) gives

$$\frac{1}{(H_\star L_0)^2}\mathcal{P}_{\rm gw}(k,t_{H_\star}) = \frac{\mathcal{P}_0}{128}\left(\frac{\Psi_0\mathcal{E}_0 L_0^{\beta+1}}{\kappa_p^\beta}\right)^2 k^{2(\beta+1)} \int_0^\infty dx \int_{|x-1|}^{x+1} dy\,\tilde{\rho}(x,y)\Delta_{ML}(t_{H_\star},k,x,y)\,, \tag{5.59}$$

where the time integrals have the form

$$\Delta_{ML}(t_{H_\star},k,x,y)=\sum_{\pm\pm}\left[\int_0^{t_{H_\star}}dt_1\frac{\cos(w_{\pm\pm}kt_1)}{1+\left[xkL(t_1)/\kappa_p\right]^{\beta+2}}\int_0^{t_{H_\star}}dt_2\frac{\cos(w_{\pm\pm}kt_2)}{1+\left[ykL(t_2)/\kappa_p\right]^{\beta+2}}\right.$$
$$\left.+\int_0^{t_{H_\star}}dt_1\frac{\sin(w_{\pm\pm}kt_1)}{1+\left[xkL(t_1)/\kappa_p\right]^{\beta+2}}\int_0^{t_{H_\star}}dt_2\frac{\sin(w_{\pm\pm}kt_2)}{1+\left[ykL(t_2)/\kappa_p\right]^{\beta+2}}\right], \quad (5.60)$$

and we have rescaled

$$\tilde{\rho}(x,y)=(xy)^{\beta-3}\left[4x^2-\left(x^2+1-y^2\right)^2\right]^2 \quad (5.61)$$

and

$$w_{\pm\pm}=1\pm c_s x\pm c_s y\,. \quad (5.62)$$

Using the result for $L(t)$ in Eq. (4.82) makes it possible to write the time integrals as

$$\int_0^{t_{H_\star}}dt_1\frac{\cos(w_{\pm\pm}kt_1)}{1+\left[xkL(t_1)/\kappa_p\right]^{\beta+2}}=\int_0^{t_{H_\star}}dt_1\frac{\cos(w_{\pm\pm}kt_1)}{1+\left(\frac{xkL_0}{\kappa_p}\right)^{\beta+2}\left(1+C\frac{t_1}{t_s}\right)^{\gamma}}\,, \quad (5.63)$$

where we have denoted

$$\gamma\equiv\lambda(\beta+2)=\frac{2(\beta+2)}{\beta+3}\,. \quad (5.64)$$

The time integrals can be written in terms of a dimensionless variable $z=t/t_s$ that measures time in the number of shock formation times. After collecting and combining factors, the GW power spectrum can be written in a simplified form as

$$\frac{1}{(H_\star L_0)^2}\mathcal{P}_{\rm gw}(kL_0,t_{H_\star})=\widetilde{\mathcal{P}}_0\left(\frac{kL_0}{\kappa_p}\right)^{2(\beta+1)}\int_0^{\infty}dx\int_{|x-1|}^{x+1}dy\,\tilde{\rho}(x,y)\tilde{\Delta}(t_{H_\star},kL_0,x,y)\,, \quad (5.65)$$

with

$$\widetilde{\mathcal{P}}_0=\frac{3\left[(1+c_s^2)(\beta+2)\right]^2}{64\pi^2}\bar{v}_0^2\sin^2\left[\frac{\pi(\beta+1)}{\beta+2}\right], \quad (5.66)$$

and a time dependent kernel function of the form

$$\tilde{\Delta}(t_{H_\star},kL_0,x,y)=\sum_{\pm\pm}\left[\mathcal{I}_c(t_{H_\star},kL_0,x,w_{\pm\pm}(x,y))\mathcal{I}_c(t_{H_\star},kL_0,y,w_{\pm\pm}(x,y))\right.$$
$$\left.+\mathcal{I}_s(t_{H_\star},kL_0,x,w_{\pm\pm}(x,y))\mathcal{I}_s(t_{H_\star},kL_0,y,w_{\pm\pm}(x,y))\right], \quad (5.67)$$

where the time integral functions $\mathcal{I}_s$ and $\mathcal{I}_c$ have the expressions

$$\mathcal{I}_c(t_{H_\star},kL_0,\chi,w_{\pm\pm}(x,y))=\int_0^{z_\star}dz\frac{\cos\left(kL_0\frac{w_{\pm\pm}}{\bar{v}_0}z\right)}{1+\left(kL_0\frac{\chi}{\kappa_p}\right)^{\beta+2}(1+Cz)^{\gamma}} \quad (5.68)$$

$$\mathcal{I}_s(t_{H_\star},kL_0,\chi,w_{\pm\pm}(x,y))=\int_0^{z_\star}dz\frac{\sin\left(kL_0\frac{w_{\pm\pm}}{\bar{v}_0}z\right)}{1+\left(kL_0\frac{\chi}{\kappa_p}\right)^{\beta+2}(1+Cz)^{\gamma}}\,, \quad (5.69)$$

with $z_\star = t_{H_\star}/t_s$. The time integrals cannot be solved analytically in this case, so they also need to be computed numerically in addition to the x and y integrals in order to obtain the spectrum. The spectrum at a given wavenumber k can be evaluated after setting values for the GW source lifetime $z_\star$ (in the units of t_s), the decay constant C, the low-k power law of the energy spectrum β, and the initial rms velocity in the fluid $\bar{v}_0$. The expression for the GW spectrum reduces to the stationary case in the limit $C \to 0$ where the time dependence of the energy spectrum vanishes.

The numerical integration has been carried out by using the `integrate.quad` routine in SciPy [283] with parameter values $\beta = 4$, $\bar{v}_0 = 0.2$, and $C = 0.2$ that roughly correspond to values used and seen in our numerical simulations. The GW power spectrum for various source durations $z_\star$ has been plotted in Fig. 14 of Paper III along with the components of Eq. (5.51). Like in the previous section with the expansion included, the energy dissipation sets an effective duration for the GW source, causing the spectrum to saturate at late times. The saturated spectrum has been plotted in Fig. 15 alongside stationary spectra with $C = 0$ that correspond to the non-expanding case discussed in the previous section. While the causal k^3 power law at low wavenumbers and the k^{-3} power law at high wavenumbers are still present, the linear scaling region at intermediate wavenumbers is no longer clearly seen and only scales close to linear in a very narrow wavenumber band. The power law below the peak is also much shallower than k^9, but the acoustic peak characteristic to acoustic turbulence can still be clearly distinguished, albeit it being shorter than in the non-decaying case. In order to measure the peak power law index, we have made power law fits to the spectrum at various times in the wavenumber range $kL_0 \in [0.28, 0.45]$. The table also contains fits of the power law seen in the $\mathcal{P}_{--}$ component with a fitting range of $kL_0 \in [0.25, 0.35]$. The results display convergence in the power law indices for $L(t_{H_\star})/L_0 \gtrsim 4.0$ in such a way that the power law in $\mathcal{P}_{--}$ converges to k^5, and the $\mathcal{P}_{+-}$, $\mathcal{P}_{-+}$, and $\mathcal{P}_{++}$ components modify it so that the total spectrum converges to a power law of k^4. The figures also show that the saturation is slower at small wavenumbers. This is more quantitatively illustrated by Fig. 16 that plots the amplitude of the spectrum normalized to its value at $t = t_s/2$ as a function of time for various different wavenumbers that are also highlighted on the x-axis of Fig. 15. The wavenumbers around the peak are mostly converged for times $t/t_s \gtrsim 20$. At high wavenumbers past the peak the amplitude of the converged spectrum corresponds to that of the spectrum at $t = 2t_s$ in the non-decaying case. This curve has been highlighted by green in Fig. 15. This makes the effective lifetime of the decaying case about two times the timescale of the flow when compared to the stationary case. The spectral shape corresponding to the stationary case is also recovered for $C \neq 0$ when the flow does not change considerably in a Hubble time so that the dissipation does not have time to properly kick in before the source is diluted by the expansion. In other words, this occurs when the GW source duration is small compared to the flow timescale, i.e. $t_{H_\star} \ll t_s$. Since the model discussed here is only valid for transitions which complete in much less than the Hubble time, the mean bubble separation $R_\star$ must be much less than the Hubble length at the phase transition, yielding

$$\begin{aligned} r_\star &\equiv R_\star H_\star \\ &= \bar{v}_0 t_s H_\star \ll 1 \,. \end{aligned} \tag{5.70}$$

With this, the $t_{H_\star} \ll t_s$ regime then implies $\bar{v}_0 \ll r_\star$, meaning that the stationary case results of

the previous section are approximately recovered in the limit of small rms velocities. We have left a more careful study of the parameter space and generalizing the study of the expanding universe case as future work.

6. Summary

Gravitational waves (GWs) manifest as ripples in spacetime that propagate at the speed of light and interact extremely weakly with matter. They carry within them information on the processes that led to their generation and on the conditions that prevailed at the time. Due to their almost free propagation through cosmic history, they act as a promising probe of the very early universe that is beyond the reach of more conventional detection methods. Gravitational waves sourced in the very early universe are present today in a stochastic GW background. An important quantity that acts as a bridge between theory and experiments is the gravitational wave power spectrum. A huge global effort is currently under way in improving the existing gravitational wave observatories, and in designing and building the next generation of detectors.

As the universe cools down due to its expansion, it goes through various phase transitions. Many extensions to the Standard Model predict a first-order phase transition (FOPT) on the electroweak energy scale, which is well motivated by it providing one of the most promising mechanisms for baryogenesis. FOPTs would also provide a strong source of GWs, as they are violent events that proceed through nucleation, expansion, and collision of bubbles that act as boundaries between the old and new phases. This makes them a candidate for detection with future gravitational wave detectors. A FOPT leads to many individual GW sources. For a wide range of models, the dominant contribution is believed to come from sound waves that can be present in the radiation fluid of the early universe long after the phase transition itself has completed. Because of the small kinematic viscosity in the early universe, resulting in a high Reynolds number and therefore strong non-linearities, the sound waves are expected to steepen into shock waves in a timescale $t_s = R_\star/\bar{v}$ where $R_\star$ is the mean bubble separation in the transition and $\bar{v}$ the rms velocity of the fluid. This non-linear regime is known as acoustic turbulence, and it is associated with strong dissipation of energy by the viscosity. The decay of the acoustic phase and the acoustic turbulence that follows are important factors in determining the intensity of the GW signal and, consequently, its detectability in future GW experiments.

In the papers featured in this thesis we have studied acoustic turbulence and the GW generation from it using numerical simulations and seminanalytical methods based on earlier literature on sound waves, like the Sound Shell Model. The relativistic fluid equations are expanded to second order in the limit of non-relativistic fluid bulk velocities and an ultrarelativistic equation of state in order to obtain a set of equations that describe a radiation fluid in the weak phase transition limit. We find an additional term in the continuity equation that has been missing from earlier literature working in a similar limit. In Papers I and III, we have simulated fluids in two and three dimensions respectively in the non-linear regime using a highly optimized self-written Python code, and com-

pared the results to the properties known for classical acoustic turbulence. Instead of simulating the phase transition itself, to study the evolution of the flow over many t_s, we have generated random initial conditions that form a random field of shocks similar to what would be expected after a FOPT.

The shape of an individual shock wave can be solved from the fluid equations in a low velocity limit. The shock profile obtains a tanh shape that with its propagation speed agrees very well with shock tube simulations. Like in the fully classical case, the energy spectrum in our simulations obtains a universal shape after acoustic turbulence develops, that at length scales above the dissipation scale follows a broken power law form. The inertial range power law is found to be close but a bit steeper than the classical k^{-2} KP spectrum with an approach towards it with an increasing Reynolds number. Evidence obtained by fitting for the low-k power law points to a k^4 scaling in 3D and a $k^{2.5}$ scaling in 2D. We come up with a universal shape for the decaying energy spectrum that extracts its time dependence, associating the change in the shape of the spectrum in the dissipation range with the flattening of shocks over time. We use the tanh profile of individual shocks to write the energy spectrum as a broken power law modulated by a function that depends on the shock width, and confirm its validity with fits to simulation data.

The decay of the fluid kinetic energy in the simulations displays a power law form at late times ($t > 10t_s$). We study the energy dissipation equation for acoustic turbulence and find that in this late time regime the mean dissipation rate is set by the viscous dissipation. We then calculate the time evolution functions for the kinetic energy and the integral length scale analytically using the previously found universal shape for the spectrum with the k^{-2} inertial range behaviour associated with shocks, and the stationarity of the energy spectrum at low wavenumbers. The obtained functions give the power law indices at late times in terms of the low-k power law in the energy spectrum, which we find to be in a good agreement with simulation data.

In Paper II we study the gravitational wave power spectrum resulting from acoustic turbulence in the stationary case. Our approach is based on the Sound Shell Model, and we confirm its prediction of a steep k^9 power law scaling below the peak of the GW power spectrum by a numerical simulation containing synthesized sound waves. We also correct an oversight with the calculation that caused the k^9 range to mask the true behaviour of the spectrum at low wavenumbers. We find by numerical integration of the spectrum that the steep scaling ends up being less prominent in practice, appearing only on a limited range below the peak, with its length depending on the lifetime of the flow. At wavenumbers smaller than this, the spectrum turns over into a shallow linear growth, and a k^3 scaling required by causality is obtained at small wavenumbers. If the timescale of the flow is comparable to the Hubble time, the expansion of the universe suppresses the GW source, imposing an effective cutoff to the GW generation and causing the spectrum to saturate. This saturation suppresses the generation of the steep power law, making it shallower. The steep result is recovered in the limit where the flow is long-lived in comparison to the Hubble time, corresponding to the case where the expansion can be neglected. The change from the linear power law range into the steeper one below the peak leads to an appearance of a sharp peak in the GW power spectrum that we have confirmed by numerical simulations to be only present in the irrotational case. This acoustic peak could be an important characteristic of GWs produced by sound waves and acoustic turbulence.

In Paper III we study the effects of dissipation on the GW power spectrum produced by decaying acoustic turbulence based on the corrected description found in Paper II. We apply the properties found for the energy spectrum, and the model for the decay in the limit where the expansion of the universe can be neglected, and numerically integrate the GW spectrum. The peak power law is found to be shallower than the steep k^9, converging to k^4 with our choice of parameters in a time where the integral length scale has grown to be three times the initial one. The linearly growing intermediate power law is also greatly suppressed, scaling only close to linear in a narrow wavenumber band. The decay also leads to a saturation in the amplitude of the spectrum that at high wavenumbers corresponds to an effective lifetime of $2t_s$ when compared to the stationary case, which is approximately recovered in the low rms velocity or slow decay limit. The acoustic peak can still be clearly distinguished in the saturated result.

Bibliography

[1] J. Dahl, M. Hindmarsh, K. Rummukainen and D.J. Weir, *Decay of acoustic turbulence in two dimensions and implications for cosmological gravitational waves*, *Phys. Rev. D* **106** (2022) 063511 [2112.12013].

[2] R. Sharma, J. Dahl, A. Brandenburg and M. Hindmarsh, *Shallow relic gravitational wave spectrum with acoustic peak*, *JCAP* **12** (2023) 042 [2308.12916].

[3] J. Dahl, M. Hindmarsh, K. Rummukainen and D.J. Weir, *Primordial acoustic turbulence: Three-dimensional simulations and gravitational wave predictions*, *Phys. Rev. D* **110** (2024) 103512 [2407.05826].

[4] B. Ryden, *Introduction to Cosmology*, Cambridge University Press, 2 ed. (2016).

[5] M. Maggiore, *Gravitational Waves. Vol. 1: Theory and Experiments*, Oxford University Press (2007), 10.1093/acprof:oso/9780198570745.001.0001.

[6] LIGO Scientific, Virgo collaboration, *Observation of Gravitational Waves from a Binary Black Hole Merger*, *Phys. Rev. Lett.* **116** (2016) 061102 [1602.03837].

[7] LIGO Scientific, Virgo collaboration, *GWTC-1: A Gravitational-Wave Transient Catalog of Compact Binary Mergers Observed by LIGO and Virgo during the First and Second Observing Runs*, *Phys. Rev. X* **9** (2019) 031040 [1811.12907].

[8] KAGRA, VIRGO, LIGO Scientific collaboration, *Open Data from the Third Observing Run of LIGO, Virgo, KAGRA, and GEO*, *Astrophys. J. Suppl.* **267** (2023) 29 [2302.03676].

[9] A.R. Liddle and D.H. Lyth, *Cosmological Inflation and Large-Scale Structure*, Cambridge University Press (2000).

[10] V.F. Mukhanov, H.A. Feldman and R.H. Brandenberger, *Theory of cosmological perturbations*, **215** (1992) 203.

[11] A. Liddle, *An Introduction to Modern Cosmology*, Wiley (2015).

[12] S.M. Carroll, *Spacetime and Geometry: An Introduction to General Relativity*, Cambridge University Press (7, 2019), 10.1017/9781108770385.

[13] Planck collaboration, *Planck 2018 results. VI. Cosmological parameters*, *Astron. Astrophys.* **641** (2020) A6 [1807.06209].

[14] H. Kodama and M. Sasaki, *Cosmological Perturbation Theory*, *Prog. Theor. Phys. Suppl.* **78** (1984) 1.

[15] L. Amendola and S. Tsujikawa, *Dark Energy: Theory and Observations*, Cambridge University Press (1, 2015).

[16] V.A. Rubakov and D.S. Gorbunov, *Introduction to the Theory of the Early Universe: Hot big bang theory*, World Scientific, Singapore (2017), 10.1142/10447.

[17] M. Maggiore, *Gravitational Waves. Vol. 2: Astrophysics and Cosmology*, Oxford University Press (3, 2018).

[18] H. Kurki-Suonio, "Cosmological perturbation theory 1." https://www.mv.helsinki.fi/home/hkurkisu/cpt/CosPer.pdf, March, 2024.

[19] J.M. Bardeen, *Gauge Invariant Cosmological Perturbations*, *Phys. Rev. D* **22** (1980) 1882.

[20] S. Weinberg, *Gravitation and Cosmology: Principles and Applications of the General Theory of Relativity*, Wiley, New York, (1972).

[21] C.W. Misner, K.S. Thorne and J.A. Wheeler, *Gravitation*, W. H. Freeman, San Francisco (1973).

[22] M. Maggiore, *Gravitational wave experiments and early universe cosmology*, *Phys. Rept.* **331** (2000) 283 [gr-qc/9909001].

[23] M. Isi, *Parametrizing gravitational-wave polarizations*, *Class. Quant. Grav.* **40** (2023) 203001 [2208.03372].

[24] J.D. Romano and N.J. Cornish, *Detection methods for stochastic gravitational-wave backgrounds: a unified treatment*, *Living Rev. Rel.* **20** (2017) 2 [1608.06889].

[25] C. Caprini and D.G. Figueroa, *Cosmological Backgrounds of Gravitational Waves*, *Class. Quant. Grav.* **35** (2018) 163001 [1801.04268].

[26] B. Allen, *The Stochastic gravity wave background: Sources and detection*, in *Les Houches School of Physics: Astrophysical Sources of Gravitational Radiation*, pp. 373–417, 4, 1996 [gr-qc/9604033].

[27] R.A. Isaacson, *Gravitational Radiation in the Limit of High Frequency. I. The Linear Approximation and Geometrical Optics*, *Phys. Rev.* **166** (1968) 1263.

[28] R.A. Isaacson, *Gravitational Radiation in the Limit of High Frequency. II. Nonlinear Terms and the Ef fective Stress Tensor*, *Phys. Rev.* **166** (1968) 1272.

[29] E.E. Flanagan and S.A. Hughes, *The Basics of gravitational wave theory*, *New J. Phys.* **7** (2005) 204 [gr-qc/0501041].

[30] N. Andersson, *Gravitational waves from instabilities in relativistic stars*, *Class. Quant. Grav.* **20** (2003) R105 [astro-ph/0211057].

[31] B. Mueller, H.-T. Janka and A. Marek, *A New Multi-Dimensional General Relativistic Neutrino Hydrodynamics Code of Core-Collapse Supernovae III. Gravitational Wave Signals from Supernova Explosion Models*, *Astrophys. J.* **766** (2013) 43 [1210.6984].

[32] K. Kotake, K. Sato and K. Takahashi, *Explosion mechanism, neutrino burst, and gravitational wave in core-collapse supernovae*, *Rept. Prog. Phys.* **69** (2006) 971 [astro-ph/0509456].

[33] J.M. Lattimer, *The nuclear equation of state and neutron star masses*, *Ann. Rev. Nucl. Part. Sci.* **62** (2012) 485 [1305.3510].

[34] N. Chamel and P. Haensel, *Physics of Neutron Star Crusts*, *Living Rev. Rel.* **11** (2008) 10 [0812.3955].

[35] N. Andersson, V. Ferrari, D.I. Jones, K.D. Kokkotas, B. Krishnan, J.S. Read et al., *Gravitational waves from neutron stars: Promises and challenges*, *Gen. Rel. Grav.* **43** (2011) 409 [0912.0384].

[36] K. Belczynski, V. Kalogera and T. Bulik, *A Comprehensive study of binary compact objects as gravitational wave sources: Evolutionary channels, rates, and physical properties*, *Astrophys. J.* **572** (2001) 407 [astro-ph/0111452].

[37] M. Spera, A.A. Trani and M. Mencagli, *Compact Binary Coalescences: Astrophysical Processes and Lessons Learned*, *Galaxies* **10** (2022) 76 [2206.15392].

[38] J. Kormendy and L.C. Ho, *Coevolution (Or Not) of Supermassive Black Holes and Host Galaxies*, *Ann. Rev. Astron. Astrophys.* **51** (2013) 511 [1304.7762].

[39] P. Amaro-Seoane, J.R. Gair, M. Freitag, M. Coleman Miller, I. Mandel, C.J. Cutler et al., *Astrophysics, detection and science applications of intermediate- and extreme mass-ratio inspirals*, *Class. Quant. Grav.* **24** (2007) R113 [astro-ph/0703495].

[40] M. Dotti, A. Sesana and R. Decarli, *Massive black hole binaries: dynamical evolution and observational signatures*, *Adv. Astron.* **2012** (2012) 940568 [1111.0664].

[41] V.F. Mukhanov and G.V. Chibisov, *Quantum Fluctuations and a Nonsingular Universe*, *JETP Lett.* **33** (1981) 532.

[42] J.B. Hartle, *Gravity: An Introduction to Einstein's General Relativity*, Benjamin Cummings, illustrate ed. (Jan., 2003).

[43] M.C. Guzzetti, N. Bartolo, M. Liguori and S. Matarrese, *Gravitational waves from inflation*, *Riv. Nuovo Cim.* **39** (2016) 399 [1605.01615].

[44] S.Y. Khlebnikov and I.I. Tkachev, *Classical decay of inflaton*, *Phys. Rev. Lett.* **77** (1996) 219 [hep-ph/9603378].

[45] A. Vilenkin and E.P.S. Shellard, *Cosmic Strings and Other Topological Defects*, Cambridge University Press (7, 2000).

[46] M.B. Hindmarsh and T.W.B. Kibble, *Cosmic strings*, *Rept. Prog. Phys.* **58** (1995) 477 [hep-ph/9411342].

[47] T.W.B. Kibble, *Topology of Cosmic Domains and Strings*, *J. Phys. A* **9** (1976) 1387.

[48] D.G. Figueroa, M. Hindmarsh and J. Urrestilla, *Exact Scale-Invariant Background of Gravitational Waves from Cosmic Defects*, *Phys. Rev. Lett.* **110** (2013) 101302 [1212.5458].

[49] LIGO Scientific, Virgo collaboration, *Properties of the Binary Black Hole Merger GW150914*, *Phys. Rev. Lett.* **116** (2016) 241102 [1602.03840].

[50] LIGO Scientific, Virgo collaboration, *GW170817: Observation of Gravitational Waves from a Binary Neutron Star Inspiral*, *Phys. Rev. Lett.* **119** (2017) 161101 [1710.05832].

[51] B.P. Abbott et al., *Multi-messenger Observations of a Binary Neutron Star Merger*, *Astrophys. J. Lett.* **848** (2017) L12 [1710.05833].

[52] I. Bartos and M. Kowalski, *Multimessenger Astronomy*, 2399-2891, IOP Publishing (2017), 10.1088/978-0-7503-1369-8.

[53] LIGO Scientific, Virgo, Fermi-GBM, INTEGRAL collaboration, *Gravitational Waves and Gamma-rays from a Binary Neutron Star Merger: GW170817 and GRB 170817A*, *Astrophys. J. Lett.* **848** (2017) L13 [1710.05834].

[54] E. Troja et al., *The X-ray counterpart to the gravitational wave event GW 170817*, *Nature* **551** (2017) 71 [1710.05433].

[55] D. Kasen, B. Metzger, J. Barnes, E. Quataert and E. Ramirez-Ruiz, *Origin of the heavy elements in binary neutron-star mergers from a gravitational wave event*, *Nature* **551** (2017) 80 [1710.05463].

[56] M.R. Drout et al., *Light Curves of the Neutron Star Merger GW170817/SSS17a: Implications for R-Process Nucleosynthesis*, *Science* **358** (2017) 1570 [1710.05443].

[57] D.A. Coulter et al., *Swope Supernova Survey 2017a (SSS17a), the Optical Counterpart to a Gravitational Wave Source*, *Science* **358** (2017) 1556 [1710.05452].

[58] P.S. Cowperthwaite et al., *The Electromagnetic Counterpart of the Binary Neutron Star Merger LIGO/Virgo GW170817. II. UV, Optical, and Near-infrared Light Curves and Comparison to Kilonova Models*, *Astrophys. J. Lett.* **848** (2017) L17 [1710.05840].

[59] LIGO Scientific, Virgo collaboration, *Tests of general relativity with GW150914*, *Phys. Rev. Lett.* **116** (2016) 221101 [1602.03841].

[60] V. Kalogera et al., *The Next Generation Global Gravitational Wave Observatory: The Science Book*, 2111.06990.

[61] S.J. Cooper, C.M. Mow-Lowry, D. Hoyland, J. Bryant, A. Ubhi, J. O'Dell et al., *Sensors and actuators for the advanced LIGO A+ upgrade*, *Rev. Sci. Instrum.* **94** (2023) 014502 [2208.00798].

[62] J. Sakstein, B. Jain, J.S. Heyl and L. Hui, *Tests of Gravity Theories Using Supermassive Black Holes*, *Astrophys. J. Lett.* **844** (2017) L14 [1704.02425].

[63] M. Bailes et al., *Gravitational-wave physics and astronomy in the 2020s and 2030s*, *Nature Rev. Phys.* **3** (2021) 344.

[64] C.M. Will, *The Confrontation between General Relativity and Experiment*, *Living Rev. Rel.* **17** (2014) 4 [1403.7377].

[65] E. Belgacem, Y. Dirian, S. Foffa and M. Maggiore, *Modified gravitational-wave propagation and standard sirens*, *Phys. Rev. D* **98** (2018) 023510 [1805.08731].

[66] M. Isi and A.J. Weinstein, *Probing gravitational wave polarizations with signals from compact binary coalescences*, 1710.03794.

[67] L. Baiotti, *Gravitational waves from neutron star mergers and their relation to the nuclear equation of state*, *Prog. Part. Nucl. Phys.* **109** (2019) 103714 [1907.08534].

[68] B.S. Sathyaprakash et al., *Extreme Gravity and Fundamental Physics*, 1903.09221.

[69] E. Annala, T. Gorda, A. Kurkela, J. Nättilä and A. Vuorinen, *Evidence for quark-matter cores in massive neutron stars*, *Nature Phys.* **16** (2020) 907 [1903.09121].

[70] E. Annala, T. Gorda, J. Hirvonen, O. Komoltsev, A. Kurkela, J. Nättilä et al., *Strongly interacting matter exhibits deconfined behavior in massive neutron stars*, *Nature Commun.* **14** (2023) 8451 [2303.11356].

[71] A. Bauswein, N.-U.F. Bastian, D.B. Blaschke, K. Chatziioannou, J.A. Clark, T. Fischer et al., *Identifying a first-order phase transition in neutron star mergers through gravitational waves*, *Phys. Rev. Lett.* **122** (2019) 061102 [1809.01116].

[72] K.K.Y. Ng, S. Vitale, W.M. Farr and C.L. Rodriguez, *Probing multiple populations of compact binaries with third-generation gravitational-wave detectors*, *Astrophys. J. Lett.* **913** (2021) L5 [2012.09876].

[73] S. Vitale, W.M. Farr, K. Ng and C.L. Rodriguez, *Measuring the star formation rate with gravitational waves from binary black holes*, *Astrophys. J. Lett.* **886** (2019) L1 [1808.00901].

[74] A. Lamberts, S. Blunt, T.B. Littenberg, S. Garrison-Kimmel, T. Kupfer and R.E. Sanderson, *Predicting the LISA white dwarf binary population in the Milky Way with cosmological simulations*, *Mon. Not. Roy. Astron. Soc.* **490** (2019) 5888 [1907.00014].

[75] F.K. Thielemann, M. Eichler, I.V. Panov and B. Wehmeyer, *Neutron Star Mergers and Nucleosynthesis of Heavy Elements*, *Ann. Rev. Nucl. Part. Sci.* **67** (2017) 253 [1710.02142].

[76] M. Enoki, K.T. Inoue, M. Nagashima and N. Sugiyama, *Gravitational waves from supermassive black hole coalescence in a hierarchical galaxy formation model*, *Astrophys. J.* **615** (2004) 19 [astro-ph/0404389].

[77] H. Padmanabhan and A. Loeb, *Unravelling the formation of the first supermassive black holes with the SKA pulsar timing array*, *Astron. Astrophys.* **676** (2023) A115 [2207.14309].

[78] S. Burke-Spolaor et al., *The Astrophysics of Nanohertz Gravitational Waves*, *Astron. Astrophys. Rev.* **27** (2019) 5 [1811.08826].

[79] M. Milosavljevic and D. Merritt, *The Final parsec problem*, *AIP Conf. Proc.* **686** (2003) 201 [astro-ph/0212270].

[80] Y.-C. Chen, H.-C. Hwang, Y. Shen, X. Liu, N.L. Zakamska, Q. Yang et al., *Varstrometry for Off-nucleus and Dual Subkiloparsec AGN (VODKA): Hubble Space Telescope Discovers Double Quasars*, *Astrophys. J.* **925** (2022) 162 [2108.01672].

[81] M. Milosavljevic, D. Merritt, A. Rest and F.C. van den Bosch, *Galaxy cores as relics of black hole mergers*, *Mon. Not. Roy. Astron. Soc.* **331** (2002) L51 [astro-ph/0110185].

[82] W.L. Freedman and B.F. Madore, *Progress in direct measurements of the Hubble constant*, *JCAP* **11** (2023) 050 [2309.05618].

[83] E. Di Valentino, O. Mena, S. Pan, L. Visinelli, W. Yang, A. Melchiorri et al., *In the realm of the Hubble tension—a review of solutions*, *Class. Quant. Grav.* **38** (2021) 153001 [2103.01183].

[84] S. Dhawan, M. Bulla, A. Goobar, A.S. Carracedo and C.N. Setzer, *Constraining the observer angle of the kilonova AT2017gfo associated with GW170817: Implications for the Hubble constant*, 1909.13810.

[85] S.M. Feeney, D.J. Mortlock and N. Dalmasso, *Clarifying the Hubble constant tension with a Bayesian hierarchical model of the local distance ladder*, *Mon. Not. Roy. Astron. Soc.* **476** (2018) 3861 [1707.00007].

[86] S.M. Feeney, H.V. Peiris, A.R. Williamson, S.M. Nissanke, D.J. Mortlock, J. Alsing et al., *Prospects for resolving the Hubble constant tension with standard sirens*, *Phys. Rev. Lett.* **122** (2019) 061105 [1802.03404].

[87] V. Cardoso and P. Pani, *Testing the nature of dark compact objects: a status report*, *Living Rev. Rel.* **22** (2019) 4 [1904.05363].

[88] S. Clesse and J. García-Bellido, *Detecting the gravitational wave background from primordial black hole dark matter*, *Phys. Dark Univ.* **18** (2017) 105 [1610.08479].

[89] B. Carr and F. Kuhnel, *Primordial Black Holes as Dark Matter: Recent Developments*, *Ann. Rev. Nucl. Part. Sci.* **70** (2020) 355 [2006.02838].

[90] B.S. Sathyaprakash, B.F. Schutz and C. Van Den Broeck, *Cosmography with the Einstein Telescope*, *Class. Quant. Grav.* **27** (2010) 215006 [0906.4151].

[91] K. Riles, *Gravitational Waves: Sources, Detectors and Searches*, *Prog. Part. Nucl. Phys.* **68** (2013) 1 [1209.0667].

[92] P.F. Michelson, *On detecting stochastic background gravitational radiation with terrestrial detectors*, *Monthly Notices of the Royal Astronomical Society* **227** (1987) 933.

[93] N. Christensen, *Measuring the stochastic gravitational radiation background with laser interferometric antennas*, *Phys. Rev. D* **46** (1992) 5250.

[94] A.J. Farmer and E.S. Phinney, *The gravitational wave background from cosmological compact binaries*, *Mon. Not. Roy. Astron. Soc.* **346** (2003) 1197 [astro-ph/0304393].

[95] D. Sivia and J. Skilling, *Data Analysis: A Bayesian Tutorial*, Oxford science publications, OUP Oxford (2006).

[96] C. Helstrom, *Statistical Theory of Signal Detection*, International series of monographs on electronics and instrumentation, Macmillan Company (1960).

[97] L.A. Wainstein and V.D. Zubakov, *Extraction of Signals from Noise*, Dover books on physics and mathematical physics, Prentice-Hall, Englewood Cliffs, NJ (1962).

[98] C.J. Hogan and P.L. Bender, *Estimating stochastic gravitational wave backgrounds with Sagnac calibration*, *Phys. Rev. D* **64** (2001) 062002 [astro-ph/0104266].

[99] M. Tinto, J.W. Armstrong and F.B. Estabrook, *Discriminating a gravitational wave background from instrumental noise in the LISA detector*, *Phys. Rev. D* **63** (2001) 021101.

[100] R. Durrer, *The Cosmic Microwave Background*, Cambridge University Press (2008).

[101] E.W. Kolb, *The Early Universe*, vol. 69, Taylor and Francis (5, 2019), 10.1201/9780429492860.

[102] Particle Data Group collaboration, *Review of Particle Physics*, *PTEP* **2020** (2020) 083C01.

[103] C.J. Moore, R.H. Cole and C.P.L. Berry, *Gravitational-wave sensitivity curves*, *Class. Quant. Grav.* **32** (2015) 015014 [1408.0740].

[104] E.D. Hall and M. Evans, *Metrics for next-generation gravitational-wave detectors*, *Class. Quant. Grav.* **36** (2019) 225002 [1902.09485].

[105] F. Matichard et al., *Seismic isolation of Advanced LIGO: Review of strategy, instrumentation and performance*, *Class. Quant. Grav.* **32** (2015) 185003 [1502.06300].

[106] T.P. Bodiya and I. ebrary, *Optical coatings and thermal noise in precision measurement*, Cambridge University Press„ Cambridge ; (c2012.).

[107] M.G. Beker et al., *Improving the sensitivity of future GW observatories in the 1-Hz to 10-Hz band: Newtonian and seismic noise*, *Gen. Rel. Grav.* **43** (2011) 623.

[108] S.A. Hughes and K.S. Thorne, *Seismic gravity gradient noise in interferometric gravitational wave detectors*, *Phys. Rev. D* **58** (1998) 122002 [gr-qc/9806018].

[109] LIGO SCIENTIFIC collaboration, *A Gravitational wave observatory operating beyond the quantum shot-noise limit: Squeezed light in application*, *Nature Phys.* **7** (2011) 962 [1109.2295].

[110] TAMA collaboration, *Overview of the TAMA project*, in *2nd Workshop on Gravitational Wave Detection*, pp. 41–43, 10, 1999.

[111] LIGO SCIENTIFIC collaboration, *Status of GEO 600*, *J. Phys. Conf. Ser.* **610** (2015) 012015 [1411.6588].

[112] LIGO SCIENTIFIC collaboration, *Advanced LIGO*, *Class. Quant. Grav.* **32** (2015) 074001 [1411.4547].

[113] VIRGO collaboration, *Advanced Virgo: a second-generation interferometric gravitational wave detector*, *Class. Quant. Grav.* **32** (2015) 024001 [1408.3978].

[114] KAGRA collaboration, *The Current Status and Future Prospects of KAGRA, the Large-Scale Cryogenic Gravitational Wave Telescope Built in the Kamioka Underground*, *Galaxies* **10** (2022) 63.

[115] C.S. Unnikrishnan, *IndIGO and LIGO-India: Scope and plans for gravitational wave research and precision metrology in India*, *Int. J. Mod. Phys. D* **22** (2013) 1341010 [1510.06059].

[116] S. Fairhurst, *Localization of transient gravitational wave sources: beyond triangulation*, *Class. Quant. Grav.* **35** (2018) 105002 [1712.04724].

[117] LIGO SCIENTIFIC collaboration, *Gravitational wave astronomy with LIGO and similar detectors in the next decade*, 1904.03187.

[118] B. Sathyaprakash et al., *Scientific Objectives of Einstein Telescope*, *Class. Quant. Grav.* **29** (2012) 124013 [1206.0331].

[119] D. Reitze et al., *Cosmic Explorer: The U.S. Contribution to Gravitational-Wave Astronomy beyond LIGO*, *Bull. Am. Astron. Soc.* **51** (2019) 035 [1907.04833].

[120] T. Regimbau et al., *A Mock Data Challenge for the Einstein Gravitational-Wave Telescope*, *Phys. Rev. D* **86** (2012) 122001 [1201.3563].

[121] M. Punturo et al., *The Einstein Telescope: A third-generation gravitational wave observatory*, *Class. Quant. Grav.* **27** (2010) 194002.

[122] J.W. Armstrong, F.B. Estabrook and M. Tinto, *Time-Delay Interferometry for Space-based Gravitational Wave Searches*, **527** (1999) 814.

[123] D.A. Shaddock, B. Ware, R.E. Spero and M. Vallisneri, *Post-processed time-delay interferometry for LISA*, *Phys. Rev. D* **70** (2004) 081101 [gr-qc/0406106].

[124] LIGO SCIENTIFIC collaboration, *Exploring the Sensitivity of Next Generation Gravitational Wave Detectors*, *Class. Quant. Grav.* **34** (2017) 044001 [1607.08697].

[125] K. Ackley et al., *Neutron Star Extreme Matter Observatory: A kilohertz-band gravitational-wave detector in the global network*, *Publ. Astron. Soc. Austral.* **37** (2020) e047 [2007.03128].

[126] *A satellite freed of all but gravitational forces: "triad i"*, *Journal of Spacecraft and Rockets* **11** (1974) 637 [https://doi.org/10.2514/3.62146].

[127] M. Armano et al., *Sub-Femto- g Free Fall for Space-Based Gravitational Wave Observatories: LISA Pathfinder Results*, *Phys. Rev. Lett.* **116** (2016) 231101.

[128] M. Armano, H. Audley, J. Baird, P. Binetruy, M. Born, D. Bortoluzzi et al., *Beyond the required lisa free-fall performance: New lisa pathfinder results down to* 20 μHz, *Phys. Rev. Lett.* **120** (2018) 061101.

[129] LISA collaboration, *Laser Interferometer Space Antenna*, 1702.00786.

[130] N. Seto, S. Kawamura and T. Nakamura, *Possibility of direct measurement of the acceleration of the universe using 0.1-Hz band laser interferometer gravitational wave antenna in space*, *Phys. Rev. Lett.* **87** (2001) 221103 [astro-ph/0108011].

[131] S. Kawamura et al., *The Japanese space gravitational wave antenna DECIGO*, *Class. Quant. Grav.* **23** (2006) S125.

[132] J. Crowder and N.J. Cornish, *Beyond LISA: Exploring future gravitational wave missions*, *Phys. Rev. D* **72** (2005) 083005 [gr-qc/0506015].

[133] G.M. Harry, P. Fritschel, D.A. Shaddock, W. Folkner and E.S. Phinney, *Laser interferometry for the big bang observer*, *Class. Quant. Grav.* **23** (2006) 4887.

[134] D.R. Lorimer, *Binary and Millisecond Pulsars*, *Living Rev. Rel.* **11** (2008) 8 [0811.0762].

[135] S.L. Detweiler, *Pulsar timing measurements and the search for gravitational waves*, *Astrophys. J.* **234** (1979) 1100.

[136] R.w. Hellings and G.s. Downs, *UPPER LIMITS ON THE ISOTROPIC GRAVITATIONAL RADIATION BACKGROUND FROM PULSAR TIMING ANALYSIS*, *Astrophys. J. Lett.* **265** (1983) L39.

[137] A. Sesana, A. Vecchio and M. Volonteri, *Gravitational waves from resolvable massive black hole binary systems and observations with Pulsar Timing Arrays*, *Mon. Not. Roy. Astron. Soc.* **394** (2009) 2255 [0809.3412].

[138] C.M.F. Mingarelli, T.J.W. Lazio, A. Sesana, J.E. Greene, J.A. Ellis, C.-P. Ma et al., *The Local Nanohertz Gravitational-Wave Landscape From Supermassive Black Hole Binaries*, *Nature Astron.* **1** (2017) 886 [1708.03491].

[139] P.A. Rosado, A. Sesana and J. Gair, *Expected properties of the first gravitational wave signal detected with pulsar timing arrays*, *Mon. Not. Roy. Astron. Soc.* **451** (2015) 2417 [1503.04803].

[140] A. Sesana, A. Vecchio and C.N. Colacino, *The stochastic gravitational-wave background from massive black hole binary systems: implications for observations with Pulsar Timing Arrays*, *Mon. Not. Roy. Astron. Soc.* **390** (2008) 192 [0804.4476].

[141] G. Hobbs, *The Parkes Pulsar Timing Array*, *Class. Quant. Grav.* **30** (2013) 224007 [1307.2629].

[142] R.D. Ferdman et al., *The European Pulsar Timing Array: current efforts and a LEAP toward the future*, *Class. Quant. Grav.* **27** (2010) 084014 [1003.3405].

[143] EPTA collaboration, *The European Pulsar Timing Array and the Large European Array for Pulsars*, *Class. Quant. Grav.* **30** (2013) 224009.

[144] A. Brazier et al., *The NANOGrav Program for Gravitational Waves and Fundamental Physics*, 1908.05356.

[145] P. Tarafdar et al., *The Indian Pulsar Timing Array: First data release*, *Publ. Astron. Soc. Austral.* **39** (2022) e053 [2206.09289].

[146] G. Hobbs et al., *The international pulsar timing array project: using pulsars as a gravitational wave detector*, *Class. Quant. Grav.* **27** (2010) 084013 [0911.5206].

[147] R.N. Manchester, *The International Pulsar Timing Array*, *Class. Quant. Grav.* **30** (2013) 224010 [1309.7392].

[148] NANOGrav collaboration, *The NANOGrav 15 yr Data Set: Observations and Timing of 68 Millisecond Pulsars*, *Astrophys. J. Lett.* **951** (2023) L9 [2306.16217].

[149] NANOGrav collaboration, *The NANOGrav 15 yr Data Set: Evidence for a Gravitational-wave Background*, *Astrophys. J. Lett.* **951** (2023) L8 [2306.16213].

[150] EPTA collaboration, *The second data release from the European Pulsar Timing Array - I. The dataset and timing analysis*, *Astron. Astrophys.* **678** (2023) A48 [2306.16224].

[151] EPTA, InPTA: collaboration, *The second data release from the European Pulsar Timing Array - III. Search for gravitational wave signals*, *Astron. Astrophys.* **678** (2023) A50 [2306.16214].

[152] A. Zic et al., *The Parkes Pulsar Timing Array third data release*, *Publ. Astron. Soc. Austral.* **40** (2023) e049 [2306.16230].

[153] D.J. Reardon et al., *Search for an Isotropic Gravitational-wave Background with the Parkes Pulsar Timing Array*, *Astrophys. J. Lett.* **951** (2023) L6 [2306.16215].

[154] G. Hobbs, R.N. Manchester, A. Dunning, A. Jameson, P. Roberts, D. George et al., *An ultra-wide bandwidth (704 to 4 032 mhz) receiver for the parkes radio telescope*, *Publications of the Astronomical Society of Australia* **37** (2020) .

[155] G. Janssen et al., *Gravitational wave astronomy with the SKA*, *PoS* **AASKA14** (2015) 037 [1501.00127].

[156] J. Di Francesco, D. Chalmers, N. Denman, L. Fissel, R. Friesen, B. Gaensler et al., *The next generation very large array*, .

[157] L.Z. Kelley, L. Blecha, L. Hernquist, A. Sesana and S.R. Taylor, *Single Sources in the Low-Frequency Gravitational Wave Sky: properties and time to detection by pulsar timing arrays*, *Mon. Not. Roy. Astron. Soc.* **477** (2018) 964 [1711.00075].

[158] E. Witten, *Cosmic Separation of Phases*, *Phys. Rev. D* **30** (1984) 272.

[159] D.J. Griffiths, *Introduction to elementary particles; 2nd rev. version*, Physics textbook, Wiley, New York, NY (2008).

[160] D.J. Gross and F. Wilczek, *Ultraviolet Behavior of Nonabelian Gauge Theories*, *Phys. Rev. Lett.* **30** (1973) 1343.

[161] A. Bazavov et al., *The chiral and deconfinement aspects of the QCD transition*, *Phys. Rev. D* **85** (2012) 054503 [1111.1710].

[162] M. D'Onofrio and K. Rummukainen, *Standard model cross-over on the lattice*, *Phys. Rev. D* **93** (2016) 025003 [1508.07161].

[163] Y. Aoki, G. Endrodi, Z. Fodor, S.D. Katz and K.K. Szabo, *The Order of the quantum chromodynamics transition predicted by the standard model of particle physics*, *Nature* **443** (2006) 675 [hep-lat/0611014].

[164] K. Kajantie, M. Laine, K. Rummukainen and M.E. Shaposhnikov, *Is there a hot electroweak phase transition at $m_H \gtrsim m_W$?*, *Phys. Rev. Lett.* **77** (1996) 2887 [hep-ph/9605288].

[165] S. Weinberg, *The Cosmological Constant Problem*, *Rev. Mod. Phys.* **61** (1989) 1.

[166] T. Kajita, *Nobel Lecture: Discovery of atmospheric neutrino oscillations*, *Rev. Mod. Phys.* **88** (2016) 030501.

[167] M.E. Peskin and D.V. Schroeder, *An Introduction to quantum field theory*, Addison-Wesley, Reading, USA (1995), 10.1201/9780429503559.

[168] A. Hook, *TASI Lectures on the Strong CP Problem and Axions*, *PoS* **TASI2018** (2019) 004 [1812.02669].

[169] C. Caprini et al., *Science with the space-based interferometer eLISA. II: Gravitational waves from cosmological phase transitions*, *JCAP* **04** (2016) 001 [1512.06239].

[170] W. Huang, Z. Kang, J. Shu, P. Wu and J.M. Yang, *New insights in the electroweak phase transition in the NMSSM*, *Phys. Rev. D* **91** (2015) 025006 [1405.1152].

[171] J. Kozaczuk, S. Profumo, L.S. Haskins and C.L. Wainwright, *Cosmological Phase Transitions and their Properties in the NMSSM*, *JHEP* **01** (2015) 144 [1407.4134].

[172] S.J. Huber, T. Konstandin, G. Nardini and I. Rues, *Detectable Gravitational Waves from Very Strong Phase Transitions in the General NMSSM*, *JCAP* **03** (2016) 036 [1512.06357].

[173] V. Barger, P. Langacker, M. McCaskey, M.J. Ramsey-Musolf and G. Shaughnessy, *LHC Phenomenology of an Extended Standard Model with a Real Scalar Singlet*, *Phys. Rev. D* **77** (2008) 035005 [0706.4311].

[174] J.R. Espinosa, T. Konstandin and F. Riva, *Strong Electroweak Phase Transitions in the Standard Model with a Singlet*, *Nucl. Phys. B* **854** (2012) 592 [1107.5441].

[175] C.-Y. Chen, J. Kozaczuk and I.M. Lewis, *Non-resonant Collider Signatures of a Singlet-Driven Electroweak Phase Transition*, *JHEP* **08** (2017) 096 [1704.05844].

[176] L. Fromme, S.J. Huber and M. Seniuch, *Baryogenesis in the two-Higgs doublet model*, *JHEP* **11** (2006) 038 [hep-ph/0605242].

[177] J.M. Cline and P.-A. Lemieux, *Electroweak phase transition in two Higgs doublet models*, *Phys. Rev. D* **55** (1997) 3873 [hep-ph/9609240].

[178] C. Grojean, G. Servant and J.D. Wells, *First-order electroweak phase transition in the standard model with a low cutoff*, *Phys. Rev. D* **71** (2005) 036001 [hep-ph/0407019].

[179] C. Delaunay, C. Grojean and J.D. Wells, *Dynamics of Non-renormalizable Electroweak Symmetry Breaking*, *JHEP* **04** (2008) 029 [0711.2511].

[180] L.A. Popa and A. Vasile, *WMAP 5-year constraints on lepton asymmetry and radiation energy density: Implications for Planck*, *JCAP* **06** (2008) 028 [0804.2971].

[181] D.J. Schwarz and M. Stuke, *Lepton asymmetry and the cosmic QCD transition*, *JCAP* **11** (2009) 025 [0906.3434].

[182] L. Randall and G. Servant, *Gravitational waves from warped spacetime*, *JHEP* **05** (2007) 054 [hep-ph/0607158].

[183] G. Nardini, M. Quiros and A. Wulzer, *A Confining Strong First-Order Electroweak Phase Transition*, *JHEP* **09** (2007) 077 [0706.3388].

[184] A.G. Cohen, D.B. Kaplan and A.E. Nelson, *Progress in electroweak baryogenesis*, *Ann. Rev. Nucl. Part. Sci.* **43** (1993) 27 [hep-ph/9302210].

[185] A.D. Sakharov, *Violation of CP Invariance, C asymmetry, and baryon asymmetry of the universe*, *Pisma Zh. Eksp. Teor. Fiz.* **5** (1967) 32.

[186] M. Quiros, *Finite temperature field theory and phase transitions*, in *ICTP Summer School in High-Energy Physics and Cosmology*, pp. 187–259, 1, 1999 [hep-ph/9901312].

[187] V.A. Kuzmin, V.A. Rubakov and M.E. Shaposhnikov, *On the Anomalous Electroweak Baryon Number Nonconservation in the Early Universe*, *Phys. Lett. B* **155** (1985) 36.

[188] M. Joyce, T. Prokopec and N. Turok, *Electroweak baryogenesis from a classical force*, *Phys. Rev. Lett.* **75** (1995) 1695 [hep-ph/9408339].

[189] A.J. Beekman, L. Rademaker and J. van Wezel, *An Introduction to Spontaneous Symmetry Breaking*, *SciPost Phys. Lect. Notes* **11** (2019) 1 [1909.01820].

[190] N. Goldenfeld, *Lectures On Phase Transitions And The Renormalization Group*, Frontiers in physics, Westview Press (1992), 10.1201/9780429493492.

[191] A. Linde, *Particle physics and inflationary cosmology*, Harwood Academic Pub. (1990).

[192] G.W. Anderson and L.J. Hall, *The Electroweak phase transition and baryogenesis*, *Phys. Rev. D* **45** (1992) 2685.

[193] M. Dine, R.G. Leigh, P. Huet, A.D. Linde and D.A. Linde, *Comments on the electroweak phase transition*, *Phys. Lett. B* **283** (1992) 319 [hep-ph/9203201].

[194] S.R. Coleman, *The Fate of the False Vacuum. 1. Semiclassical Theory*, *Phys. Rev. D* **15** (1977) 2929.

[195] C.G. Callan, Jr. and S.R. Coleman, *The Fate of the False Vacuum. 2. First Quantum Corrections*, *Phys. Rev. D* **16** (1977) 1762.

[196] C.L. Hammer, J.E. Shrauner and B. DeFacio, *Alternate Derivation of Vacuum Tunneling*, *Phys. Rev. D* **19** (1979) 667.

[197] M. Laine and A. Vuorinen, *Basics of Thermal Field Theory*, vol. 925, Springer (2016), 10.1007/978-3-319-31933-9, [1701.01554].

[198] A.D. Linde, *Fate of the False Vacuum at Finite Temperature: Theory and Applications*, *Phys. Lett. B* **100** (1981) 37.

[199] K. Enqvist, J. Ignatius, K. Kajantie and K. Rummukainen, *Nucleation and bubble growth in a first order cosmological electroweak phase transition*, *Phys. Rev. D* **45** (1992) 3415.

[200] M.A. Ajmi and M. Hindmarsh, *Thermal suppression of bubble nucleation at first-order phase transitions in the early Universe*, *Phys. Rev. D* **106** (2022) 023505 [2205.04097].

[201] A. Megevand and S. Ramirez, *Bubble nucleation and growth in very strong cosmological phase transitions*, *Nucl. Phys. B* **919** (2017) 74 [1611.05853].

[202] J.R. Espinosa, T. Konstandin, J.M. No and G. Servant, *Energy Budget of Cosmological First-order Phase Transitions*, *JCAP* **06** (2010) 028 [1004.4187].

[203] D. Bodeker and G.D. Moore, *Can electroweak bubble walls run away?*, *JCAP* **05** (2009) 009 [0903.4099].

[204] D. Bodeker and G.D. Moore, *Electroweak Bubble Wall Speed Limit*, *JCAP* **05** (2017) 025 [1703.08215].

[205] L.D. Landau and E.M. Lifshitz, *Fluid Mechanics, Second Edition: Volume 6 (Course of Theoretical Physics)*, Course of theoretical physics / by L. D. Landau and E. M. Lifshitz, Vol. 6, Butterworth-Heinemann, 2 ed. (Jan., 1987).

[206] G.D. Moore and T. Prokopec, *How fast can the wall move? A Study of the electroweak phase transition dynamics*, *Phys. Rev. D* **52** (1995) 7182 [hep-ph/9506475].

[207] J. Ignatius, K. Kajantie, H. Kurki-Suonio and M. Laine, *The growth of bubbles in cosmological phase transitions*, *Phys. Rev. D* **49** (1994) 3854 [astro-ph/9309059].

[208] C. Caprini, R. Durrer and G. Servant, *Gravitational wave generation from bubble collisions in first-order phase transitions: An analytic approach*, *Phys. Rev. D* **77** (2008) 124015 [0711.2593].

[209] C. Caprini et al., *Detecting gravitational waves from cosmological phase transitions with LISA: an update*, *JCAP* **03** (2020) 024 [1910.13125].

[210] F. Giese, T. Konstandin, K. Schmitz and J. van de Vis, *Model-independent energy budget for LISA*, *JCAP* **01** (2021) 072 [2010.09744].

[211] F.R. Ares, M. Hindmarsh, C. Hoyos and N. Jokela, *Gravitational waves from a holographic phase transition*, *JHEP* **21** (2020) 100 [2011.12878].

[212] F. Giese, T. Konstandin and J. van de Vis, *Model-independent energy budget of cosmological first-order phase transitions—A sound argument to go beyond the bag model*, *JCAP* **07** (2020) 057 [2004.06995].

[213] M. Kamionkowski, A. Kosowsky and M.S. Turner, *Gravitational radiation from first order phase transitions*, *Phys. Rev. D* **49** (1994) 2837 [astro-ph/9310044].

[214] D. Croon, O. Gould, P. Schicho, T.V.I. Tenkanen and G. White, *Theoretical uncertainties for cosmological first-order phase transitions*, *JHEP* **04** (2021) 055 [2009.10080].

[215] C. Gowling and M. Hindmarsh, *Observational prospects for phase transitions at LISA: Fisher matrix analysis*, *JCAP* **10** (2021) 039 [2106.05984].

[216] A. Kosowsky and M.S. Turner, *Gravitational radiation from colliding vacuum bubbles: envelope approximation to many bubble collisions*, *Phys. Rev. D* **47** (1993) 4372 [astro-ph/9211004].

[217] S.J. Huber and T. Konstandin, *Gravitational Wave Production by Collisions: More Bubbles*, *JCAP* **09** (2008) 022 [0806.1828].

[218] D. Cutting, M. Hindmarsh and D.J. Weir, *Gravitational waves from vacuum first-order phase transitions: from the envelope to the lattice*, *Phys. Rev. D* **97** (2018) 123513 [1802.05712].

[219] D. Cutting, E.G. Escartin, M. Hindmarsh and D.J. Weir, *Gravitational waves from vacuum first order phase transitions II: from thin to thick walls*, *Phys. Rev. D* **103** (2021) 023531 [2005.13537].

[220] M. Lewicki and V. Vaskonen, *On bubble collisions in strongly supercooled phase transitions*, *Phys. Dark Univ.* **30** (2020) 100672 [1912.00997].

[221] C.J. Hogan, *Gravitational radiation from cosmological phase transitions*, *Mon. Not. Roy. Astron. Soc.* **218** (1986) 629.

[222] M. Hindmarsh, S.J. Huber, K. Rummukainen and D.J. Weir, *Gravitational waves from the sound of a first order phase transition*, *Phys. Rev. Lett.* **112** (2014) 041301 [1304.2433].

[223] M. Hindmarsh, S.J. Huber, K. Rummukainen and D.J. Weir, *Numerical simulations of acoustically generated gravitational waves at a first order phase transition*, *Phys. Rev. D* **92** (2015) 123009 [1504.03291].

[224] M. Hindmarsh, S.J. Huber, K. Rummukainen and D.J. Weir, *Shape of the acoustic gravitational wave power spectrum from a first order phase transition*, *Phys. Rev. D* **96** (2017) 103520 [1704.05871].

[225] D. Cutting, M. Hindmarsh and D.J. Weir, *Vorticity, kinetic energy, and suppressed gravitational wave production in strong first order phase transitions*, *Phys. Rev. Lett.* **125** (2020) 021302 [1906.00480].

[226] A. Roper Pol, S. Mandal, A. Brandenburg, T. Kahniashvili and A. Kosowsky, *Numerical simulations of gravitational waves from early-universe turbulence*, *Phys. Rev. D* **102** (2020) 083512 [1903.08585].

[227] R. Jinno, T. Konstandin and H. Rubira, *A hybrid simulation of gravitational wave production in first-order phase transitions*, *JCAP* **04** (2021) 014 [2010.00971].

[228] R. Jinno, T. Konstandin, H. Rubira and I. Stomberg, *Higgsless simulations of cosmological phase transitions and gravitational waves*, *JCAP* **02** (2023) 011 [2209.04369].

[229] C. Caprini, R. Jinno, T. Konstandin, A. Roper Pol, H. Rubira and I. Stomberg, *Gravitational waves from decaying sources in strong phase transitions*, 2409.03651.

[230] M. Hindmarsh, *Sound shell model for acoustic gravitational wave production at a first-order phase transition in the early Universe*, *Phys. Rev. Lett.* **120** (2018) 071301 [1608.04735].

[231] M. Hindmarsh and M. Hijazi, *Gravitational waves from first order cosmological phase transitions in the Sound Shell Model*, *JCAP* **12** (2019) 062 [1909.10040].

[232] J. Ahonen and K. Enqvist, *Electrical conductivity in the early universe*, *Phys. Lett. B* **382** (1996) 40 [hep-ph/9602357].

[233] R. Durrer and A. Neronov, *Cosmological Magnetic Fields: Their Generation, Evolution and Observation*, *Astron. Astrophys. Rev.* **21** (2013) 62 [1303.7121].

[234] A. Brandenburg, K. Enqvist and P. Olesen, *Large scale magnetic fields from hydromagnetic turbulence in the very early universe*, *Phys. Rev. D* **54** (1996) 1291 [astro-ph/9602031].

[235] U.-L. Pen and N. Turok, *Shocks in the Early Universe*, *Phys. Rev. Lett.* **117** (2016) 131301 [1510.02985].

[236] P.B. Arnold, G.D. Moore and L.G. Yaffe, *Transport coefficients in high temperature gauge theories. 1. Leading log results*, *JHEP* **11** (2000) 001 [hep-ph/0010177].

[237] A. Kosowsky, A. Mack and T. Kahniashvili, *Gravitational radiation from cosmological turbulence*, *Phys. Rev. D* **66** (2002) 024030 [astro-ph/0111483].

[238] A.D. Dolgov, D. Grasso and A. Nicolis, *Relic backgrounds of gravitational waves from cosmic turbulence*, *Phys. Rev. D* **66** (2002) 103505 [astro-ph/0206461].

[239] C. Caprini and R. Durrer, *Gravitational waves from stochastic relativistic sources: Primordial turbulence and magnetic fields*, *Phys. Rev. D* **74** (2006) 063521 [astro-ph/0603476].

[240] G. Gogoberidze, T. Kahniashvili and A. Kosowsky, *The Spectrum of Gravitational Radiation from Primordial Turbulence*, *Phys. Rev. D* **76** (2007) 083002 [0705.1733].

[241] C. Caprini, R. Durrer and G. Servant, *The stochastic gravitational wave background from turbulence and magnetic fields generated by a first-order phase transition*, *JCAP* **12** (2009) 024 [0909.0622].

[242] P. Auclair, C. Caprini, D. Cutting, M. Hindmarsh, K. Rummukainen, D.A. Steer et al., *Generation of gravitational waves from freely decaying turbulence*, *JCAP* **09** (2022) 029 [2205.02588].

[243] A. Kolmogorov, *The Local Structure of Turbulence in Incompressible Viscous Fluid for Very Large Reynolds' Numbers*, *Akademiia Nauk SSSR Doklady* **30** (1941) 301.

[244] L. Rezzolla and O. Zanotti, *Relativistic Hydrodynamics*, Oxford University Press (9, 2013), 10.1093/acprof:oso/9780198528906.001.0001.

[245] C. Eckart, *The Thermodynamics of irreversible processes. 3.. Relativistic theory of the simple fluid*, *Phys. Rev.* **58** (1940) 919.

[246] I. Prigogine, *Introduction to Thermodynamics of Irreversible Processes*, American lecture series, Thomas (1955).

[247] A. Brandenburg, T. Kahniashvili, S. Mandal, A. Roper Pol, A.G. Tevzadze and T. Vachaspati, *Evolution of hydromagnetic turbulence from the electroweak phase transition*, *Phys. Rev. D* **96** (2017) 123528 [1711.03804].

[248] NORDITA, *The Pencil Code: A High-Order MPI Code for MHD Turbulence. User's and Reference Manual.*, 2024.

[249] J. Carlson, A. Jaffe, A. Wiles, C.M. Institute and A.M. Society, *The Millennium Prize Problems*, American Mathematical Society (2006).

[250] J. Hinze, *Turbulence*, McGraw-Hill classic textbook reissue, McGraw-Hill (1975).

[251] M. Lesieur, *Turbulence in fluids*, vol. 40 of *Fluid Mechanics and Its Applications*, Springer, Dordrecht, third revised and enlarged edition. ed. (1997).

[252] P.A. Davidson, *Turbulence : an introduction for scientists and engineers*, Oxford University Press, Oxford (2004).

[253] S. Nazarenko, *Wave Turbulence*, Lecture Notes in Physics, Springer Berlin Heidelberg (2011).

[254] S. Galtier, *Physics of Wave Turbulence*, Cambridge University Press (2022).

[255] V.E. Zakharov and R.Z. Sagdeev, *Spectrum of Acoustic Turbulence*, *Soviet Physics Doklady* **15** (1970) 439.

[256] K. Elsasser and H. Schamel, *Acoustic turbulence*, *Physics Letters A* **47** (1974) 419.

[257] B.B. Kadomtsev and V.I. Petviashvili, *Acoustic Turbulence*, *Soviet Physics Doklady* **18** (1973) 115.

[258] J. Burgers, *A mathematical model illustrating the theory of turbulence*, *Advances in Applied Mechanics* **1** (1948) 171.

[259] J. Dahl, *Simulation code for fluids in two dimensions*, Dec., 2021. 10.5281/zenodo.5786090.

[260] J. Dahl, *Simulation code for fluids in three dimensions*, Jan., 2024. 10.5281/zenodo.10580342.

[261] C.R. Harris et al., *Array programming with NumPy*, *Nature* **585** (2020) 357.

[262] S. Behnel, R. Bradshaw, C. Citro, L. Dalcin, D.S. Seljebotn and K. Smith, *Cython: The best of both worlds*, *Computing in Science Engineering* **13** (2011) 31.

[263] D. Cooke, T. Hochberg, F. Alted, I. Vilata, M. Wiebe, G. de Menten et al., *NumExpr: Fast numerical expression evaluator for NumPy*, Nov., 2018. 10.5281/zenodo.1492916.

[264] L. Dalcín, R. Paz and M. Storti, *Mpi for python*, *Journal of Parallel and Distributed Computing* **65** (2005) 1108.

[265] Dalcin, Lisandro and Mortensen, Mikael and Keyes, David E, *Fast parallel multidimensional FFT using advanced MPI*, *Journal of Parallel and Distributed Computing* (2019) .

[266] Pencil Code collaboration, *The Pencil Code, a modular MPI code for partial differential equations and particles: multipurpose and multiuser-maintained*, *J. Open Source Softw.* **6** (2021) 2807 [2009.08231].

[267] G. Hairer, E Wanner and G. Wanner, *Solving ordinary differential equations II. Stiff differential algebraic problems*, Springer series in computational mathematics 14, Springer, Berlin (1991).

[268] F.K.C.R. Lewy, H., *Über die partiellen differenzengleichungen der mathematischen physik*, *Mathematische Annalen* **100** (1928) 32.

[269] B. Fornberg, *Generation of finite difference formulas on arbitrarily spaced grids*, *Mathematics of Computation* **51** (1988) 699.

[270] E. Hewitt and R.E. Hewitt, *The gibbs-wilbraham phenomenon: An episode in fourier analysis*, *Archive for History of Exact Sciences* **21** (1979) 129.

[271] A. Brandenburg and E. Ntormousi, *Dynamo effect in unstirred self-gravitating turbulence*, *Monthly Notices of the Royal Astronomical Society* **513** (2022) 2136–2151.

[272] G. Falkovich, *Bottleneck phenomenon in developed turbulence*, *Physics of Fluids* **6** (1994) 1411.

[273] W. Dobler, N.E.L. Haugen, T.A. Yousef and A. Brandenburg, *Bottleneck effect in three-dimensional turbulence simulations*, *Physical Review E* **68** (2003) .

[274] P.G. Saffman, *On the spectrum and decay of random two-dimensional vorticity distributions at large reynolds number*, *Studies in Applied Mathematics* **50** (1971) .

[275] M. Lesieur, *Turbulence in Fluids*, Fluid Mechanics and Its Applications, Springer Netherlands (2008).

[276] A. Brandenburg and T. Kahniashvili, *Classes of hydrodynamic and magnetohydrodynamic turbulent decay*, *Phys. Rev. Lett.* **118** (2017) 055102 [1607.01360].

[277] C. Caprini, R. Durrer, T. Konstandin and G. Servant, *General Properties of the Gravitational Wave Spectrum from Phase Transitions*, *Phys. Rev. D* **79** (2009) 083519 [0901.1661].

[278] A. Monin and A. Yaglom, *Statistical Fluid Mechanics, Volume II: Mechanics of Turbulence*, Dover Books on Physics, Dover Publications (2013).

[279] P.G. Castro, A.F. Heavens and T.D. Kitching, *Weak lensing analysis in three dimensions*, *Phys. Rev. D* **72** (2005) 023516 [astro-ph/0503479].

[280] N.E. Chisari and A. Pontzen, *Unequal time correlators and the Zel'dovich approximation*, *Phys. Rev. D* **100** (2019) 023543 [1905.02078].

[281] A. Roper Pol, S. Procacci and C. Caprini, *Characterization of the gravitational wave spectrum from sound waves within the sound shell model*, *Phys. Rev. D* **109** (2024) 063531 [2308.12943].

[282] L. Giombi, J. Dahl and M. Hindmarsh, *Signatures of the speed of sound on the gravitational wave power spectrum from sound waves*, *JCAP* **01** (2025) 100 [2409.01426].

[283] P. Virtanen et al., *SciPy 1.0: Fundamental Algorithms for Scientific Computing in Python*, *Nature Methods* **17** (2020) 261.